University of Massachusetts Amherst
ScholarWorks@UMass Amherst

Doctoral Dissertations | Dissertations and Theses

Spring August 2014

SIMULATION AND MODELING OF THE DECAY OF ANISOTROPIC TURBULENCE

Christopher J. Zusi

Follow this and additional works at: https://scholarworks.umass.edu/dissertations_2

 Part of the Mechanical Engineering Commons

Recommended Citation

Zusi, Christopher J., "SIMULATION AND MODELING OF THE DECAY OF ANISOTROPIC TURBULENCE" (2014). *Doctoral Dissertations*. 129.
https://doi.org/10.7275/6jst-4h05 https://scholarworks.umass.edu/dissertations_2/129

This Open Access Dissertation is brought to you for free and open access by the Dissertations and Theses at ScholarWorks@UMass Amherst. It has been accepted for inclusion in Doctoral Dissertations by an authorized administrator of ScholarWorks@UMass Amherst. For more information, please contact scholarworks@library.umass.edu.

SIMULATION AND MODELING
OF THE
DECAY OF ANISOTROPIC TURBULENCE

A Dissertation Presented

by

CHRISTOPHER J. ZUSI

Submitted to the Graduate School of the
University of Massachusetts Amherst in partial fulfillment
of the requirements for the degree of

DOCTOR OF PHILOSOPHY

May 2014

Mechanical and Industrial Engineering

© Copyright by Christopher J. Zusi 2014

All Rights Reserved

SIMULATION AND MODELING
OF THE
DECAY OF ANISOTROPIC TURBULENCE

A Dissertation Presented

by

CHRISTOPHER J. ZUSI

Approved as to style and content by:

_____

J. Blair Perot, Chair

_____

Stephen M. de Bruyn Kops, Member

_____

Marinos N. Vouvakis, Member

_____

Donald L. Fisher, Department Head
Mechanical and Industrial Engineering

ACKNOWLEDGMENTS

Thank you to Blair Perot for his guidance, support and our many interesting and in depth conversations on many subjects, including turbulence. Thank you to Prof. de Bruyn Kops and Prof. Vouvakis for their time and helpful insight. Thank you to my wife Lynne and my children Nolan and Anna for their endless patience and understanding and to the rest of my family for their kind words, friendship and support. Thank you to my co-workers in the CFD lab for their help and friendship. Finally the author would like to acknowledge the National Science Foundation for their support (CBET grant 1032364).

ABSTRACT

SIMULATION AND MODELING OF THE DECAY OF ANISOTROPIC TURBULENCE

April 2014

CHRISTOPHER J. ZUSI

B.S., UNIVERSITY OF MASSACHUSETTS AMHERST

M.S., UNIVERSITY OF NEVADA RENO

Ph.D., UNIVERSITY OF MASSACHUSETTS AMHERST

Directed by: Professor J. Blair Perot

The influence of turbulence structure, parameterized by two point correlations, on the return-to-isotropy process is examined under controlled conditions. In order to determine the influence of structure, direct numerical simulations (DNS) of return-to-isotropy in homogeneous, anisotropic turbulence is performed on meshes of 512^3 and 512x512x1024. Isotropic turbulence is generated by mechanical stirring (as in a wind tunnel). Anisotropy is then generated by one of four fundamentally different mean strains, axisymmetric expansion and contraction, plane strain, and pure rotation. Each strain produces very different structure within the turbulence. The influence on the return-to-isotropy process of the initial structure (parameterized by the two-point

correlations) as well as Reynolds number and initial length scale, is characterized and used to calibrate the Oriented-Eddy Collision (OEC) turbulence model developed by Martell and Perot [1]. In addition, this data provides critical information for other turbulence models which incorporate turbulence structure.

TABLE OF CONTENTS

LIST OF TABLES

Table Page

LIST OF FIGURES

Figure Page

CHAPTER 1

INTRODUCTION

Turbulence is not easily described but it is easy to give examples. Atmospheric turbulence such as weather modeling, pollution transport, combustion processes, chemical engineering problems including mixing and entrainment, air over wind turbine blades, water over a ship's hull, within pipes and heat exchangers, etc. are all subjected to the consequences of turbulence. Understanding the behavior of such turbulent flows and more importantly the ability to accurately computationally model these flows has broad engineering and economic consequences. For many years there have existed a number of models that aim to capture the physics of turbulence and these models have been employed by the scientific and engineering community the world around. Because of our collective lack of understanding of the turbulence process, our engineering and scientific communities are forced to deal with the shortcomings of existing models by building in tolerances in designs to accommodate modeling inaccuracies. More accurate and cost effective modeling tools would also allow engineers to explore designs that might otherwise go untested.

1.1 Anisotropy

Anisotropy in the context of turbulence research typically refers to flow configurations in which the turbulent velocity fluctuations are not equal when measured along the different coordinate directions. Anisotropy is caused primarily by the fact that

energy injected into the turbulence from the mean flow is not isotropic. In a boundary or shear layer, for example, only the streamwise velocity fluctuations directly receive energy from the mean flow. This leads to velocity fluctuations in the streamwise direction that are roughly twice the level of the fluctuations in the spanwise direction and depending on the location, the spanwise fluctuations can be orders of magnitude larger than the wall-normal velocity fluctuations. These secondary turbulence components receive energy via a process known as return-to-isotropy which continually redistributes the fluctuating energy among the different component directions. The smallest fluctuation levels are the physically important ones, which will be discussed further on in this section, and they are determined by the rate of redistribution, the rate at which this energy redistribution occurs is a very important part of a turbulence mode. The other source of strong anisotropy is walls. Even slip walls cause the velocity fluctuations normal to the wall to be severely damped. This is because fluctuations normal to the wall or free-surface will eventually want to travel through the wall or surface and this is prohibited. Pressure fluctuations arise that specifically damp these normal fluctuations. Return-to-isotropy, and the energy redistribution associated with that process, tends to increase the important normal fluctuation levels above the value that simple wall reflection theory predicts.

Absent any forces to increase or maintain the anisotropy, the velocity fluctuations are expected to become evenly distributed among the individual coordinate components over time. (return-to-isotropy). The return-to-isotropy process is not well understood. Even the overall decay rate of turbulent kinetic energy (TKE) is still a topic of debate, Davidson [2].

1.1.1 Applied Anisotropy

The level of anisotropy in turbulence is important because it can have a direct influence on how the turbulence affects the mean flow. As mentioned earlier it is frequently the minimum turbulence level, not the average turbulence level which dictates the mean flow evolution. The turbulent kinetic energy measures the average velocity fluctuation level and it is frequently a component of turbulence models. However, near walls the normal (minimal) velocity component (not the kinetic energy) actually dictates turbulent mixing and eddy viscosity levels, Durbin [3]. This is can be seen clearly in figure 1.1 (data from Kim [4]) where it is shown that the exact eddy viscosity is far better represented using a model based on the minimum turbulence level than it is on a model using the kinetic energy.

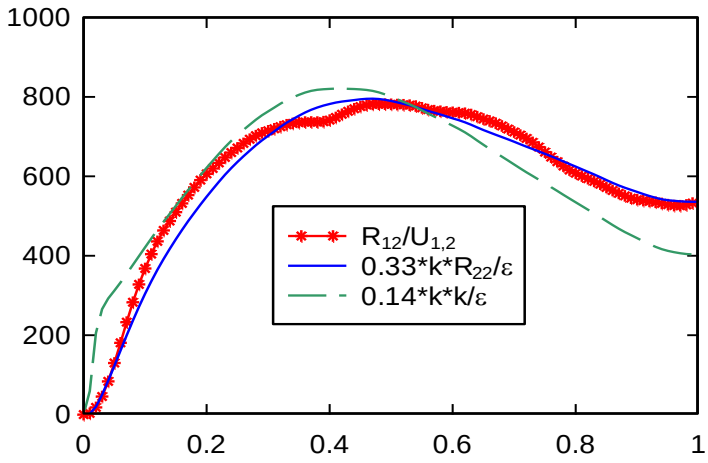

Figure 1.1 Eddy viscosity in channel flow at Re=590. Red symbols are the exact eddy viscosity. Blue line is eddy viscosity based on the minimum turbulence level and green line is the modeled eddy viscosity based on the kinetic energy.

Like the turbulent energy cascade, return-to-isotropy is an inherently non-linear process which involves turbulence-turbulence interactions. The return process significantly influences near wall turbulence. In the corner of a duct the anisotropy is the

driving mechanism behind large secondary mean recirculation flows, Speziale [5], in atmospheric and oceanic heat and mass transfer processes like CO_2 absorption, in heat exchanger performance, in wing tip vortices, and a host of important and currently poorly modeled turbulent flow situations. In order to improve our understanding and impart this understanding on future engineering projects, better information about the return-to-isotropy process is needed. In particular, information about the turbulent structures (i.e. the shape of the underlying eddies) and their impact on the return-to-isotropy process. The idea of understanding the return-to-isotropy process by way of structure is the main premise of the current body of work. Before this idea is discussed at length it is important to put these ideas into historical context.

1.1.2 Modeling Anisotropy

At the very lowest level of approximation, anisotropy is neglected in turbulence models. One-equation models (such as the Spalart-Allmaras model [6], [7]) and the widely used two-equation models, such as k/ε and k/ω, treat the turbulence as isotropic. These types of turbulence models are the workhorse of industry and are amazingly useful given the crudeness of this and some of their other underlying approximations.

Return-to-isotropy is a critical component of more advanced turbulence models. Figure 1.2 shows the results from two classic experiments of Le Penven [8]. This figure shows the different turbulence levels for two different anisotropic turbulent flows. Both figures show the tendency of the turbulence levels to converge to a common value (isotropic turbulence). Case B even shows the smallest turbulence level increasing in time due to the return-to-isotropy process. Like the experiments of Le Penven, which

were performed in 1985, many of the key experiments Le Penven [8], Lumley [9], Choi [10] [11], Gence [12], Harris [13] and simulations Rogallo [14], Yamamoto [15] [16] concerning this phenomena are now quite old. While these were landmark studies in their time, they focused almost entirely (as did all studies at that time) on the velocity fluctuations. This was reasonable as it is the velocity fluctuations which ultimately influence the mean flow and its evolution.

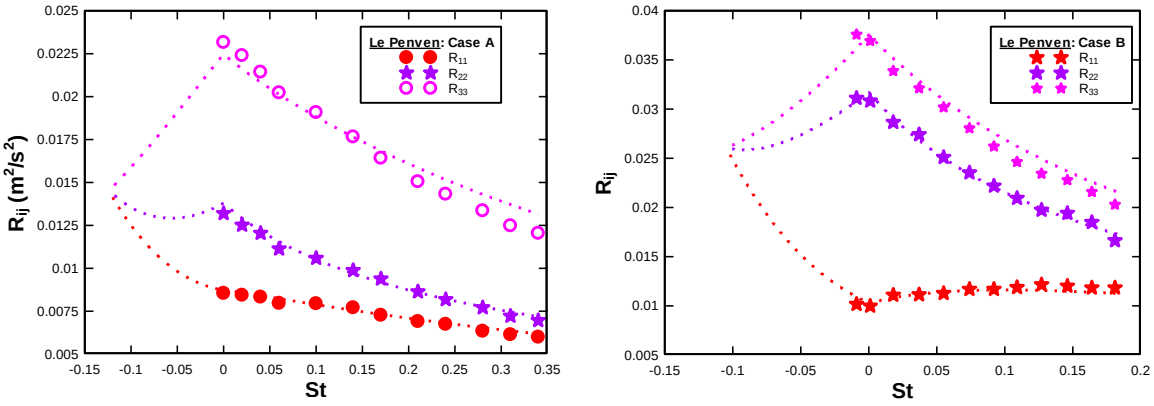

(a) (b)

Figure 1.2 Reynolds stresses for Le Penven case A and case B experiments. Symbols: experimental data. Dotted lines: Rotta return-to-isotropy model. Case A: Rotta constant = 1.7. Case B: Rotta constant = 2.9.

However, over the years it has proven very difficult to develop return-to-isotropy models based only on knowledge of the velocity fluctuations alone. The return constants , such as those of Rotta, used by Le Penven in figure 1.2, invariably differ significantly for different flows. Reynolds stress transport (RST) models can represent anisotropy and number of complex return models (Sjögren and Johansson [17], Sarkar and Speziale [18], Haworth and Pope [19]) have been proposed which attempt to parameterize the decay rates purely in terms of the anisotropy, but none have been widely adopted. Improving significantly on predictive accuracy of these types of models requires fundamental changes in how the turbulence is modeled.

Recent evidence suggests that it may be the structure of the turbulence not the anisotropy levels themselves which govern the decay rates. The simulations shown in figure 1.3 may show little return-to-isotropy because this simulation has very isotropic structures and slightly anisotropic fluctuations (due to statistical variation). It is hypothesize in this work, that a very simple return-to-isotropy model is possible if the return process is modeled using turbulent structural information.

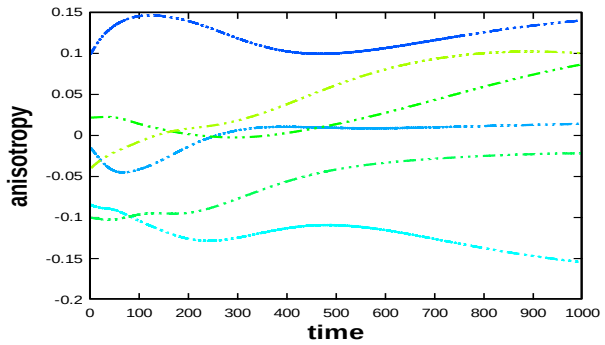

Figure 1.3 The six components of the anisotropy tensor calculated from 512^3 DNS simulations over a very long time period. In a return-to-isotropy situation these curves would be trending towards zero.

The argument that Reynolds stress anisotropy is not sufficient to predict anisotropic turbulence decay (developed by these prior groups) is as follows. Two turbulent flows can have identical Reynolds stress tensors, and therefore identical anisotropy tensors, and yet be structurally very different. For example, turbulence stratified by density or rotation (as in the atmosphere or ocean) has pancake shaped eddies that are 'flat' in one direction (normal to gravity in the density stratified case). In contrast, the turbulence generated by a shear flow tends to be elongated in one direction ("cigar" or "hot dog" shaped), see figure 1.4.

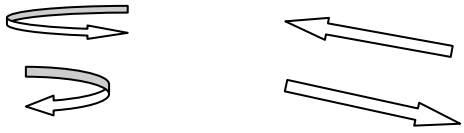

(a) (b)

Figure 1.4 (a) pancake shaped eddies typical of many stratified turbulent flows (b) long jet like eddies common in shear flow.

Despite clear differences in their structure, both flows can have identical Reynolds stress tensors and anisotropy tensors. This suggests that the fluctuations alone (the anisotropy tensor) does not provide enough information about the turbulence to accurately predict the tensor's evolution.

A few advanced modeling approaches (Besnard [20] [21], Kassinos & Reynolds [22], Van Slooten and Pope [23], Perot & Chartrand [24]) now include turbulent structural information. Kassinos & Reynolds define additional single-point tensor quantities based on the streamfunction derivatives that contain additional information about the dimension, 'circulicity', and 'stropholysis' of the turbulence. In contrast, Besnard and coworkers [20] use information from the two-point correlations to provide the additional information required to predict anisotropic decay and return-to-isotropy. By including structural information (based on two-point correlations), modelers have the opportunity to radically change the predictive capacity of turbulence models by increasing the included physics and reducing the number of adjustable constants. Unfortunately, prior experiments and simulations on return-to-isotropy do not contain sufficient information to calibrate and develop advanced turbulence models containing structural information.

1.1.3 Studying Anisotropy

The study of return-to-isotropy must, by definition, start with the generation of anisotropy. The decay of turbulence that has been subjected to strain is interesting because it is a case in which the turbulence can be homogeneous but not isotropic. After straining, the fluctuations have different magnitudes in the three different principal directions. The generation of anisotropy via constant strain can be precisely defined and therefore accurately reproduced in both experiments and in other numerical simulations. Direct numerical simulation (DNS) allows precise level of control over the parameters including the strain rate, the initial Reynolds number and turbulent length scale. In addition DNS provides complete 3D data at both large and small scales for both the velocity fluctuations and the turbulence structure. Compared to experiments, DNS is better suited to cover a large range of parameter space. Kurian and Fransson [25] show that the use of a contraction to isotropize the Reynolds stresses that result from the anisotropic wind tunnel grid turbulence does not also isotropize the two-point correlations. Wind tunnels also have trouble with large axisymmetric expansion because of separation issues. Large rotation rates are difficult to achieve experimentally, as is rapidly generating and removing walls without creating mean shear.

The return-to-isotropy process is part and parcel of the energy cascade that transfers energy from large length-scale eddies to smaller length-scale eddies. Studying return-to-isotropy is therefore equivalent to studying the energy cascade for anisotropic

turbulence. Since in practice, almost all turbulence is not isotropic, this is an important endeavor.

The return-to-isotropy process is difficult to accurately model. As discussed earlier, most turbulence models assume that return-to-isotropy is solely a function of the degree of anisotropy of the velocity fluctuations. However, one primary tenet of this research is that the anisotropy velocity fluctuations themselves are not sufficient to predict the-return-to-isotropy rates. The idea that more information than Reynolds stress anisotropy is needed to predict anisotropic decay is not new. It has been present by Kassinos and Reynolds [26] [27] [28] [29] and their coworkers. In addition, perhaps, the earliest references to the basic idea can be attributed to the turbulence research group at Los Alamos [20] [21].

This work explores the use of two-point structure information similar to that of the Los Alamos group, Besnard [20], rather than one-point statistics of the streamfunction derivatives (used by Kassinos, Reynolds and coworkers) as the additional information necessary to close the system. For rapid distortion theory (RDT) these two approaches are equivalent, as they must be. But for the decay case (which is the antithesis of RDT) it is no longer clear that both approaches to understanding and modeling the anisotropic decay process are still equivalent.

Kevlahan and Hunt [30] discuss the theory for turbulence when it is being strained. Under very large strains, rapid distortion theory (RDT), Batchelor [31], applies. The turbulence evolution can be linearized and solved exactly in this limit. Hällback *et al.* [32] describe how this linear theory can even be applied to the non-linear cascade related terms like the dissipation rate tensor. RDT proves that Reynolds stresses alone

contain insufficient information to predict their own evolution when the turbulence is subjected to large strain.

There is relatively little in the way of theory that applies directly to the decay of anisotropic turbulence, but isotropic decay has been extensively studied. Perot [33] reviews much of what is available with regard to research into isotropic decay theory. One of the most critical results for isotropic decay is due to Saffman [34] and it shows that the behavior of the large scale correlations (or small wave numbers) dictates the decay rate. This means that both experiments and simulations must be careful to keep the large eddy length-scale much smaller than the tunnel size or simulation domain. Perot [33] shows that $L = k^{3/2}/\varepsilon$ should be less than ¼ of the periodic domain size or the decay of isotropic turbulence becomes length-scale constrained. In order to capture both the large and the small scales, the simulations reported in this work will be at resolutions of 512^3. The additional resolution in the simulations is not used to increase the turbulent Reynolds numbers over prior calculations. It is used to capture the influential large scales better and to produce smoother statistics. The simulations in this work are similar in Reynolds number and resolution to the well resolved simulations of de Bruyn Kops and Riley [35]. The turbulent Reynolds numbers present in these simulations should be sufficient to capture the fundamental physics. The turbulent Reynolds number in the majority of the cases simulated is nearly the same as the turbulent Reynolds numbers in the classic decay experiments of Comte-Bellot and Corrsin [36].

Another important aspect of the simulations presented in this work relates to the generation of the initial isotropic turbulence. It is well understood that the small wavenumber (or large correlation scales) are set by the initial conditions (IC) and are

invariant during the decay process. Most simulations therefore inadvertently impose the decay behavior via the choice of the initial turbulence spectrum or initial turbulence forcing. It is desired for these studies that the large scale correlations be formed physically, and not via the specification of initial conditions. The initial flow for these simulations is therefore a velocity and pressure of zero. The turbulence is then generated physically by having small solid and stationary 'mixing boxes' in the domain (768 of them for the 512^3 simulations, see Figure 1.5). The fluid is driven past these boxes with a randomly time varying but spatially uniform pressure gradient. After the turbulence is established, (developing all the long range correlations naturally), the boxes 'melt' and become zero velocity fluid. More detail on the turbulence generation process is provided in section 2 and in Perot [33].

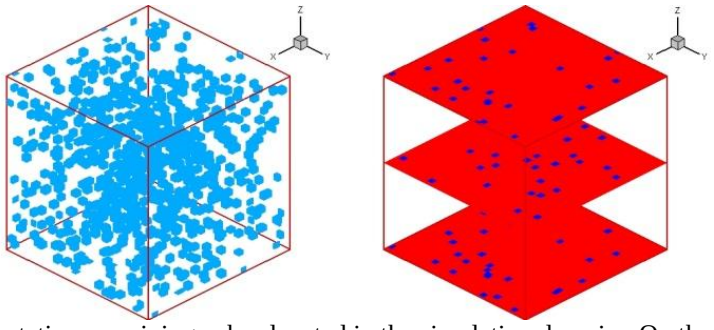

Figure 1.5 On the left, stationary mixing cubes located in the simulation domain. On the right, 2D slices in the XY-plane help to better show the mixing cube density.

Numerical simulation allows this investigation to observe the turbulence over very long times and at high temporal resolution. Some of the quantities that will be of interest, such as the decay rate, are extremely sensitive and require both high temporal resolution and long times to accurately calculate. This work follows the strategy of Parviz Moin who has long advocated the use of direct numerical simulation to investigate the fundamental physics of turbulent flows [37]. In particular, it is the logical successor

to the pressure-strain investigations of Perot and Moin [38] [39] on the return-to-isotropy process near walls. The four canonical cases studied in this work neatly define the layout of this document. Following this introductory chapter which includes a brief review of turbulence and its modeling, each case will define a chapter followed by chapters on conclusions and future work.

CHAPTER 2

TURBULENCE

2.1 Turbulence Described

Turbulence is as old as physics and thus by comparison the study of turbulence is relatively new. It is generally accepted that Osborne Reynolds' 1883 paper [40] marked the beginning of the modern study of turbulence. In this paper Reynolds describes flow visualizations and discusses a critical value for which "the motion of water in parallel channels shall be direct or sinuous" (i.e. laminar or turbulent). Rott [41] describes how later (1908) Arnold Sommerfeld [42] would present a paper on hydrodynamic stability at the 4th International Congress of Mathematicians in Rome and give this critical value the name still in use today, Reynolds number. Although Reynolds' papers of 1883 [40] and 1895 [43] are recognized as the start of the modern study of turbulence, it is only right and just to give credit to earlier known writings on turbulence. Foremost those of Leonardo de Vinci as pointed out by Richter [44] and cited by Lumley [45]. da Vinci is apparently describing the fluid motion in much the same way Reynolds is in his 1895 [43] paper where he decomposed velocity into "mean-mean motion" and "relative-mean motion", what are often today called the mean and fluctuating parts. Upon observing the motion of swirling water da Vinci wrote,

> "Observe the motion of the surface of the water, which resembles that of hair, which has two motions, of which one is caused by the weight of the hair, the other by the direction of the curls; thus the water has eddying

motions, one part of which is due to the principal current, the other to random and reverse motion."

-Leonardo da Vinci

It is a fool's errand attempting to recount all the historical endeavors which one might consider research into the nature of turbulence. The literature is vast and a number of excellent historical accounts exist. Rott [41] reviews thoroughly Reynolds' original 1883 [40] work. Jackson and Launder [46] delve deeper into the contributions of Reynolds' papers, giving accounts of the reviews of the papers by the then editor, Lord Rayleigh, as well as Sir George Stokes and Horace (later Sir Horace) Lamb. Jimenez describes Kolmogorov's numerous contributions [47]. Throughout his text P. A. Davidson [47] cites contributions due to original authors on specific topics in turbulence research, suggesting further reading at the end of each chapter. Ecke [48] delivers a condensed summary of historical work in his article "The Turbulence Problem". Some of the most in depth accounts of the history of turbulence research and the researchers themselves is given by J. L. Lumley [45] [49]. In this author's judgment the most current and thorough account of the history of turbulence research is given by Peter A. Davidson, Youkio Kaneda Keith Moffatt and Katepalli R. Sreenivasan [50].

This introduction suggests the starting point of modern turbulence research as Reynolds' classic 1883 [40] and 1895 [43] papers, with perhaps some inspiration from Leonardo da Vinci's description and illustrations of the flow of water. Reynolds' works of course are built on the foundations of Navier-Stokes equations (N-S). It should be noted here that PDEs such as N-S are the collapse of spatially continuous physical laws

and quantities, to a single point PDE, an often overlooked point that was originally intended to allow mathematicians to solve troublesome equations analytically. Although this document will focus on the theory behind various modeling methods, the methods of discretizing these PDE's for solution by numerical techniques is of great importance, not just for the physics that they represents but for the fact that the physics has been recast as single point quantities and physics does not happen at any single point in space. Physics, not surprisingly, resides in physical space and as such any equations describing physics must contain spatial consideration, Tonti [51]. Numerical solutions of course need not concern themselves with the PDE but can work directly from the discrete conserved quantities. The collapse of a spatial accounting of conserved physical quantities to PDE's, from control volumes to differential equation, and the translation of the Langrangian representation to Eularian, Wilcox [52], is meant to facilitate analytical solutions to N-S. N-S PDEs represent single point physics and as such manipulation of these PDEs yield only new single point equations. Therefore Reynolds' 1895 [43] paper which establishes Reynolds average Navier-Stokes equations (RANS) by way of the decomposition of unknowns into mean and fluctuating parts yields yet more single point physics with one more term, the gradient of Reynolds stresses, so no more physics but one more term. In order to discretize RANS a choice must be made on how to separate our unknowns in space. The technique has come full circle. Reduce Newton's second law to single point physics resulting in N-S, Reynolds decomposition N-S into RANS (single point physics). Then a discretization method must be chosen to return to accurately reconstruct the multi-point physics, Perot [53]. Harlow and Welch [54], described by Harlow [55] originally suggested the staggered mesh method in order to

properly resolve continuity. In doing so also conserved secondary physical quantities such as vorticity see Zhang [56]. Reynolds stresses, as single point physical quantities in the RANS equations, have been questioned as to their legitimacy for modeling turbulence, namely rotating flows, (Reynolds and Kassinos [22]). A vast amount of research exists into the discretization of PDEs for solution by numerical methods. As important as an understanding of these methods is, to accurate solutions to PDEs, further discussion of such methods is beyond the scope of this document.

This paper describes a number of the more widely recognized turbulence models and the theory behind them, starting with the basic turbulent viscosity models all the way up the complexity ladder to PDF methods. This introduction has mentioned the important work of da Vinci and Reynolds. Throughout the remainder of this document additional important works will be discussed in order to trace the evolution of turbulence research and modeling with an emphasis on the modeling of the slow pressure strain term in Reynolds stress transport models. It is, to be sure, not an exhaustive accounting of turbulence modeling as one can certainly follow citation after citation at infinitum. This paper does however work to establish a broad overview for the understanding of the current state of turbulence modeling with an emphasis on and culmination in prior work on incorporating turbulence structural information.

Turbulence is not easy to describe but it is easy to give examples. Atmospheric turbulence such as weather modeling, pollution transport, combustion processes, chemical engineering problems including mixing and entrainment, air flow past wind turbine blades, internal combustion engines inject a fuel-oxidizer mix into their cylinders, compresses and ignites it. All of these seemingly disparate phenomenons share a

common and complicated attribute known turbulent flow. The equations governing turbulence, the Navier-Stokes (N-S) equations can be used to exactly represent both laminar or turbulent fluid flow given the proper initial and boundary conditions. However owing to their non-linear and coupled nature they are intractable for high Reynolds number flows when discretized to a sufficient resolution at which numerical schemes can give an accurate assessment in space and time. As is with chaotic systems, the N-S equations are deterministic but extremely sensitive to initial conditions, Besnard [57]. Therefore small variations in initial conditions can lead to vastly different realizations of the flow. By analogy a raindrop landing atop the continental divide can migrate east and be carried into the Gulf of Mexico, or west and be carried into the Pacific Ocean. The determining factor could theoretically be a one molecule difference within the drop, east or west of the divide, a virtually imperceptible difference in the initial conditions resulting in vastly different outcomes.

In common engineering flows, the range of scales of turbulence can be enormous. As an example we here in the Theoretical and Computational Fluid Dynamics Laboratory have been working to model an experiment performed at NASA Ames' wind tunnel facility in California in 2000, [58]. Data was collected and a challenge put forth to the CFD community to take their best shot at modeling the experimental results with no prior knowledge of the experimental results. We have built a representative model of these experiments and are collecting data. As part of the work the ratio of largest to smallest scales (designated by a $y+ = 1$, common among numericists) has come to light. This ratio is on the order of 1 million. It is sometimes helpful to put these types of scales into human perspective so as to better appreciate the magnitude. To that end, if the smallest

scales were the size of a basketball and centered here in Amherst, the largest scales would easily reach Boston. The challenges in modeling the smallest scales in order to predict their influence on the mean flow encompass significant efforts in meshing, numerical methods, and post processing, in order to provide a cost effective and reasonably trustworthy result.

As previously mentioned the N-S equations, fully discretized spatially and temporally in order to provide reasonable results for engineering flows of interest, is intractable. Therefore in an attempt to compute turbulent flows at a reasonable cost, efforts are made to model the effects of the small scale structures of the turbulence on the mean flow with discretization that is cost effective. This is the impetus for modeling based on RANS. Reynolds averaging is solely for modeling purposes. Even Reynolds' peers at the time found his ideas challenging when he first introduced what would later become known as Reynolds averaging. Upon review of Reynolds' 1895 paper [43] on Reynolds averaging Sir Horace Lamb writes to the editor at the time, Lord Reyleigh, basically stating that the material must be good, as Reynolds basically created the field, but he couldn't understand what Reynolds was trying to convey [46]:

"I think the paper should be published in the Transactions as containing the views of its author on a subject which he has to a great extent created, although much of it is obscure and there are some fundamental points which are not clearly established."

-Sir Horace Lamb

The other reviewer, Sir George Stokes, writes to Lord Rayleigh:

"Dear Lord Rayleigh,

I enclose what Lamb meant for a draft of remarks to be submitted to the author. I think we are both disposed to say let the paper be printed, but first let some remarks be submitted to the author. There was very good work in the former paper, and there may be something of importance in this, but the paper is very obscure. In its present state it would hardly be understood."

Yours very truly,

G.G. Stokes

As incomprehensible as it was when first introduced the idea of a fluctuating velocity superimposed atop a mean velocity has been the foundation for virtually all subsequent turbulence modeling techniques.

2.2 Turbulence Modeling

A complete and accurate physical representation of a flow field as a continuum requires the numerical representation of N-S at a spatial and temporal resolution that is unreasonable for the vast majority of engineering flows. Therefore the classic shortcut is to use a spatial and temporal resolution that is economically feasible, along with a numerical representation of what is known as the Reynolds averaged Navier-Stokes (RANS) equations which will be outlined at length later in this section. The process of Reynolds averaging N-S yields an additional term involving what is known as Reynolds stresses ($R_{ij} = u_i' u_j'$) where u_i' and u_j' are the fluctuating velocities in the i and j directions respectively. This R_{ij} term is a result of the Reynolds decomposition of the advective terms within N-S.

It is generally accepted in the field that research into turbulence modeling began with the seminal papers of Reynolds 1883 [40] and 1895 [43]. Reynolds' 1883 [40]paper discussed his experiments in flow visualization in channels while his 1895 [43] paper gave us Reynolds decomposition leading to the Reynolds average Navier-Stokes equations (RANS) which are the foundation of almost all of today's turbulence models. Reynolds' 1895 [43] paper, as fundamental as it seems today, was not without speculation in its day. What is covered in 15 minutes in a present day turbulence class was, to a certain degree, confusing to even the experts of the day. Then editor of the

Philosophical Transactions of The Royal Society, Lord Reyleigh, responded to Reynolds with Sir Horace Lamb and Sir George Stokes' reviews, the opening sentence being, "The referees have found great difficulty in following the argument of this paper;"

The RANS equations described by Reynolds' 1895 [43] begin from the N-S equations which are deterministic and exactly describe the time dependent motion of fluid (i.e. the rate of change of momentum at each point in a viscous fluid). In principal once the initial and boundary conditions are known the evolution of dependent variables namely u and p can be tracked exactly. However the effects of nonlinearity and coupling result in dependent variables that are extremely sensitive to initial conditions such that after a short time, realizations with seemingly identical (beyond our ability to measure) initial conditions will look nothing alike. N-S is the implementation of Newton's second law $F = ma$ on fluid flow which is an extension of Euler's equations which do not take into account viscous forces. Reynolds' insight was to substitute a mean and fluctuating part for the instantaneous dependent variables. Starting with N-S (conservation of mass and momentum), which when considering constant density, become the continuity and momentum equations (density drops out of mass equation to become the continuity equations and density is absorbed into p). Additionally kinematic viscosity is substituted for dynamic viscosity by dividing by density ($\nu = \mu/\rho$).

$$\frac{\partial u_i}{\partial x_i} = 0 \tag{2.1}$$

$$\frac{\partial u_i}{\partial t} + \frac{\partial u_i u_j}{\partial x_j} = -\frac{\partial p}{\partial x_i} + \nu \frac{\partial^2 u_i}{\partial x_j^2} \tag{2.2}$$

Reynolds substituted as follows:

$$u_i = \bar{u}_i + u_i'$$
$$p = \bar{p} + p' \tag{2.3}$$

To obtain:

$$\frac{\partial(\bar{u}_i + u_i')}{\partial x_i} = 0 \tag{2.5}$$

$$\frac{\partial(\bar{u}_i + u_i')}{\partial t} + \frac{\partial(\bar{u}_i + u_i')(\bar{u}_j + u_j')}{\partial x_j} = -\frac{\partial(\bar{p} + p')}{\partial x_i} + \nu\frac{\partial^2(\bar{u}_i + u_i')}{\partial x_j^2} \tag{2.6}$$

Expanding and ensemble averaging each term to obtain a statistical representation of the equations, Reynolds arrived at the Reynolds averaged N-S equations (RANS).

$$\frac{\partial \bar{u}_i}{\partial x_i} = 0 \tag{2.7}$$

$$\frac{\partial \bar{u}_i}{\partial t} + \frac{\partial \bar{u}_i\bar{u}_j}{\partial x_j} = -\frac{\partial \bar{p}}{\partial x_i} + \nu\frac{\partial^2 \bar{u}_i}{\partial x_j^2} - \frac{\partial \overline{u_i'u_j'}}{\partial x_j} \tag{2.8}$$

The last term on the right hand side of Eq. (2.8) is the gradient of the famous Reynolds stresses, often represented as $R_{ij} = \overline{u_i'u_j'}$. In decomposing u and p into mean and fluctuating parts, expanding and ensemble averaging, Reynolds produced one more term with no more physics but equations that are numerically tractable. As a result the

RANS equations for turbulence are unclosed with three velocity unknowns, u_i, with $i = 1,2,3$, one pressure, p, and six components of the symmetric Reynolds stress tensor $\overline{u_i' u_j'}$ with $i = 1,2,3 : j = 1,2,3$. Unfortunately no new equations have emerged in the process and thus there exists four equations, one for each component of momentum as well as continuity. In order to close the system of equations there is a need for some sort of representations of the last term of Eq. (2.8) (i.e. a model to represent the gradient of the Reynolds stress tensor). Determining a representation for the gradient of the Reynolds stress tensor has been the foundation of virtual all turbulence modeling research. More importantly, finding representation that is computationally cost effective, applicable to a broad range of engineering applications and yields reasonable results is the task of what might be considered "solving" the turbulence problem.

Over the years there has been a diverse set of turbulence models put forth by a multitude of researchers. A complete review of these methodologies is beyond the scope of this document. However it is intended that this paper should encompass the generally accepted categories of turbulence modeling and to emphasize the strengths and weaknesses of each for the problem of anisotropic decay. While there is much literature on each type of model listed in table 2.1, and still more on large eddy simulation (LES) and direct numerical simulations (DNS), this document will give special attention to the mixing length model as well as Reynolds stress transport models (RSTM). Mixing length models are important because they are the earliest of models and as such represent the foundation upon which further developments in turbulence modeling has been built, laying the groundwork for understanding 1-equations and 2-equation models. RSTM are a departure from the aforementioned models in that they forgo the use of the intrinsic

assumption, that the Reynolds stresses are directly proportional to the mean shear and instead work to model the spatial and temporal evolution of R_{ij}. In discussing the shortcomings of RSTM the need to understand the structure of turbulence and the role that structure plays in return-to-isotropy and turbulent kinetic energy decay will be unveiled. Finally, more advanced modeling techniques will be discussed. In particular, probability density function (PDF) methods and their application to modeling both the mean velocity and Reynolds stresses, the first and second moments of the Eulerian PDF of velocity.

Model	Specified fields	Fields from differential Eq. Used in modeling	Primary quantities modeled
Mixing length	l_m	$\frac{\partial \bar{u}_i}{\partial x_i}$	$\overline{u_i' u_j'}$
1-equation (ν_t)	-	$\nu_t, \frac{\partial \bar{u}_i}{\partial x_i}$	$\overline{u_i' u_j'}, \frac{\bar{D}\nu_t}{\bar{D}t}$
1-equation ($k - l_m$)	l_m	$k, \frac{\partial \bar{u}_i}{\partial x_i}$	$\overline{u_i' u_j'}, \varepsilon$
2-equation ($k - \varepsilon$) isotropic viscosity nonlinear viscosity algebraic stress	-	$k, \varepsilon, \frac{\partial \bar{u}_i}{\partial x_i}$	$\overline{u_i' u_j'}, \frac{\bar{D}\varepsilon}{\bar{D}t}$
Reynolds stress	-	$\overline{u_i' u_j'}, \varepsilon, \frac{\partial \bar{u}_i}{\partial x_i}$	$\overline{u_i' u_j'}, \frac{\bar{D}\varepsilon}{\bar{D}t}$

Table 2.1 Attributes of RANS turbulence models. Adapted from Pope [59].

2.2.1 Mixing Length Models ("algebraic" or "zero-equation" models)

The earliest turbulence model by Prandtl, the mixing length model, is also known in modern parlance as an algebraic or zero-equation model. Where algebraic or zero-equation means that no additional equation(s), that is PDE(s), for the transport of any

quantity have been added to the system of equations in order to close it. This means that a simple algebraic, non-PDE, representation is being used for the Reynolds stresses.

In order to formulate the mixing length model Prandtl borrowed from Boussinesq's eddy-viscosity approximation the idea that Reynolds stresses (i.e. velocity fluctuations) added viscosity to the flow in a similar manner that molecular momentum transport is responsible for a fluid's dynamic viscosity μ, Wilcox [60]. Specifically, Boussinesq's idea was that if turbulence somehow causes added viscosity then perhaps the velocity fluctuations of turbulence are analogous the mean free path motion of the fluid's molecules in the derivation of viscosity. Boussinesq argued heuristically to replace the random molecular fluctuations u_i'' , u_j'' with the turbulent fluctuations, u_i' , u_j', leading to the turbulent viscosity hypothesis which suggest the turbulent stresses are proportional to the mean flow. Analysis of the molecular momentum transport process yields the definition of the viscous stress tensor $t_{ij} = -\rho u_i'' u_j''$, Wilcox [60], and which can further be evaluated to derive the shear stress resulting from molecular transport of momentum in a perfect gas as:

$$t_{ij} = \mu \frac{d\bar{u}_i}{dx_j} \tag{2.9}$$

where

$$\mu = \frac{1}{2} \rho v_{th} l_{mfp} \tag{2.10}$$

resulting in

$$t_{ij} = \frac{1}{2} \rho v_{th} l_{mfp} \frac{d\bar{u}_i}{dx_j} \tag{2.11}$$

Prandtl's took the liberty of replacing the average thermal molecular velocity v_{th} with a turbulence mixing velocity, v_{mix}, and the length of the mean free path l_{mpf} with a turbulence mixing length, l_{mix}, essentially taking a previously defined microscopic process which used intrinsic properties of the fluid, and applied macroscopic values using properties of the flow, resulting in

$$\tau_{ij} = \frac{1}{2}\rho v_{mix} l_{mix} \frac{d\bar{u}_i}{dx_j} \tag{2.12}$$

Prandtl specified

$$v_{mix} = (const.)\, l_{mix} \left|\frac{d\bar{u}_i}{dx_j}\right| \tag{2.13}$$

substituting Eq. (2.13) into Eq. (2.12)

$$\tau_{ij} = \frac{1}{2}\rho \left[(const.)\, l_{mix} \left|\frac{d\bar{u}_i}{dx_j}\right|\right] l_{mix} \frac{d\bar{u}_i}{dx_j} \tag{2.14}$$

l_{mix} is not a physical property of the fluid and thus the $\frac{1}{2}$ and $const.$ can be absorbed into it.

$$\tau_{ij} = \underbrace{\rho {l_{mix}}^2 \left|\frac{d\bar{u}_i}{dx_j}\right|}_{\mu_t} \frac{d\bar{u}_i}{dx_j} \tag{2.15}$$

Defining a turbulent viscosity as:

$$\mu_t = \rho {l_{mix}}^2 \left| \frac{d\bar{u}_i}{dx_j} \right| \tag{2.16}$$

combining Eq. (2.16) and Eq. (2.15) yields

$$\tau_{ij} = \mu_t \frac{d\bar{u}_i}{dx_j} \tag{2.17}$$

As originally shown for the analysis of molecular momentum transport and now extended to the Boussinesq approximation:

$$\tau_{ij} = -\rho\overline{u_i' u_j'} + \rho\overline{u_i' u_j'} \frac{\delta_{ij}}{3} = \mu_t \frac{d\bar{u}_i}{dx_j} \tag{2.18}$$

Rearranging we have a representation (model) for Reynolds stresses

$$\overline{u_i' u_j'} = \left(-v_t \frac{d\bar{u}_i}{dx_j} + \frac{2}{3} k\delta_{ij} \right) \tag{2.19}$$

Where

$$v_t = \frac{\mu_t}{\rho} \tag{2.20}$$

The mixing length model was one of the earliest models developed and one might say the simplest. It is however incomplete in that it requires a mixing length, l_{mix}, to be stipulated. Unfortunately one size does not fit all and the mixing length is case dependent. For simple flows where a clear length scale can be defined, such as those of boundary layers, the model performs well. However, in complex geometries, which are typically where models are needed most, the length scale is indeterminable and the modeler is forced to guess a length scale. In such situations results from the mixing length model can be woefully wrong. Therefore this type of model leaves much to be desired for flows of practical interest to scientist and engineers. By today's standards the mixing length model is not considered worthwhile as a standalone model with the availability of more cost effective physically accurate alternatives. It is however used for large eddy simulations (LES) where an inexpensive sub-grid scale model is required.

That being said it is not difficult to understand how simple models based on the turbulent-viscosity hypothesis, set forth by Boussinesq and known as the Boussinesq approximation, got their start. Experiments in pipe flow by G. Hagen (1797-1894), Anderson [61], had shown that decreasing a fluids kinematic viscosity can cause the onset of turbulence with a corresponding increase in the pressure gradient through the length of the pipe. Therefore the onset of turbulence must add some sort of viscosity to the flow. Turbulent viscosity models developed by way of the turbulent viscosity hypothesis are simple to implement by incorporating the turbulent viscosity as an addition to the fluid's kinematic viscosity. The combination of the two often referred to as an effective viscosity:

$$\mu_{effective} = \mu + \mu_t \tag{2.21}$$

2.2.2 One-Equation Models

By definition an n-equation model is a model that sets out to track the transport of n additional flow quantities beyond conservation of mass, momentum and energy. Some such quantities we will see are kinetic energy, k, in the one-equation model, and k and ε in one example of a two-equation model. To explain the one-equation model we look back at the definition of turbulent viscosity described in the previous section.

The mixing length model defines a turbulent viscosity as:

$$\mu_t = \rho {l_{mix}}^2 \left|\frac{d\bar{u}_i}{dx_j}\right| \tag{2.22}$$

Considering the myriad of possible flow configurations it can be understood that there are areas of the flow where $\left|\frac{d\bar{u}_i}{dx_j}\right|$ and therefore μ_t go to zero. Some examples are the centerline of a round jet as well as decaying turbulence behind a grid. Clearly in these situations turbulence exists and therefore some measure of turbulent viscosity should remain. Rather than estimating μ_t with values of mean shear both Kolmogorov (1942) and Prandtl (1945) (see Wilcox [60]) suggested using the velocity scale of the turbulent kinetic energy. This would eliminate the issue of vanishing turbulent viscosity in the areas of zero mean shear so long as turbulent fluctuations were present. The definition of turbulent viscosity Eq. (2.22) can be written as:

$$\mu_t = \rho l_{mix} l_{mix} \left| \frac{d\bar{u}_i}{dx_j} \right| \tag{2.23}$$

Equivalently we can define a velocity scale as:

$$u^* = l_{mix} \left| \frac{d\bar{u}_i}{dx_j} \right| \tag{2.24}$$

And thus turbulent viscosity can be defined as:

$$\mu_t = \rho l_{mix} u^* \tag{2.25}$$

The velocity scale is then alternatively defined by way of the square root of kinetic energy.

$$u^* = (const.)\rho k^{1/2} \tag{2.26}$$

And thus the turbulent viscosity is defined by way of kinetic energy.

$$\mu_\tau = (const.)\rho l_{mix} k^{1/2} \tag{2.27}$$

To define μ_t, values for $const.$ and l_{mix} still need to be estimated for each flow and more importantly k has spatial and temporal dependence and as such a transport equation is

derived for $k(x,t)$. This one-equation model, the transport of $k(x,t)$ equation, has added complexity over the simple mixing length model and thus should be able to capture more physics. It has also eliminated the issue of vanishing turbulent viscosity in regions of zero mean gradients. In developing the transport equation for k, terms for production, diffusion and dissipation are created, Pope [59].

$$\frac{\bar{D}k}{\bar{D}t} \equiv \frac{\partial k}{\partial t} + \bar{u}_i \cdot \nabla k = -\nabla \cdot T' + \mathcal{P} - \varepsilon \tag{2.28}$$

While the terms on the left side of the equation:

$$\frac{\partial k}{\partial t} + \bar{u}_i \cdot \nabla k \tag{2.29}$$

are exact (just accounting), and the production term, $\mathcal{P}$, is the result of transfer of kinetic energy from the mean flow to the fluctuating flow and is considered to be known, Pope [59].

$$\mathcal{P} = -\overline{u_i' u_j'} \frac{\partial \bar{U}_\iota}{\partial x_j} \tag{2.30}$$

It should be noted that the equation for the mean flow kinetic energy has an equal and opposite term as it gives up energy to the fluctuating part. This is analogous to the mean

flow shear giving up internal energy to the fluid by way of viscosity, but in this case the Reynolds stresses are thought of as viscosity and the mean flow shear gives up kinetic energy to the fluctuating flow. The divergence of the energy flux, $-\nabla \cdot T'$, as well as the dissipation, ε, are unknown and need to be modeled in terms of what is known. The energy flux, T', from the exact equation for transport of k is;

$$T' = \frac{1}{2}\overline{u_i' u_j' u_j'} + \overline{u_i' p'}/\rho - 2\upsilon\overline{u_j' s_{ij}} \tag{2.31}$$

Where the fluctuating rate-of-strain tensor:

$$s_{ij} = \frac{1}{2}\left(\frac{\partial u_i'}{\partial x_j} + \frac{\partial u_j'}{\partial x_j}\right) \tag{2.32}$$

This is modeled using the gradient-diffusion hypothesis which is mathematically analogous to Fick's law of molecular diffusion or Fourier's law of heat conduction, which states that the heat flux q is proportional to the temperature gradient, ∇T, with the proportionality set by the thermal conductivity of the material, K. The gradient-diffusion hypothesis uses the turbulent viscosity divided by the turbulent Prandtl number (usually $\sigma_k = 1$) as the constant of proportionality. This hypothesis postulates that there is a flux of k down the k gradient.

$$q = \mathrm{K}\nabla\mathrm{T} \qquad \text{Fourier's Law}$$

$$T' = \frac{\nu_t}{\sigma_k}\nabla k$$ Gradient diffusion hypothesis

Finally the dissipation of kinetic energy, ε, (i.e., the time rate of change k) must be modeled. As such we must find a combination of 'known' quantities that resolve to give units identical to those of

$$\varepsilon = \frac{dk}{dt} \tag{2.33}$$

that is units of:

$$\frac{length^2}{time^3}$$

While it is somewhat intuitive to attempt to model the dissipation term using the smallest scales, after all dissipation happens at the smallest scales, these scales are Reynolds number dependent and therefore change from one flow to another which of course does not lead to a general model. As shown in figure 2.1, as Re is increased the smallest scales become ever smaller, adjusting to accommodate the increased energy and dissipation needed. The size of the smallest eddies decrease and therefore the gradients they produce between one another increase allowing for greater dissipation.

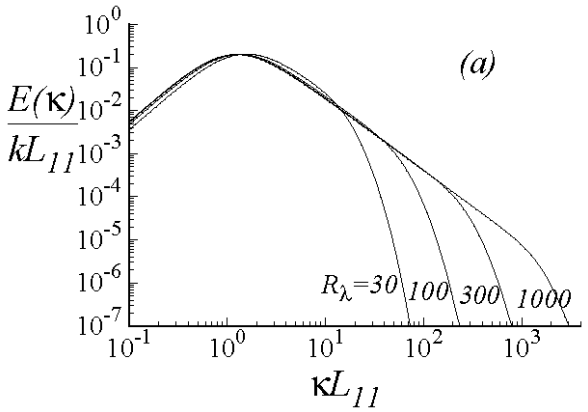

Figure 2.1 The model spectrum for various Reynolds numbers, scaled by kinetic energy, $\boldsymbol{k}$, and energy containing scale $\boldsymbol{L_{11}}$. Adapted from Pope [59].

Turbulent kinetic energy is inserted into the spectrum at the largest eddies where the length scales, l_0, are directly governed by the length scale of the geometry of the flow. Owing to the concept given to us by Richardson, that energy cascades from the larger scales to the smaller and there dissipated into heat. It is justified that we model dissipation by the energy entering the spectrum and consider it equivalent to the energy being dissipated. Thus dissipation can be modeled using a known length scale, L_{11}, where L_{11} is the integral length scale defined as:

$$L_{11}(\boldsymbol{x},t) \equiv \frac{1}{R_{11}(0,\boldsymbol{x},t)} \int_{\boldsymbol{0}}^{\infty} R_{11}(\boldsymbol{e_1},r,\boldsymbol{x},t)dr \tag{2.34}$$

In words this states that we can define the length scale of the largest eddies by integrating the two point correlations over all r and normalizing by the Reynolds stress $R_{11}(0,\boldsymbol{x},t)$. We expect the two point correlation to drop to zero as r tends toward infinity.

The dissipation length scale is defined as

$$L = \frac{k^{3/2}}{\varepsilon} \tag{2.35}$$

And thus dissipation can be defined if a suitable length scale can be prescribed. This can be done using $L_{11}(\boldsymbol{x}, t)$**,** Eq. (2.34), provided a consistent relationship between $L_{11}(\boldsymbol{x}, t)$ and L can be shown. Figure 1.5 shows just such a relationship as a function of Reynolds number.

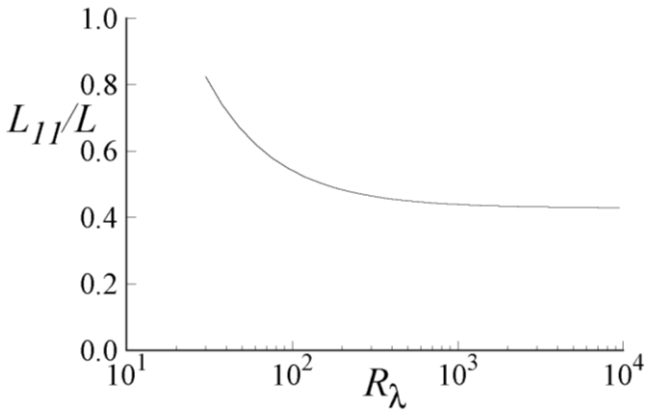

Figure 2.2 Ratio of the longitudinal integral length scale $L_{11}$to $L = k^{3/2}/\varepsilon$ as a function of Reynolds number for the model spectrum. Adapted from Pope [59].

Dissipation can therefore be modeled as

$$\varepsilon = C_D \frac{k^{3/2}}{L_{11}} \tag{2.36}$$

where C_D is a model constant. Then for convenience dissipation can be recast as turbulent viscosity by combining Eq (2.27) and Eq. (2.36), Pope [59].

$$\mu_t = (const.) C_D \, k^2/\varepsilon \tag{2.37}$$

To summarize the one-equation model the steps of this section as well as previous section on zero-equation models are retraced. Simple algebraic models require the stipulation of a velocity scale which is defined by the product of a mixing length and mean flow velocity gradient Eq (2.22). The shortcoming of this is that there are areas in the flow where the mean flow velocity gradient is zero yet turbulence is clearly present. Such a case would be at the centerline of a round jet. In order to remedy the problem Kolmogorov and Prandtl both suggest using kinetic energy as a route to velocity scale, $k^{1/2}$, as this will always be positive and can provide a measure of turbulence in areas where the mean flow gradients go to zero which empirical evidence would seem to dictate. Temporal and spatial dependent values of $k = k(x,t)$ are determined by solving a transport equation for $k(x,t)$ which, like any scalar transport equation, requires terms for production, dissipation, and redistribution, also known as energy flux, Pope [59]. However a length scale is still needed in order to determine turbulent viscosity. The next level of complexity is achieved by attempting to improve upon the model for dissipation by developing a transport equation for ε. This leads to the two-equation models such as the classic and well used k-epsilon model ($k - \varepsilon$).

2.2.3 Two-Equation Models

The idea behind the two-equation models, specifically the $k - \varepsilon$ model, is not a complete departure from one-equation models or algebraic (mixing length models). It is simply what is thought to be a better way of predicting the turbulent viscosity through an

improved estimate of a turbulent length scale and thus a more accurate representation of the evolution of the turbulent viscosity, υ_t, and thus the Reynolds stress term of the RANS. Therefore two-equation models, as well as one-equation and algebraic models, all operate under the turbulent-viscosity hypothesis that the Reynolds stresses are proportional to the mean shear, Eq. (2.19), with the proportionality given by the turbulent viscosity defined as, Eq. (2.20). Specifically, in the case of $k-\varepsilon$, ε is defined by a transport equation rather than using the integration of longitudinal velocity correlation, Eq (2.34). Harlow's scientific memoir [55] describes the impetus and introduction of $k-\varepsilon$.

As previously mentioned an n-equation model is a model that sets out to track the transport of n additional quantities beyond conservation of mass momentum and energy. As such two-equation models track the transport of two flow properties. The two-equation $k-\varepsilon$ is one of the most widely used models in commercial CFD packages.

The transport equation for k is arrived at by taking the trace of the Reynolds stress transport equation as described by Wilcox [60]. The accepted method for modeling the transport of ε does not resemble the method used for k. Efforts undertaken to derive the transport equation for ε as was done with the Reynolds stress transport equation, and thus k, become extremely cumbersome. Wilcox [60] shows the dissipation transport equation and expresses the generally accepted position with this equation. When referring to the triple correlations found in the ε transport equation Wilcox states: "These correlations are essentially impossible to measure with any degree of accuracy so that there is presently little hope of finding reliable guidance from experimentalists regarding suitable closure approximations". Libby [62] explains; "Formal derivation of a partial

differential equation for the mean viscous dissipation can be carried out by appropriate operations applied to the momentum equations…but the complexity resulting from this formal attack and the extensive and uncertain modeling needed to reduce the resulting equation to a usable one calls for a pragmatic alternative." Pope [59] explains, "The exact equations for ε can also be derived, but it is not a useful starting point for a model equation. This is because ε is best viewed as the energy flow rate in the cascade and it is determined by the large-scale motions, independent of the viscosity (at high Reynolds number). By contrast, the exact equation for ε pertains to processes in the dissipative range. Consequently, rather than being based on the exact equation, the standard model equation for ε is similar to other scalar transport equations and thus contains terms for diffusion, production and dissipation.

$$\frac{\overline{D}\varepsilon}{\overline{D}t} = \underbrace{\nabla \cdot \left(\frac{\nu_t}{\sigma_\varepsilon}\nabla\varepsilon\right)}_{diffusion} + \underbrace{C_{\varepsilon 1}\frac{\mathcal{P}\varepsilon}{k}}_{production} - \underbrace{C_{\varepsilon 2}\frac{\varepsilon^2}{k}}_{dissipation} \tag{2.38}$$

As such the transport equation for dissipation is simply a dimensionally consistent analogy to the transport of k with a time scale given by $T = k/\varepsilon$, Durbin [63], and the length scale defined as $k^{3/2}/\varepsilon$. In order to arrive at this the $k-\varepsilon$ makes the assumption that at high Reynolds numbers the dissipation and production rates are close in magnitude (i.e. energy entering the spectrum at the larger scales equals energy leaving at the dissipative scales), and from empirical observations, Pope [59] that $\left|\overline{u_i u_j}\right|/k \approx 0.3$. The constants associated with the "standard" $k-\varepsilon$ model are:

$C_\mu = 0.09$ (for v_t) $\quad C_{\varepsilon 1} = 1.44 \quad C_{\varepsilon 2} = 1.83 \quad \sigma_\varepsilon = 1.3$

The $k-\varepsilon$ model is not without limitations. In particular it has difficulties near solid walls with the dissipation term as ε^2 and k don't go to zero at the same rate. k at the wall goes to zero while ε^2 is finite and thus ε^2/k tends to infinity. Wilcox [60] proposed an alternative two-equation model, the k-omega $(k-\omega)$ model, that would specify the evolution of the time scale. Such an equation would combine the evolution equations for k and ε as $T = \varepsilon/k$ for non-homogeneous flows or $\frac{1}{T} = \omega = \varepsilon/k$.

In summary, two-equations models operate under the turbulent-viscosity hypothesis, that the turbulent fluctuations create additional viscosity, known as "turbulent viscosity", in a similar manner as that the molecular motion of fluid particles transport momentum and create kinematic viscosity. As discussed in section 1.2.2 the turbulent viscosity is modeled with the equation $\mu_t = \rho l_{mix} u^*$, or if preferred, divide through by density to obtain $\nu_t = l_{mix} u^*$. It is clear then that what is needed is a model for the l_{mix} and u^*. First , u^* is solved for by $u^* = k^{1/2}$ where k is modeled with one half the trace of the RANS equation Eq. (2.8). The length scale l_{mix} is arrived at by $l_{mix} = k^{3/2}/\varepsilon$ where ε is modeled not with a formal transport equation for ε, as this equation becomes unwieldy, but with a dimensionally consistent analogy to the transport of k as seen in Eq. (2.28) with the time scale defined as $T = k/\varepsilon$. An alternate two-equation model is the $k-\omega$. As defined by Wilcox [60] the inverse time scale is defined as $\frac{1}{T} = \omega = \varepsilon/k$. The transport equation for k remains unchanged and the ε equation is replaced with the ω equation:

$$\frac{\bar{D}\omega}{\bar{D}t} = \underbrace{\nabla \cdot \left(\frac{\nu_t}{\sigma_\omega}\nabla\omega\right)}_{diffusion} + \underbrace{C_{\omega 1}\frac{\mathcal{P}\omega}{k}}_{production} - \underbrace{C_{\omega 2}\omega^2}_{dissipation} \tag{2.39}$$

This is entirely uninteresting for homogeneous flows with (i.e. no diffusion term) as dependent variables are just being algebraically manipulated between Eq (2.38) and Eq. (2.39) using the identity $\omega = \varepsilon/k$. However with inhomogeneous flows the diffusion term has a part to play and we are taking into account gradients of the inverse time. The $k-\varepsilon$ and $k-\omega$ models have been used in concert. Mentor [64] used a blending function with $k-\omega$ near the walls and $k-\varepsilon$ in the free stream regions.

2.2.4 Reynolds Stress Models (Second-Moment Transport, Second Order Closure, Reynolds Stress Transport)

The $k-\varepsilon$ model is deficient for a number of reasons. Most notable is the fact that the Reynolds stresses are represented by way of turbulent viscosity using kinetic energy as the basis for velocity scale which does not properly represent turbulence anisotropy. In addition the turbulence is represented as directly proportional to mean rate of strain which predicts no lag between mean rate of strain and turbulence quantities. Empirical observations indicate otherwise.

Rather than attempt to solve for an eddy viscosity and model the Reynolds stresses as proportional to it, Reynolds stress models track the very transport of $R_{ij} = \overline{u_i' u_j'}$. The derivation of the Reynolds stress transport equations will not be examined in depth here. Wilcox [60] and many other texts do an excellent job covering this which culminates in:

$$\frac{\overline{D}}{\overline{D}t}\overline{u_\iota' u_\jmath'} + \frac{\partial}{\partial x_k} T_{kij} = \mathcal{P}_{ij} + \mathcal{PRS}_{ij} - \varepsilon_{ij} \tag{2.40}$$

Where the second term on the left side, the flux of Reynolds stresses, contains individual contributions due to turbulent convection, T_{kij}^{u}, fluctuating pressure, T_{kij}^{p}, and diffusion, T_{kij}^{v}, thus $T_{ijk} = T_{kij}^{u} + T_{kij}^{p} + T_{kij}^{v}$. This is done because the contribution of each is considered to be insignificant relative to the remaining terms, production, $\mathcal{P}_{ij}$, the pressure rate of strain tensor, $\mathcal{PRS}_{ij}$, and diffusion, ε_{ij}. While models are required for T_{ijk}, $\mathcal{PRS}_{ij}$, as well as ε_{ij}, modeling efforts can be focused on the pressure rate of strain tensor, $\mathcal{PRS}_{ij}$, by first considering homogeneous turbulence which sends the flux of Reynolds stresses to zero. The pressure rate of strain tensor and the flux of Reynolds stresses due to fluctuating pressure or "pressure flux", T_{kij}^{p}, are derived from the velocity pressure gradient tensor, Π_{ij}, by writing the pressure gradient tensor in conservative form, calling it the pressure transport term and decomposing it using Leibniz rule (i.e. product rule) into the velocity pressure gradient tensor and pressure rate of strain tensor as follows:

$$\frac{\partial}{\partial x_k} \underbrace{\left(\frac{1}{\rho}\overline{u_\iota p'}\delta_{jk} + \frac{1}{\rho}\overline{u_\jmath p'}\delta_{ik}\right)}_{\underbrace{T_{kij}^{(p)}}_{Pressure\ Flux\ or\ "Pressure\ Transport"}} = - \underbrace{\frac{1}{\rho}\overline{\left(u_\iota \frac{\partial p'}{\partial x_\jmath} + u_\jmath \frac{\partial p'}{\partial x_\iota}\right)}}_{\underbrace{\Pi_{ij}}_{velocity\ pressure\ gradient}} - \underbrace{\frac{1}{\rho}\overline{\left(p' \frac{\partial u_\iota}{\partial x_\jmath} + p' \frac{\partial u_\jmath}{\partial x_\iota}\right)}}_{\underbrace{\mathcal{PRS}_{ij}}_{Pressure\ Rate\ of\ Strain}} \tag{2.41}$$

In homogeneous turbulence the gradient of the pressure transport term (left side of Eq. (2.41)) is zero and therefore all redistributive terms are equivalent, $\Pi_{ij} = \mathcal{PRS}_{ij}$. It should be noted that it is common to split the terms in Reynolds stress modeling into "rapid" (linear), $\mathcal{PRS}_{ij}{}^{(r)}$, and "slow" (non-linear), $\mathcal{PRS}_{ij}{}^{(s)}$, terms. This is done by assessing the Poisson equation for fluctuating pressure using Reynolds decomposition Pope [59]. The rapid pressure rate of strain is so called because it involves mean flow gradients and thus responds immediately to changes in these gradients Pope [59]. The slow pressure-rate-of-strain term tends to be slower because it is due to nonlinear turbulence-turbulence interactions. To further reduce the complexity and isolate the pressure rate of strain tensor it is convenient to consider decaying homogeneous anisotropic turbulence. Not only does this eliminate production but as stated it results in the elimination of mean shear and thus rapid pressure-rate-of-strain, $\mathcal{PRS}_{ij}{}^{(r)}$. This allows for the evaluation of redistribution with a simplified Reynolds-stress equation.

$$\frac{d}{dt}\overline{u_i'u_j'} = \mathcal{PRS}_{ij}{}^{(s)} - \varepsilon_{ij} \tag{2.42}$$

Eq. (2.42) constitutes the time dependent redistribution kinetic energy among the individual components of $\overline{u_i'u_j'}$ or what is known as return-to-isotropy as the individual $\overline{u_i'u_j'}$ components become equal, $\overline{u_i'u_j'} \Rightarrow (2/3)k\delta_{ij}$ in the absence of production or walls.

In order to understand the modeling of return-to-isotropy it is imperative to make clear the underlying concepts of anisotropy and represent it via a quantifiable tensor.

Isotropic turbulence is defined as the equal distribution of kinetic energy among the diagonal components of the Reynolds stress tensor

$$\underbrace{R_{ij}}_{isotropic} = \frac{2}{3}k\delta_{ij} \tag{2.43}$$

where:

$$k \equiv \frac{1}{2}\overline{u_i' u_j'} \tag{2.44}$$

And δ_{ij} is the Kronecker delta defined as:

$$\delta_{ij} = \begin{Bmatrix} 1, if\ i = j \\ 0, if\ i \neq j \end{Bmatrix} \tag{2.45}$$

However in typical flows of engineering interest anisotropy is the norm. In order to evaluate such flows the individual components of the Reynolds stress tensor and their deviation from isotopic turbulence (anisotropy) must be quantified. To do so the deviatoric or anisotropy tensor is defined as:

$$a_{ij} \equiv \overline{u_i' u_j'} - \frac{2}{3}k\delta_{ij} \tag{2.46}$$

The normalized anisotropy tensor is then defined as:

$$b_{ij} = \frac{a_{ij}}{2k} = \frac{\overline{u_i' u_j'}}{\overline{u_l' u_l'}} - \frac{1}{3}\delta_{ij} \equiv \frac{\overline{u_i u_j}}{2k} - \frac{1}{3}\delta_{ij} \tag{2.47}$$

Important to effective turbulence modeling is capturing the time evolution of the normalized anisotropy tensor, db_{ij}/dt. That is, how does turbulent kinetic energy get redistributed among the individual components and return to equilibrium (return-to-isotropy). To evaluate this, the Reynold-stress equation for homogeneous, decaying, anisotropic turbulence is considered:

$$\frac{d}{dt}\overline{u_i' u_j'} = \mathcal{PRS}_{ij}^{(s)} - \varepsilon_{ij} \tag{2.48}$$

this is recast as

$$\frac{d}{dt}\left(\frac{\overline{u_i' u_j'}}{2k} 2k\right) = \mathcal{PRS}_{ij}^{(s)} - \varepsilon_{ij} \tag{2.49}$$

implementing the product rule

$$\frac{d}{dt}\left(\frac{\overline{u_i' u_j'}}{2k}\right) 2k + \frac{\overline{u_i' u_j'}}{2k} 2\frac{dk}{dt} = \mathcal{PRS}_{ij}^{(s)} - \varepsilon_{ij} \tag{2.50}$$

given the simplified flow condition, dissipation of k is

$$\frac{dk}{dt} = -\varepsilon \tag{2.51}$$

Eq. (2.47) is rearranged as

$$\frac{\overline{u_i' u_j'}}{2k} = b_{ij} + \frac{1}{3}\delta_{ij} \tag{2.52}$$

Substituting Eq. (2.52) and (2.51) into (2.48)

$$\frac{d}{dt}\left(b_{ij} + \frac{1}{3}\delta_{ij}\right)2k - \left(b_{ij} + \frac{1}{3}\delta_{ij}\right)2\varepsilon = \mathcal{PRS}_{ij}^{(s)} - \varepsilon_{ij} \tag{2.53}$$

Rearranging yields

$$\frac{db_{ij}}{dt} = \frac{\varepsilon}{k}\left(b_{ij} + \frac{1}{3}\delta_{ij} + \frac{\mathcal{PRS}_{ij}^{(s)}}{2\varepsilon} - \frac{\varepsilon_{ij}}{2\varepsilon}\right) \tag{2.54}$$

If then ε_{ij} is assumed to be proportional to $\overline{u_i' u_j'}$

$$\varepsilon_{ij} = \frac{\varepsilon}{k}\overline{u_i' u_j'} \tag{2.55}$$

We can arrive at Rotta's proposed model for $\mathcal{PRS}_{ij}^{(s)}$

$$\mathcal{PRS}_{ij}^{(s)} = -C_r \frac{\varepsilon}{k}\left(\overline{u_i' u_j'} - \frac{2}{3}k\delta_{ij}\right) \tag{2.56}$$

With his model for $\mathcal{PRS}_{ij}^{(s)}$ Rotta (1951) [65] addressed the drawbacks associated with two-equation models such as $(k-\varepsilon)$. Namely the fact that the two equation models instantaneously produce Reynolds stresses in the presence of mean shear. Two-equation models do not take into account the time evolution of turbulence. For instance the fact that large scale eddies can quickly carry Reynolds stresses to different points in the flow domain without the need for them to be produced locally. Rotta's model amounts to taking the $(k-\varepsilon)$ model and adjusting the anisotropy with a time scale to take into account the fact that the Reynolds stress anisotropy does not respond instantaneously to the mean flow.

Rotta's model effectively states that the slow pressure rate of strain is proportional, by a constant C_r, to the amount of anisotropy, a_{ij}, or $\left(\overline{u_i' u_j'} - \frac{2}{3}k\delta_{ij}\right)$. It seems logical to propose such a relation. However empirical evidence does not bear results that support the assertion that C_r is a constant. Once again, figure 1.2 shows result of Le Penven [8] and it is a clear indication that starting from two different initial conditions of turbulence anisotropy, one must use different values for C_r in the Rotta model in order to match the empirical data of decaying anisotropic turbulence.

A convenient way of visualizing return-to-isotropy is by way of an anisotropy map which displays the trajectory of return-to-isotropy. One such map, developed by Lumley and commonly referred to as the Lumley triangle, plots the 2nd and 3rd invariants of the normalized anisotropy tensor defined as:

$$II = 3\eta^2 = -(1/2)b_{ij}b_{ji} \tag{2.57}$$

$$III = 2\xi^3 = (1/3)\, b_{ij}b_{jk}b_{ki} \tag{2.58}$$

Figure 2.3 shows plots of Rotta's linear return model as well as the more general non-linear return model proposed by Sarkar and Speziale [18]. These models for decaying anisotropic turbulence suggest the initial distribution of anisotropy to follow the trajectories to the origin as shown in the plots. That is, two anisotropic conditions that at any time during the decay occupy the same point in space on the invariant plot should return to the origin along the same trajectory. Empirical data from Perot [66] indicate that neither Rotta's linear return model nor Sarkar and Speziale more general non-linear model properly capture the return process.

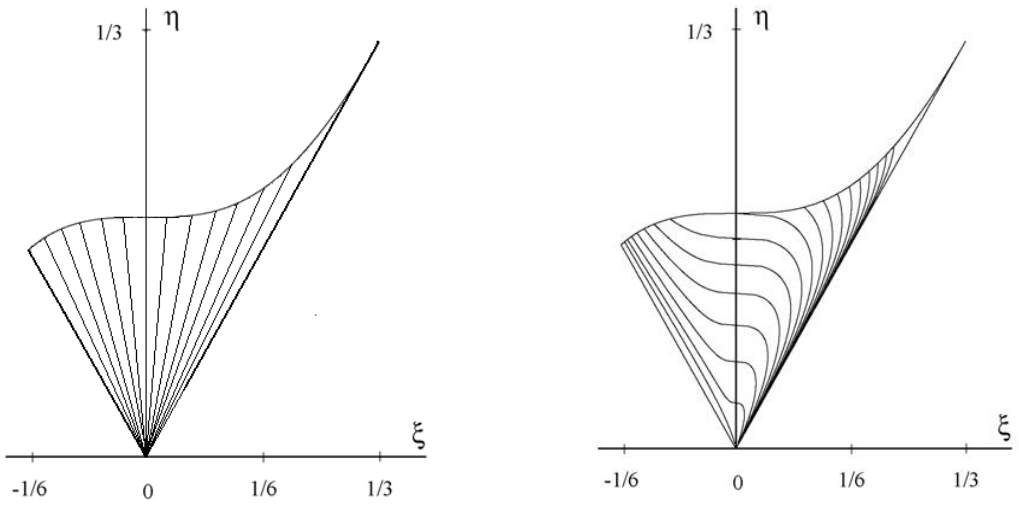

Figure 2.3 (a) Return trajectories predicted by Rotta's linear return model [65]. (b) Trajectories predicted by the nonlinear model of Sarkar and Speziale [18]. Adapted from Pope [59].

As discussed by Pope [59], Sarkar and Speziale [18] took a more general approach than Rotta in order to come up with their nonlinear model. If it is assumed that the slow pressure rate of strain tensor is proportional to some function dependent on characteristics of the flow and fluid properties, it can be envisioned that

$$\mathcal{PRS}_{ij}^{(s)} = \mathcal{F}_{ij}^{(1)}\left(\overline{u_i' u_j'}, \varepsilon, \nu\right) \tag{2.59}$$

or in non-dimensional form as

$$\frac{\mathcal{PRS}_{ij}^{(s)}}{\varepsilon} = \mathcal{F}_{ij}^{(2)}(\mathbf{b}, \mathrm{Re_L}) \tag{2.60}$$

where $Re_L = k^2/(\varepsilon\nu)$. Even further generalization can be achieved by assuming

$$\mathcal{F}_{ij}^{(2)} = \sum_n f^{(n)}\, T_{ij}^{(n)} \tag{2.61}$$

where $T_{ij}^{(n)}$ represents every possibility of deviatoric tensor formed by **b** and $f^{(n)}$ coefficients thereof. Pope [59] continues with further manipulation by way of the invariants of the anisotropy tensor and the Cayley-Hamilton theorem to arrive at

$$\frac{k}{\varepsilon}\frac{db_{ij}}{dt} = \left(1 + \frac{1}{2}f^{(1)}\right) b_{ij} + \frac{1}{2}f^{(2)}\left(b_{ij}^2 - \frac{1}{3}b_{kk}^2\delta_{ij}\right) \tag{2.62}$$

As can be seen, Eq. (2.62) contains nonlinear terms and thus the trajectories within a return-to-isotropy map such as Lumley's become more interesting than those of Rotta's linear model. However due to the fact that no new information has been incorporated into the derivation of the nonlinear return model, only $\overline{u_i' u_j'}, \varepsilon, and\ \nu$ were used, one cannot hope to achieve trajectories that cross as is shown in figure 2.4.

Results such as those shown in figure 2.4 indicate that more information than the current state of anisotropy (i.e. the magnitude and relative values of the Reynolds stresses) is required to describe the isotropic decay of turbulence. There exist a handful of models that take into account the structure of the turbulence in an attempt to improve the prediction of return-to-isotropy. Some such models are the Oriented-Eddy Collision model, as described by Martell and Perot [1]. Models by Besnard [20], Van Slooten and Pope [23], Kassinos and Reynolds [22], Saffman and Pullin [67] use structure to predict the fast pressure strain but no to predict the slow pressure strain and therefore the return-to-isotropy.

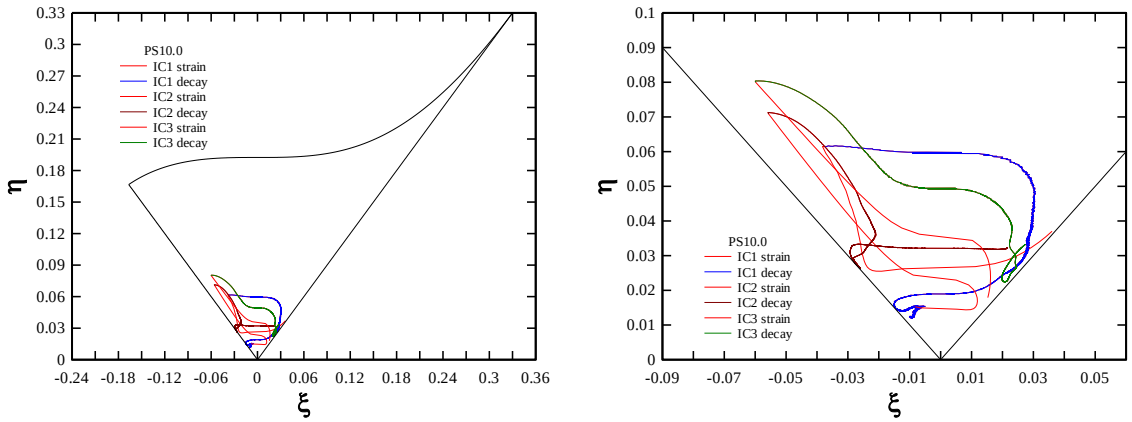

Figure 2.4 The effect of initial conditions. Isotropic turbulence subjected to plane strain and its subsequent decay (return-to-isotropy).

2.2.5 Probability Density Function (PDF) Methods

PDF methods differ fundamentally from previously described methods in that they aim to describe the dynamics of the turbulence by way of statistics. More specifically PDF methods use statistical distributions as a representation for the properties of each fluid particle within the domain of interest. For the sake of a simplified introduction it is safe to visualize a Gaussian distribution as the shape of a given PDF. In its simplest form a PDF represents the probability that a fluid particle at a specific location will have a specific velocity at a specific time $f(v_i, x_i, t)$. From an Eulerian point of view imagine that for every location in space a PDF exists that describes the properties of that location's current fluid particle. Similarly, a Lagrangian view point would track a given particle through space and time and its assigned PDF would evolve to represent its properties. From the PDF we can back out useful quantities of interest. Multiplying by velocity and integrating over velocity space we can arrive at the mean velocity:

$$\bar{u}_i = \int_{v_i} v_i f(v_i, x_i, t) dv_i \tag{2.63}$$

Where $\int_{v_i} dv_i$ is the triple integral in velocity space with $i = 1,2,3$. Additionally we can arrive at the Reynolds stress tensor:

$$\overline{u_i' u_j'} = \int_{v_i} (v_i - \bar{u}_i)(v_j - \bar{u}_j) f(v_i, x_i, t) dv_i \tag{2.64}$$

Owing to the fact that PDF methods are based on the statistics of many possible particles it is necessary to discuss an evolution equation for such a continuum. In order to do so the Boltzmann equation is introduced:

$$\frac{\partial}{\partial t} f(v_i, x_i, t) + v_i \frac{\partial}{\partial x_i} f(v_i, x_i, t) + a_i \frac{\partial}{\partial v_i} f(v_i, x_i, t) = \frac{\partial}{\partial t} f(v_i, x_i, t)|_{collisions} \quad (2.65)$$

The Boltzmann equation describes how a PDF evolves as a result of the collisions of every particle in the system. The left hand side of Eq. (2.65) is exact in that it simply accounts for the evolution of the PDF with the third term representing body forces such as gravity or Coriolis effects. The single term on the right side of Eq. (2.65) represents the summed effects of all particle collisions. There is a physically "correct" representation of the collision term but it involves tracking every particle. Although theoretically accurate it is an exercise in futility from an engineering standpoint as it is simply not tractable for any flow of interest. Rather than track all the particles a model can be employed to represent the resulting behavior or average of all the collision (i.e. a model for the collision term). In 1954 Bhatnager, Gross and Krook [68] (BGK) came up with one of the simplest of models for the collision term:

$$\frac{\partial}{\partial t} f(v_i, x_i, t) + v_i \frac{\partial}{\partial x_i} f(v_i, x_i, t) + a_i \frac{\partial}{\partial v_i} f(v_i, x_i, t) = -\frac{1}{\tau}\left(f(v_i, x_i, t) - f^{eq}(v_i, x_i, t)\right) \quad (2.66)$$

Where τ is the intrinsic turbulent time scale, $f(v_i, x_i, t)$ is the current particle distribution function and $f^{eq}(v_i, x_i, t)$ is the equilibrium distribution function (the Boltzmann-Maxwellian distribution function with a half width of $2k/3$) Chen, [69]. As f evolves toward f^{eq} the effect of the collision model, the right hand side of Eq. (2.66), tends toward zero which is of course not a good representation of turbulence. This model produces a constant viscosity related to the inverse time scale, $1/T$.

The next level of complexity for modeling the collision term aims to eliminate the evolution to zero of the collision term seen in BGK. The Fokker-Planck equation:

$$\frac{\partial}{\partial t} f(v_i, x_i, t) + v_i \frac{\partial}{\partial x_i} f(v_i, x_i, t) + a_i \frac{\partial}{\partial v_i} f(v_i, x_i, t) = - \underbrace{\alpha \frac{\partial}{\partial v_i} (v_i - U_i) f(v_i, x_i, t)}_{drift} + \underbrace{\beta \frac{\partial^2}{\partial v_i^2} f(v_i, x_i, t)}_{diffusion} \quad (2.67)$$

which includes a "drift" term allowing the mean of the PDF to move toward a new value but also causing an increase in kurtosis or peakedness in the distribution due to the fact that random fluctuations are being removed from the distribution. To counteract this decaying effect of the drift, a second "diffusion" term is included which adds zero-mean random walk increments of standard deviation. Coefficients lay in front of both the drift and diffusion terms and getting these coefficients correct in order to properly represent turbulence is the goal. For the turbulence these coefficient require a more general form and are themselves tensors.

The use of Fokker-Planck as effective tool for the evolution of the PDF to represent turbulence quantities is only as good as the collision term model. The Langevin equations can be used as a way to numerically compute PDF equations.

The Langevin equation is defined as:

$$dU^*(t) = -U^*(t)\frac{dt}{T_L} + \left(\frac{2\sigma^2}{T_L}\right)^{1/2} dW(t) \tag{2.68}$$

And its finite difference counterpart as:

$$U^*(t+\Delta t) = U^*(t) - U^*(t)\frac{\Delta t}{T_L} + \left(\frac{2\sigma^2 \Delta t}{T_L}\right)^{1/2} \xi(t) \tag{2.69}$$

The Langevin evolves in what is known as an *Ornstein-Uhlenbeck* (OU) process. This process is a statistically stationary, Gaussian, Markov process with continuous sample paths that are nowhere differentiable with an autocorrelation function described by:

$$\rho(s) = e^{-|s|/T_L} \tag{2.70}$$

Which when compared to DNS data shows good agreement, Pope [59]. Figure 2.6 shows five realizations of a stochastic path, OU process of $U^*(t)$, generated from the Langevin equation as well as agreement between the autocorrelation of the OU process and the structure function (autocorrelation in time) extracted from DNS data.

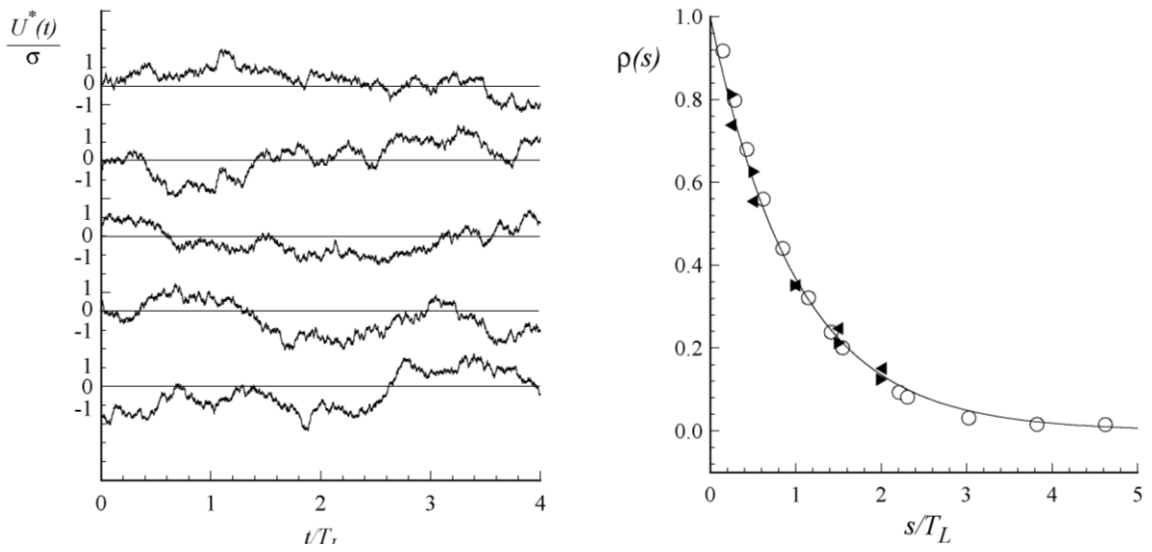

(a) (b)

Figure 2.5 (a) Realizations of stochastic sample paths of *Ornstein-Uhlenbeck* (OU) process. (b) Line, Langevin model autocorrelation $\rho(s) = e^{-|s|/T_L}$: solid symbols, experimental data of Sato and Yamamoto (1987) ►$R_\lambda = 46$, ◄ $R_\lambda = 66$, ○ DNS data of Yeung and Pope (1989), $R_\lambda = 90$ adapted from Pope [59].

Figure 2.5 (b) makes a powerful statement allowing for the two parameters of the Langevin Eq. (2.69), σ^2, and $1/T_L$, to be expressed as the properties of turbulence, ε and k. This is accomplished through the comparison of structure functions define by the Kolmogorov hypotheses and that of the Langevin equation, Pope [59]. Therefore a heuristic, stochastic process can be combined with empirical data to yield a PDF representation for a particle's velocity.

In summary, the Langevin equation is a statistical representation of how a particle's velocity might fluctuate with time. Its validity is supported by empirical data (DNS) as shown in figure 2.5 (b). A PDF of this Langevin's OU process can then be generated, represented as $f_L^*(V;t)$. Using the Fokker-Planck equation the evolution of the PDF through space and time can then be evaluated, keeping in mind that at any time Eq. (2.63) and (2.64) are available to recover the meaningful turbulence values of mean velocity and Reynolds stresses.

Since their introduction the most commonly used PDF method is that developed by Pope [70]. Perot took Popes use of PDF methods a step further. Pope's PDF methods only use PDFs dependent on position, velocity, and time, $f(x_i, v_i, t)$. Perot added to this the turbulence's structure in the form of eddy orientation, $f(x_i, v_i, t, q_{ij})$. Others before Perot had used the idea of including structure, D. Besnard, F. Harlow, R. Rauenzahn, C. Zemach [20] but not via PDF methods. It should be noted that no matter what one does with Pope's PDF method the results are still going to be a function of single point velocity fluctuation because that is all that was ever include in the PDF representation at the outset. So structure, if one is to use it, must be included at the outset as one of the probabilities that the distributions depends on. In this way an evolution equation for velocity fluctuations can be generated that takes structure into account. When considering the importance or effect of structure on turbulence modeling it is instructive to consider the possible Reynolds stress distributions within a given domain of turbulence as these Reynolds stress tensors are the basis for most turbulence modeling today. Isotropic turbulence can be represented by randomly fluctuating velocity fields that are identical in each coordinate direction. Consider for example figure 2.6(a) which depicts a measured turbulent velocity. If this same velocity distribution were to be measured in each coordinate direction the turbulence would be considered isotropic. What is often overlooked however is the fact that any combination of figure 2.6(a) through (e), aligned in the individual component directions would also result in isotropic turbulence owed to the fact that each plot's RMS value is identical. Take a specific case where the R_{11}= 1.9(a), R_{22}= 1.9(c), and R_{22}= 1.9(e). These are three very different distributions but each is represented by the same Reynolds stress value. Now it becomes easier to envision that

structure may need to be incorporated into turbulence modeling in order to properly capture return-to-isotropy. As can be imagined, if Reynolds stresses of the same value can be derived from vastly different velocity distributions, anisotropic turbulence certainly can. Based solely on heuristic arguments it seems natural that decaying anisotropic turbulence, with differing velocity distributions would naturally lead to different patterns of decay. As a difference in decay would be imagined between cases of the (R_{11}= 13(a), R_{22}= 13(a), R_{22}= 13(a)) and (R_{11}= 13(a), R_{22}= 13(c), and R_{22}= 13(e)) and these two cases would not traverse the Lumley triangle along the same trajectory.

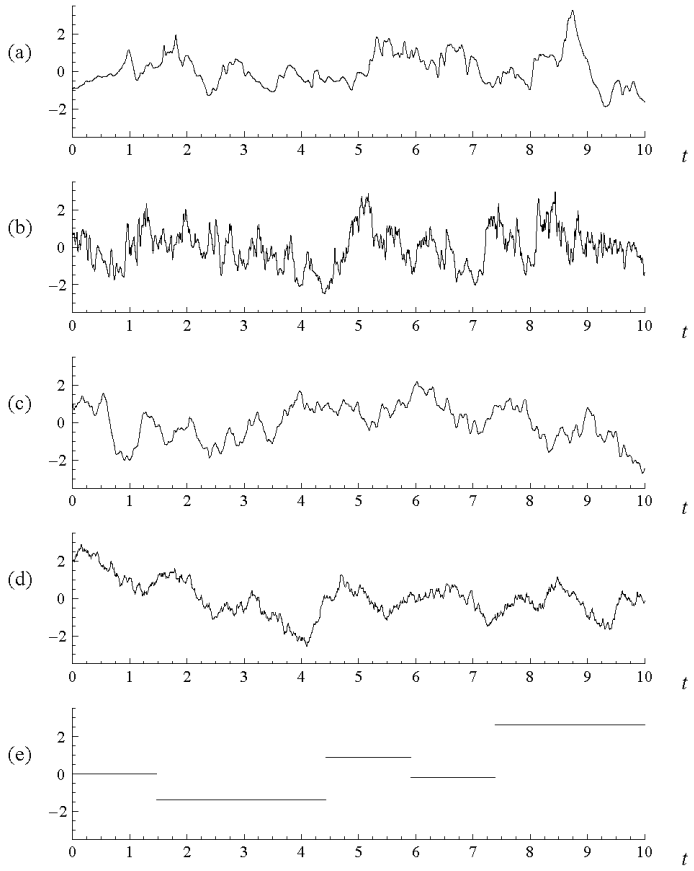

Figure 2.6 Sample paths of five statistically stationary random processes. The one-time PDF of each is a standardized Gaussian. (a) A measured turbulent velocity. (b) A measured turbulent velocity of a higher frequency than that of (a). (c) A Gaussian process with the same spectrum as that of (a). (d) An Ornstein-Uhlenbeck process with the same integral timescale as that of (a). (e) A jump process with the same spectrum as that of (d). Adapted from Pope [59].

CHAPTER 3

SIMULATION METHODOLOGY

3.1 Numerical Method

The incompressible Navier-Stokes equations with constant viscosity are solved with the classic 2nd–order Cartesian staggered mesh spatial discretization of Harlow & Welch [54]. A 3-step and 2nd-order low-storage Runge-Kutta method is used for time advancement. The pressure and incompressibility constraint are enforced by using the classic fractional step method [71] or the exact projection method [72]. The inviscid, no penetration, boundary condition is directly enforced on mixing box walls with this discretization because the normal velocity flux on a wall is a primary unknown of the method. The viscous no-slip condition on walls is enforced by choosing velocity gradients on the wall so that the tangential velocity goes to zero on the wall.

This numerical discretization has been widely used for turbulence simulations when complex wall boundary conditions are present (see Perot & Moin [38], Le & Moin [73], Martell *et al.* [74] and the references therein). This method is favored because it not only conserves mass and momentum like finite volume and spectral methods but because it also conserves physically important secondary variables such as vorticity and kinetic energy. The kinetic energy cascade is central to the correct physical prediction by any DNS simulation, so it is attractive to know that this discrete system respects the energy and vorticity physics of the Navier-Stokes equation system. The method is validated in section 2.3. Numerical methods with attractive secondary conservation properties are

discussed extensively in Perot [53], and a general methodology for generating such discretizations can be found in Perot and Subramanian [75].

Fourier spectral methods are common in DNS simulations of turbulence, and were used for all the previously cited simulations of plane-strain turbulence. However, in the situation where turbulence arises physically from mechanical stirring and it is not imposed as an *ad hoc* initial condition or due to a forcing term, Fourier spectral methods are not appropriate. The required wall boundary conditions cannot be imposed with an inherently periodic Fourier spectral method. The reader should also be strongly cautioned about assuming that Fourier methods are significantly more accurate than a physics capturing (mimetic) 2^{nd} order method for DNS simulations. In DNS, the solutions are not sufficiently resolved to a level where only the leading order error of a Taylor series expansion matters. All error terms are relevant in DNS, not just the leading order one in the Taylor series expansion. The described method resolves small scale fluctuations (dissipation spectra) as well as FFT based methods with the same resolution (section 2.3).

3.2 Turbulence Generation

The generation of the turbulence is a important component of this work because the large scale correlations have a direct affect on the decay process. It is therefore important that those large scales arise from some physical process (such as mixing by cubes) and are not being directly imposed by any human choices about the initial conditions or the large scale forcing. For the simulations shown in this work 768 small

no-slip cubes are randomly distributed throughout the domain (for the 512^3 cases). These small mixing cubes fill less than 2% of the total fluid volume (see figure 2.1).

The cubes remain fixed in place and the turbulence is generated by imposing an external, constant in space, acceleration. This is equivalent to performing the calculation in a time varying linearly accelerating reference frame (shaking). The direction of this acceleration is changed randomly every 0.3 seconds, but its magnitude is specified by the user. The shaking time scale is much less than the initial large eddy timescale (which is on the order of 2.0), but long enough to create a wake behind each cube that is sufficiently long enough to interact, on average, with a neighboring cube. A typical value of the acceleration is 100 cm/s^2 (or about 1/10 the acceleration of gravity). The shaking is performed for 5.1 seconds in most simulations (or 17 different accelerations). The primary acceleration (shaking) is then turned off and a restoring acceleration, $\boldsymbol{a_{return}}$, is allowed to act for another 1.9 seconds. After 1.9 seconds the restoring acceleration (which is exponentially decaying in time) causes the mean flow to be extremely close to zero. A mean flow of zero is not necessary for the code, but it does allow the simulation to take slightly larger time steps (by minimizing the CFL stability criteria), and it does seem to lead to better statistical accuracy at very long times when the fluctuations can become smaller than the mean flow. During this 1.9 second period the turbulence changes from being accelerated to being in isotropic decay. At the end of this period (at a time of 7) the boxes instantaneously turn into zero velocity fluid. It tends to take about one or two large-eddy turnover times for the surrounding turbulence to fully merge with (chew up) the small regions of zero velocity fluid where the stirring boxes used to be. The flow tends to behave like ideal (Saffman, k^2) decaying turbulence by a time of 12.

Figure 3.1 is a pictorial representation of the turbulence generation process (Stages 1 – 2) followed by the straining (Stage 3) and decay (Stage 4) for the case of axi-symmetric contraction.

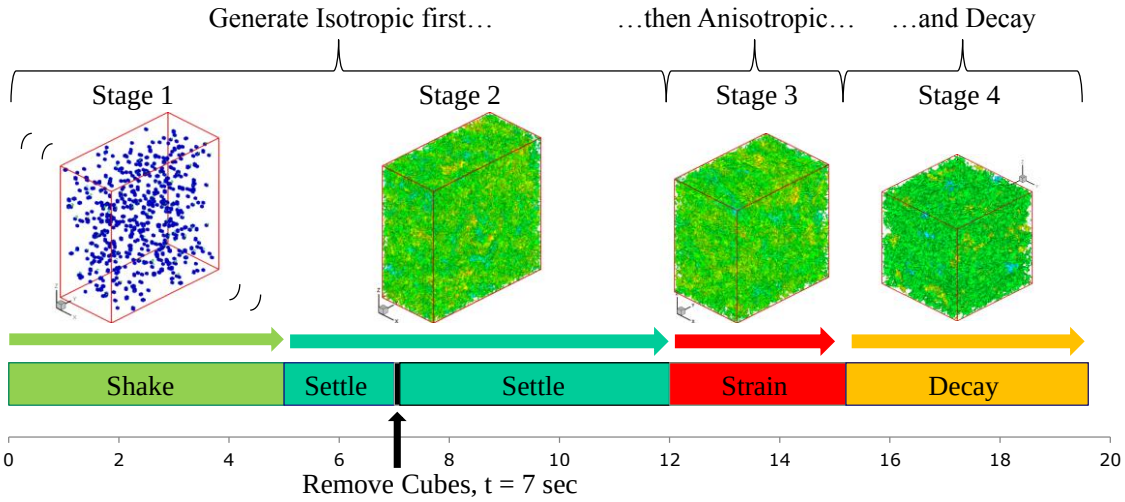

Figure 3.1 Generating isotropic and anisotropic turbulence. Stage 1: 'Shake' domain (t = 0 - 5). Stage 2: Allow for settling (t = 5 – 7), remove stirring cubes (t = 7), and allow for additional settling (t = 7 – 12). Stage 3: Strain (t = 12+). Stage 4: Allow for decay and return-to-isotropy.

Physical units are not needed by the computer, but can be helpful for the reader, and make the discussion simpler. If the simulated fluid is water at standard temperature and pressure (with $\nu = 10^{-2}$ cm^2/s) then the domain size (after straining) is a cube that is 48 cm on a side. The small cubes that stir the turbulence are 1.4 cm on a side. And in the 512^3 simulations there are 768 of them randomly placed in the domain. The total volume of all the stirring elements is therefore 1.93% of the total simulation volume. The mesh size itself is 0.9375 mm (which is 1/15th of the stirring cube size). At early times in the simulation, the timestep can be as small as 1/1000th of a second. In all the simulations it is never larger than a 1/10th of a second. All the simulations run out to a time of roughly 100 seconds. More details can be found in reference [33].

3.3 Validation

An example of the 3D energy and dissipation spectra generated by the stirring process is shown in figure 2.2(a) and 2.2(b) at a time of 12 seconds. Data for these plots is generated from the plane strain case (solid black lines) but similar results appear in each of the canonical cases performed. This snapshot of the energy spectra is taken 5 seconds after the stirring boxes have been removed and at the point in which the kinetic energy decay exponent has asymptoted to its theoretical value of 6/5. These spectra are compared with other simulations and experiments with symbols being data from the second measurement station of Comte-Bellot and Corrsin [36] (tU/M = 98) and dashed lines being data from a simulation by Wray [76]. The Comte-Bellot and Corrsin experiments have a Taylor microscale Reynolds number of 65.3 at this measurement station while the plane strain example has a Taylor microscale Reynolds number of 50.8.

The peaks of the simulation and the Wray data have been scaled to match the peak in the experimental data. The wavenumbers were scaled to have the same Kolmogorov length scale $L_\eta = \left(\nu^3/\varepsilon\right)^{1/4}$. Both the low wavenumber and high wavenumber (dissipation spectra) are well captured. de Bruyn Kops and Riley [35] also computed this Reynolds number with a spectral code and 512^3 mesh points, with very similar results.

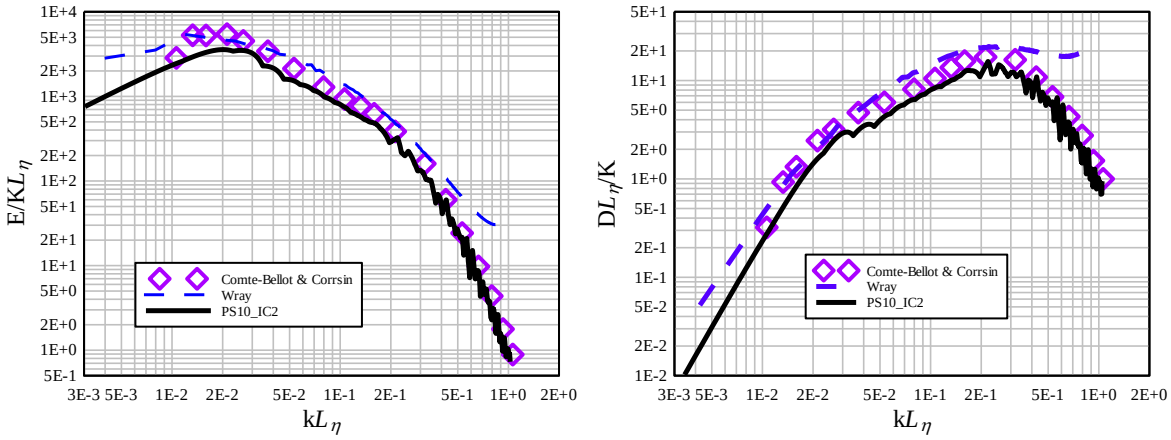

(a) (b)

Figure 3.2 (a) Energy spectra. (b) Dissipation Spectra. Solid lines current simulations. Symbols Comte-Bellot & Corrsin [36] at tU/M=98 (second station). Dashed lines spectral 512^3 simulation by Wray [76].

3.4 Moving Mesh for Straining

When the fluid is being strained, the simulations are performed on a moving mesh that moves with the mean flow. The incompressible Navier-Stokes equations in an arbitrary moving reference frame, moving with a velocity $\boldsymbol{v}$, are

$$\frac{d\boldsymbol{u}}{dt} + (\boldsymbol{u} - \boldsymbol{v}) \cdot \nabla \boldsymbol{u} = -\nabla p + \nu \nabla^2 \boldsymbol{u} \tag{3.1}$$

The equation for the mean velocity, which for the case of plane strain is constant in time and varies linearly in space, then becomes.

$$(\overline{\boldsymbol{u}} - \boldsymbol{v}) \cdot \nabla \overline{\boldsymbol{u}} + \nabla \cdot (\overline{\boldsymbol{u}'\boldsymbol{u}'}) = -\nabla \bar{p} \tag{3.2}$$

The second term is zero for plane strain where the turbulence is homogeneous, and for these simulations the reference frame moves with the mean flow ($\boldsymbol{v} = \overline{\boldsymbol{u}}$), so the

first term is also zero. This means that the mean pressure is spatially constant (and set to zero for simplicity). As a result of Eq. (3.2), the equation for the fluctuating velocity, u'_i, in a moving frame is (in Cartesian tensor notation):

$$\frac{du_i'}{dt} + u_j' u_{i,j}' + u_j' \bar{u}_{i,j} = -p_{,i}' + \nu \nabla^2 u_i' \tag{3.3}$$

This has a form similar to the Navier-Stokes equations but with an extra source term (third term on the left hand side) that is due to the mean flow. By example, in the case of of plane strain the mean velocity gradient tensor is a diagonal tensor and the result of this extra term is to cause exponential decay for the x-direction fluctuations and exponential growth of the y-direction fluctuations. Incompressibility, diffusion, and advection, then modify this forcing term. In the RDT limit, the mean gradient forcing term is large and only the pressure is large enough to modify its effects.

Eq. (3.3) uses essentially the same transformation used by Rogallo [14], but the implementation looks very different because Rogollo's equations are first transformed into wavespace. Solution for the fluctuations rather than the total velocity is attractive because it allows one to use periodic boundary conditions for the sides of the simulation domain. In plane strain the total flow is not periodic because the mean flow is not periodic, but the fluctuating velocity and pressure fields can be represented as periodic fields.

The simulation methodologies described within this chapter are consistent across all of the simulations examined in the present body of work. The chapters that follow deliver results arising from the various canonical cases considered.

CHAPTER 4

PLAIN STRAIN

4.1 Overview

Direct numerical simulation is used to evaluate the effect of plane strain on isotropic homogeneous turbulence. The subsequent return-to-isotropy, after the removal of the strain, is also investigated. Large, moderate, and small strain rates are computed at moderate turbulence Reynolds numbers. The initial turbulence is generated via mechanical mixing so that the large scale turbulence develops relatively naturally. Turbulence length scales, Reynolds numbers, decay rates, and anisotropy are computed over the range of the simulations, with the goal of quantifying how anisotropic decay behaves. The simulations indicate that large scale anisotropy may not decay to zero at very large times. In agreement with experimental data, the presence of a recovery region is discerned before the return process is observed. Trajectory crossing is observed on the anisotropy invariant map indicating that anisotropy itself is not sufficient to determine its time evolution. Model constants for classic return-to-isotropy models are determined from the data and shown to vary considerably. The Oriented-Eddy Collision (OEC) model [1], which includes turbulent structure information, is shown to predict the salient structure of the straining and return process.

4.2 Introduction

Isotropic turbulence subjected to plane strain is a canonical case for investigating the fundamental properties of turbulence and for developing turbulence models. Under

the influence of plane strain, the mean velocity stretches the fluid in one direction while compressing it in another, orthogonal direction, at a rate that makes the mean flow incompressible. In this work, stretching occurs in the x direction while compression is in the y direction. The mean velocity during the strain is therefore $u = Sx$ and $v = -Sy$ where S is a constant. This type of mean flow is found in 2D stagnation point flows. The classic example is the leading edge of a wing or turbine blade. The flow is interesting for this practical application but also because it is perhaps the simplest incompressible turbulent flow that involves a mean flow gradient. This turbulent flow is the next step up in complexity from decaying isotropic turbulence.

Experiments of plane strain and the return-to-isotropy have a long history dating from the experiments of Townsend [77] in 1954 that used a 4:1 straining ratio. These experiments were followed by those of Tucker and Reynolds [78] [79] who used a higher straining ratio (6:1). Over a decade later, Gence and Mathieu [12] performed further experiments of plane strain and its subsequent return-to-isotropy. Le Penven et al. [8] performed two experiments, one of which was close to plane strain in order to show that the simple Rotta model [65] for return-to-isotropy was inadequate. Choi and Lumley [10] and Lumley and Newman [9] used these prior experiments as well as their own to propose models for return-to-isotropy.

Perhaps the first numerical simulations of plane strain were performed by Kwak [80] in his Ph.D. thesis completed in 1975. Those simulations, at 16^3 and 32^3 mesh resolutions, were soon replaced by larger calculations using 128^3 meshes. For example, Rogallo [14] in 1981 demonstrated the moving mesh numerical approach that will also be used in this work (though with a very different numerical method). Then in 1985, Lee

and Reynolds [81] performed 128^3 simulations for a variety of different strain configurations that are still used widely today. Lee and Reynolds suggested that small scale anisotropy relaxes rapidly initially but then relaxes with the large-scale anisotropy over longer time scales. Rogers and Moin [82] looked at the instantaneous flow structures in those configurations. More recently (2001) Barre at al. [83] have performed 96^3 DNS simulations of particle laded turbulent plane strain.

In the simulations performed for this work the initial domain in which the stirring boxes reside and in which the turbulence is initially generated is shorter in the x-direction and is given by $L_x^{initial} = L_z e^{-ST}$ where T is the total straining time. Similarly, the initial domain is longer in the y-direction and is given by $L_y^{initial} = L_z e^{+ST}$. The domain (and mesh size L_z) in the z-direction remains fixed. The initial domain and mesh is shown in figure 4.1(a). As the turbulence is strained the domain grows in the x direction and shrinks in the y direction, figure 4.1(b). Finally, at the end of the straining period the domain is perfectly cubic, figure 4.1(c). Different strain rates can be used with the same initially distorted mesh. What must remain constant is the product of strain rate, *S*, and the duration of the strain, *T*. For the computed plane strain cases in this work, $ST = 0.5$ with all straining starting at time = 12 seconds. A strain S = 0.625 1/s, strains until 12.8 seconds ($ST = 0.5$), S = 0.3125 1/s strains until 13.6 seconds, S = 0.15625 1/s until 15.2 seconds, S = 0.0625 1/s until 20 seconds and the case with S = 0.025 1/s strains until 32.0 seconds. After the domain becomes cubic in shape the strain is turned off. The resulting anisotropic turbulence now decays without strain, and with no more motion of the underlying mesh.

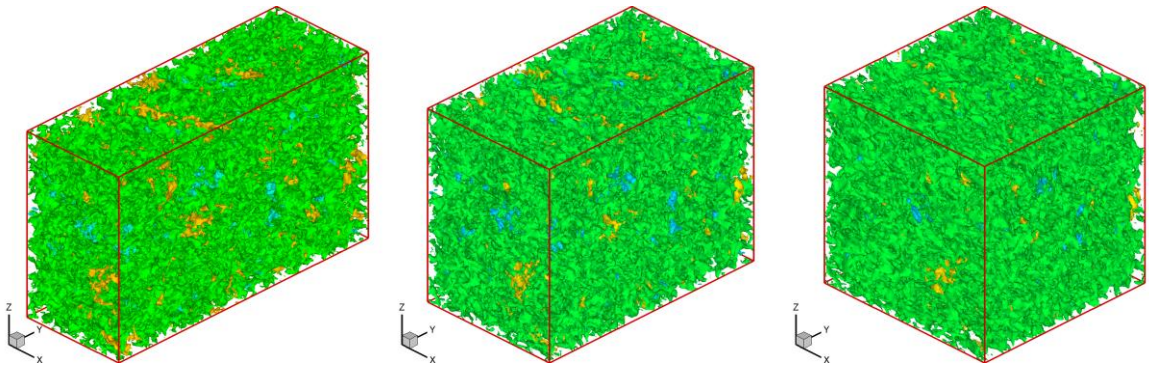

(a) (b) (c)

Figure 4.1 Domain evolution during straining. (a) Domain at time 12.0s before straining begins. (b) Domain at $ST = 0.25$, halfway through the straining process. (c) Final cubic domain after straining is complete (at $ST = 0.5$).

4.3 Results

4.3.1 Initial Conditions

A set of 3 different initial conditions were used to investigate the effects of non-dimensional strain rate on the return process. Values for mean strain rate were chosen but different initial conditions dictate slightly different initial (at start of strain, t = 12) k_0 and ε_0. As a result Sk_0/ε_0 vary slightly from between IC1, IC2 and IC3. Approximate values for the initial Sk_0/ε_0 (at time = 12) are ($Sk_0/\varepsilon_0 \approx 0.346$, 0.865, 1.73 and 3.46). The largest dimensionless strain rate will be shown to approximate the theory of RDT well. The different initial conditions are generated by having a different random placement for the stirring boxes, and by shaking in different random directions (though at the same amplitude). Table 4.1 describes the properties of the three different initial conditions (at time = 12). In total there are 12 simulations involving 4 strain rates and 3 initial conditions, all at roughly the same initial turbulent Reynolds number.

	k_0	ε_0	Re_0	$Re_{\lambda 0}$	$T_0 = k_0/\varepsilon_0$	$L_0 = k_0^{3/2}/\varepsilon_0$	$S\,k_0/\varepsilon_0$	L_η	$L_\eta/\Delta X$
IC1	0.848	0.151	477.466	56.419	5.628	5.184	Low = 0.352 Med-Low = 0.879 Med-High = 1.759 High = 3.518	0.051	0.541
IC2	0.700	0.126	387.370	50.818	5.536	4.631	Low = 0.346 Med-Low = 0.865 Med-High = 1.730 High = 3.460	0.053	0.566
IC3	0.534	0.099	287.880	43.809	5.396	3.941	Low = 0.337 Med-Low = 0.843 Med-High = 1.686 High = 3.372	0.056	0.602

Table 4.1 Initial conditions for the three test cases at a time = 12 seconds (when straining begins).

Table 4.1 shows the initial kinetic energy k_0, dissipation ε_0 and turbulent Reynolds number $Re_0 = {k_0}^2/\nu\varepsilon_0$. It also shows the Taylor micro-scale Reynolds number $Re_{\lambda 0} = (\frac{20}{3}Re_0)^{1/2}$, large-eddy turnover time $T_0 = k_0/\varepsilon_0$, large-eddy length scale $L_0 = {k_0}^{3/2}/\varepsilon_0$, and the Kolmogorov length scale, $L_\eta = \nu^{3/4}/\varepsilon_0^{1/4}$. A grid spacing ΔX that is twice the Kolmogorov length scale or smaller, is considered by most DNS practitioners to be more than sufficient for resolving small scales.

4.3.2 Time Development

The behavior of the turbulent Reynolds number and the large-eddy length scale are shown as a function of time in figure 4.2. This figure shows the behavior for three different initial conditions at the moderate strain rate (Sk_0/ε_0 = 1.76, 1.73 and 1.69). Other strain-rate cases behave similarly. Note that the length-scales (increasing set of blue lines) grow rapidly during the straining process (time 12 to 13.6) and the Reynolds number (decreasing set of green lines) also grows slightly during the straining as energy is added to the turbulence via the mean flow gradients. At a time of roughly 100 the

turbulence is becoming box constrained. The IC1 case (solid blue line) exhibits the most abrupt transition to a fixed length-scale limit. In isotropic decaying simulations a length-scale of 10 to 12 is also found as the upper limit possible for the large-eddy length scale [33]. In what follows, results at times greater than 80 will be assumed to be influenced by the domain size of the simulation.

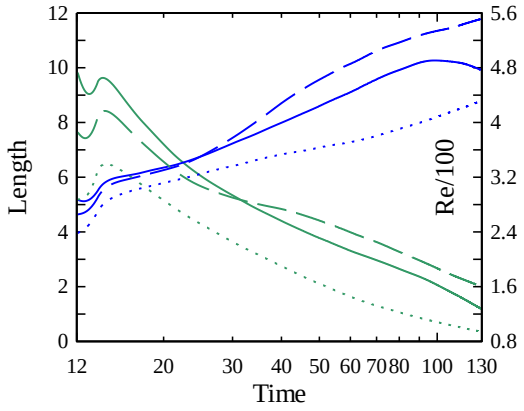

Figure 4.2 Large eddy length scale (blue: left y-axis, increasing curves) and turbulent Reynolds number divided by 100 (green: right y-axis, decreasing curves) as a function of time for $Sk_0/\varepsilon = 1.76$ (IC1), 1.73 (IC2) and 1.69 (IC3). IC1 is solid, IC2 is dashed, and IC3 is dotted line.

The Reynolds stresses for $Sk_0/\varepsilon_0 = 1.76$ and IC2 are shown in figure 4.3 as they evolve in time. Again this case is indicative of the other strain rates and initial conditions. The Reynolds stresses decay with time, with an increase in R_{22} during the straining period and a more rapid decrease in R_{11}. In theory the off-diagonal components of the Reynolds stress tensor should be zero for this flow so the off-diagonal components are not shown here.

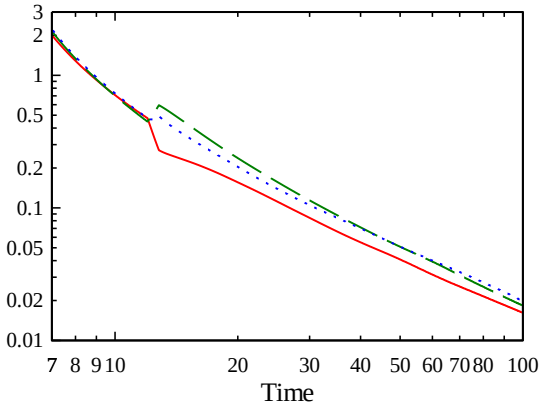

Figure 4.3 Reynolds stresses for IC2 (with $Sk_0/\varepsilon = 1.76$) as a function of time. R_{11} solid red, R_{22} dashed green, and R_{33} dotted blue.

In this work, the dimensionless Reynolds stress anisotropy tensor is given by the expression

$$b_{ij} = \frac{\langle u_i u_j \rangle}{2k} - \frac{1}{3}\delta_{ij} \tag{4.1}$$

This quantity removes the effect of the strong decay that dominates figure 4.3, and allows one to focus on the deviations of the Reynolds stresses from the isotropic case. Figure 4.4 shows the anisotropy tensor corresponding to the same case as figure 4.3. For statistical reasons the off-diagonal components of the anisotropy tensor are not zero. They are shown here (as lines without symbols) to give an indication of the statistical variability present in the results. A dimensionless anisotropy below 0.05 is therefore essentially statistically equivalent to zero in our results. Figure 4.4 confirms the theoretically expected behavior of turbulence subjected to plane strain. For extension in the x-direction the b_{11} component of the tensor (red squares) decreases and becomes negative. The turbulence fluctuations in the x-direction are suppressed. Similarly, compression in the y-direction causes the b_{22} component of the anisotropy tensor (green

diamonds) to increase. Fluctuations are amplified in the compression direction. The z-direction (blue triangles) is only indirectly affected by the strain. The turbulent fluctuations increase slightly in this direction as the energy reorients due to mixing from the y-direction. Figure 4.4 also shows the RDT prediction (which assumes very large dimensionless strain) for this case (solid, black lines) for the time 12 to 12.8. The DNS agreement with the RDT prediction is very good for this highest strain-rate case (the RDT lines lie right on top of the DNS data).

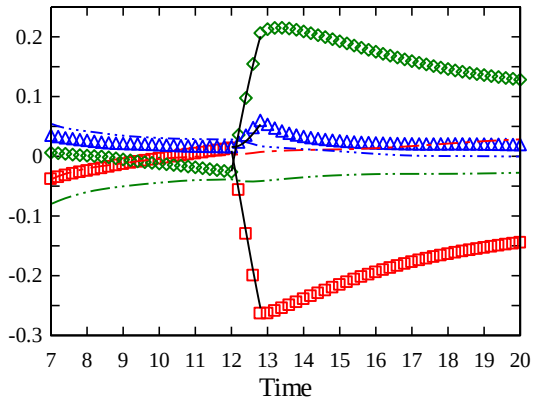

Figure 4.4 Anisotropy tensor, b_{ij} resulting from IC2 subjected to $Sk_0/\varepsilon_0 = 3.46$. Strain runs from t = 12 to t = 12.8. b_{11} red squares, b_{22} green diamonds, b_{33} blue triangles. b_{12} (red, dash-dot), b_{23} (green, dash-dot-dot), b_{13} (blue, dash-dot-dot-dot). RDT predictions are shown (black solid lines) from t = 12 to t = 12.8. There are 50 timesteps between each symbol on the figure.

4.3.3 Strain Rate

The influence of the strain rate on the anisotropy tensor is shown in figure 4.5. This shows four different strain rates applied to the same initial condition (IC2). Remember that the total strain is a constant for these cases (ST =0.5).

To first order the curves are very similar after the straining is completed. This confirms that the total strain and not the strain rate is the critical factor governing how much anisotropy is generated in the turbulence. Another important observation that we

will return to later is the fact that immediately after the strain is removed, the b_{11} and b_{33} components begin to return-to-isotropy, but the large b_{22} component (green) goes *away* from isotropy for some time (1-2 seconds) before finally beginning to decrease. This affect has been noticed in some experiments previously [84] and is also discussed in [26] [28]. We will refer to this period after the strain is removed, but before all components begin to reduce their isotropy, as the ***recovery*** period. It is hypothesized in this work that

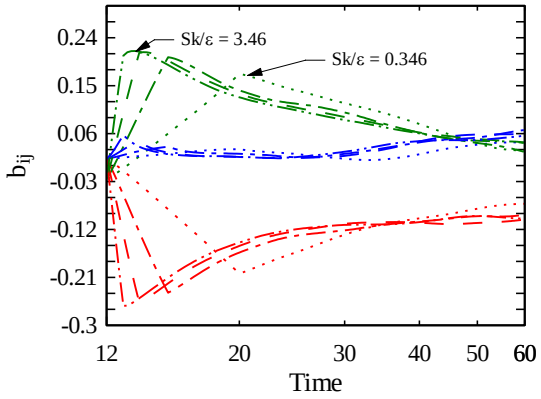

Figure 4.5 (a) Diagonal comp. of anisotropy tensor during strain and decay. Red, lower curves, b_{11}; green, upper curves, b_{22}; blue, central curves b_{33}. Sk_0/ε_0 = 0.346, 0.865, 1.73 and 3.46 for IC2.

in this recovery period, the structure of the turbulence (the two-point correlation lengths) are returning to isotropy faster than the velocity fluctuations are returning. Once the structure (two-point lengths) rapidly recover their isotropic values the more classic mixing of eddies and return-to-isotropy of the velocity fluctuations takes over which we refer to as ***return***.

At very long times, the anisotropy curves do not appear to asymptote to zero. They seem to asymptote to a fixed (non-zero) value. This could be a statistical effect, caused by the very largest eddies (the only ones left after very long times) not having enough statistical sample in the finite simulation domain. Experiments show similar results [8] [78].

Figure 4.6 shows the effect of having different initial conditions and roughly the same strain rate (Sk_0/ε_0 = 3.52 for IC1, Sk_0/ε_0 = 3.46 for IC2, Sk_0/ε_0 = 3.37 for IC3). This figure confirms that the trends described above (particularly the recovery region) are general and not a result of one particular initial condition.

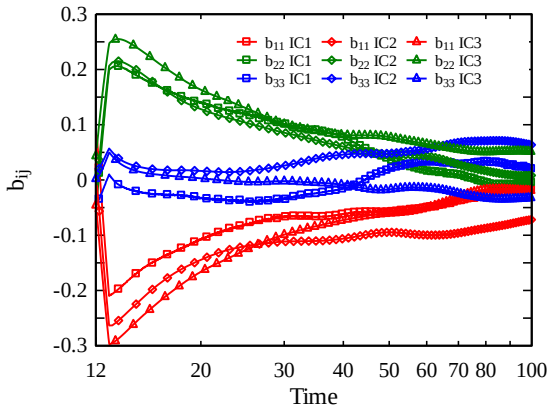

Figure 4.6 Effect of initial conditions IC1, IC2 and IC3 at Sk_0/ε_0 = 3.46. This shows the statistical variation due to different realizations. Statistical anisotropy variation on the order of 0.05 is common.

4.3.4 Scaling

Two different scalings of the time axis are shown in figure 4.7. The first scaling shown in figure 4.7(a) uses a dimensionless timescale based on the strain rate, t* = S(t-12). Under this scaling all the curves travel along the same lines during the straining process. The only difference is that the lower strain rates progress less far along those lines. Only the very lowest strain rate (Sk_0/ε_0 = 0.35) shows a noticeable difference. For this low strain rate, the return-to-isotropy mechanism is strong enough to slow the straining trajectory as it moves away from isotropy.

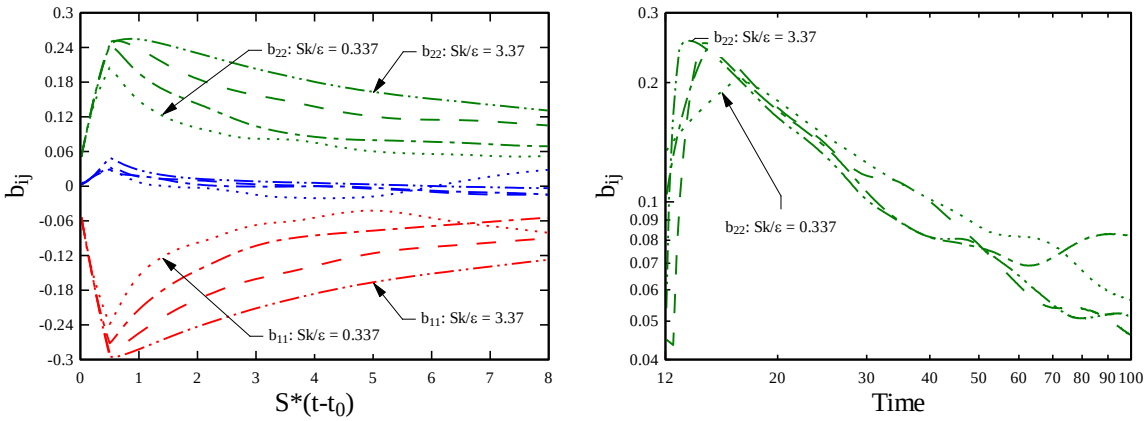

(a) (b)

Figure 4.7 Component of anisotropy tensor during strain and recovery of IC3 subjected to different strain rates. (a) b_{11}, b_{22}, and b_{33} of the anisotropy tensor with time axis scaled. (b) time axis translated.

To obtain a collapse of the curves after the strain, a different scaling must used. The scaling used in figure 4.7(b) translates each curve to the left (in time) until its peak value (at the end of the strain) lies on the highest strain curve. After matching the initial anisotropy level to the highest strain curve, the subsequent evolution of the anisotropy behaves very similarly (the curves lie on top of each other). The linear behavior on a log-log plot indicates a power law decay.

4.3.5 Invariant Map

The anisotropy invariant plot [85] is a common way to look at the return-to-isotropy problem. The anisotropy tensor has zero trace, so one can plot the state of the turbulence as a function of the other two invariants $II = -(1/2)b_{ij}b_{ji}$, and

$III = (1/3)\, b_{ij}b_{jk}b_{ki}$.

Figure 4.8 shows the variation of this turbulence state as a function of time for all three initial conditions and two different strain rates. The turbulence starts close to the origin (isotropy) at time 12. The solid red lines show the evolution as the turbulence is strained and moves away from isotropy. When the strain is removed on the high strain

case, figure 4.8(a), the state moves to the right on the invariant map. This is the recovery period and does not represent a significant return-to-isotropy. After some time the recovery (motion to the right) stops, and the state moves downward towards the isotropic state. At very long times, the trajectory wanders about near zero but no longer continues to approach it. We believe this is a result of the statistical sensitivity and domain constraint at large times. The three different initial conditions have somewhat different trajectories on the invariant map, but these general characteristics remain true for all of them.

The low strain case, figure 4.8(b), has the same general structure of strain (solid) line moving away from isotropy, and no strain (symbols) moving back towards isotropy. However, for the low strain case, return is almost back along the upward straining trajectory. There is far less recovery, or movement of the trajectory to the right. It is hypothesized that when the strain is weaker the structure of the turbulence (two-point correlation lengths) can remain more isotropic even as the strain proceeds, so that the following recovery (to isotropic structure) is much weaker on removal of the strain.

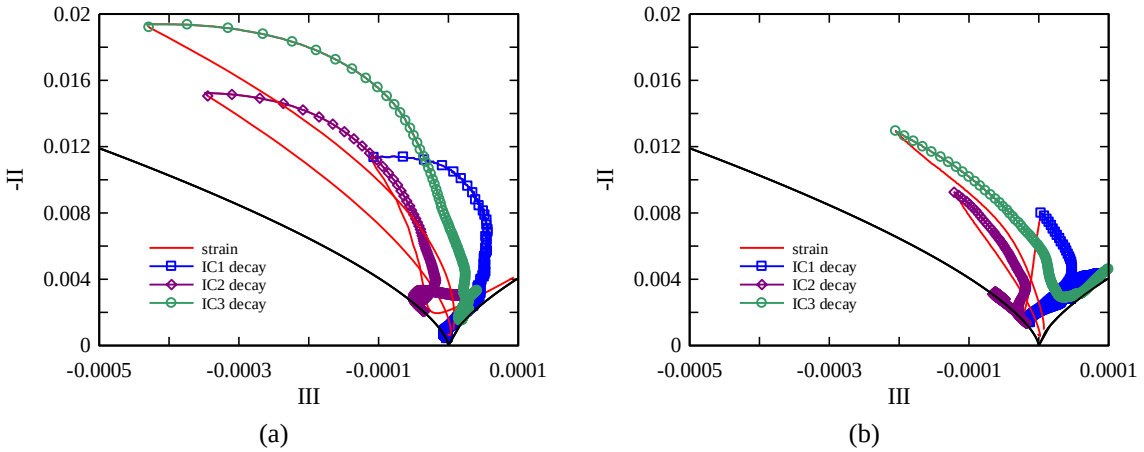

Figure 4.8 Invariant plots of Reynolds-stress anisotropy: (a) IC1: Sk_0/ε_0 = 3.52, IC2: Sk_0/ε_0 = 3.46, IC3: Sk_0/ε_0 = 3.37 (b) IC1: Sk_0/ε_0 = .352, IC2: Sk_0/ε_0 = .346, IC3: Sk_0/ε_0 = .337. The lowest black curves bound the realm or realizability. Solid red lines show the trajectory during the straining process and lines with symbols show the anisotropic decay trajectories.

On this invariant map the classic linear return-to-isotropy model of Rotta [65] would be trajectories that only move downwards, never to the right. Those trajectories never overlap. More complicated nonlinear return-to-isotropy models, such as that of Sarkar and Speziale [18] do show trajectories that move to the right. However, those trajectories can still never cross each other. In figure 4.8(a) there are a large number of trajectory crossings (for the different initial conditions). Trajectory crossing confirms the hypothesis that the time evolution of the anisotropy depends on more than just the anisotropy state itself.

4.3.6 Higher Total Strain

Figure 4.9 shows the effects of doubling the total strain for IC3 subjected to an initial strain-rate of Sk_0/ε_0 = 0.337, 0.843 and 1.686. Both the original strain of ST = 0.5 and doubled strain of ST = 1.0 are shown on each figure.

It can be seen that increasing the strain time increases the amount of anisotropy produced. In addition, it appears that the recovery slope depends on the strain-rate, and

not the total strain. In fact, the low strain case, figure 4.9(a), appears to be recovering (moving to the right) even as the turbulence is strained. The faster the strain-rate, the smaller the strain time and the less recovery can happen during the straining process, and the more it happens after the strain is removed.

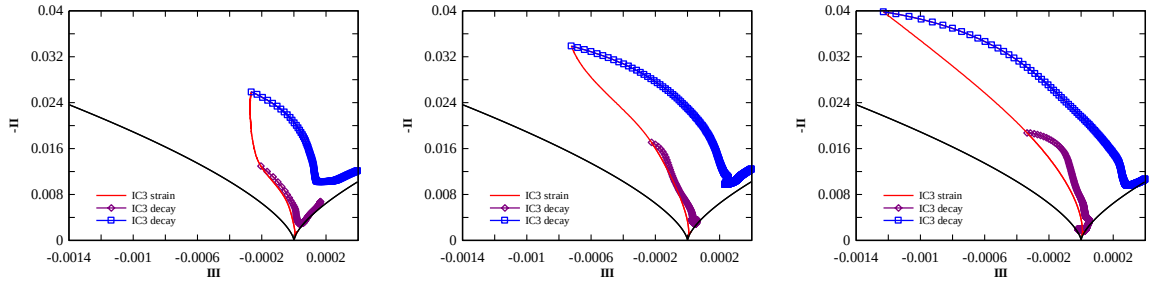

(a) (b) (c)

Figure 4.9 Effect of doubling the strain time on IC3 for: Sk_0/ε_0 = (a) 0.337, (b) 0.843, (c) 1.686

Note that all the doubly strained curves (upper blue curves with squares) tend to move away from isotropy at very long times. This is probably because the mesh is no longer uniform at the end of the doubly strained simulation cases. The mesh is, in fact, the reverse of the initial condition mesh before the straining. Differences in resolution in the three mesh directions may then cause slightly different decay rates in the three directions moving the turbulence away from isotropy at very long times. The very long time behavior of these doubly strained cases is therefore less accurate.

4.3.7 Decay Rate

The decay rate is an extremely sensitive indicator of whether the turbulence is decaying like isotropic turbulence. The velocity derivative skewness, which is a more commonly used indicator, will stay at the classic value of -0.5 for all sorts of conditions where the decay rate shows a strong variation from the theoretical values. Figure 4.10 shows the decay rate n as a function of time for three different initial conditions and two

different strain rates. The decay rate is given by $n^{-1} = \frac{d(K/\varepsilon)}{dt}$. It represents the power at which the kinetic energy decays, $(t) = K_0(t - t_0)^{-n}$. The numerical calculation of this quantity requires small time increments for an accurate representation of the derivative [33]. Before the strain is applied at time 12 the turbulence usually approaches the theoretically expected high Reynolds number value of 6/5 determined by Saffman [86]. Reference [33] shows this initial development behavior before this time but this work focuses on the strain and subsequent recovery. After the strain, the decay rate appears to approach the low Reynolds number Saffman theoretical value of 3/2. Then after more time, the higher Reynolds number cases (IC1 and IC2, see figure 4.10) drop back towards the high Re decay rate , before finally moving towards the domain constrained decay exponent value of 2 (see Stalp *et al*. [87] and Touil *et al*. [88]) at very long times (after about 100 seconds). The highest Re case (IC2, at time 40) drops all the way to the high Re value. The medium Re case (IC1) only drops slightly, but does not go to 6/5. In any case, Reference [33] looked at Re effects for decaying turbulence in more detail and showed that the decay rate transition from 6/5 to 3/2 is not solely related to the Reynolds number.

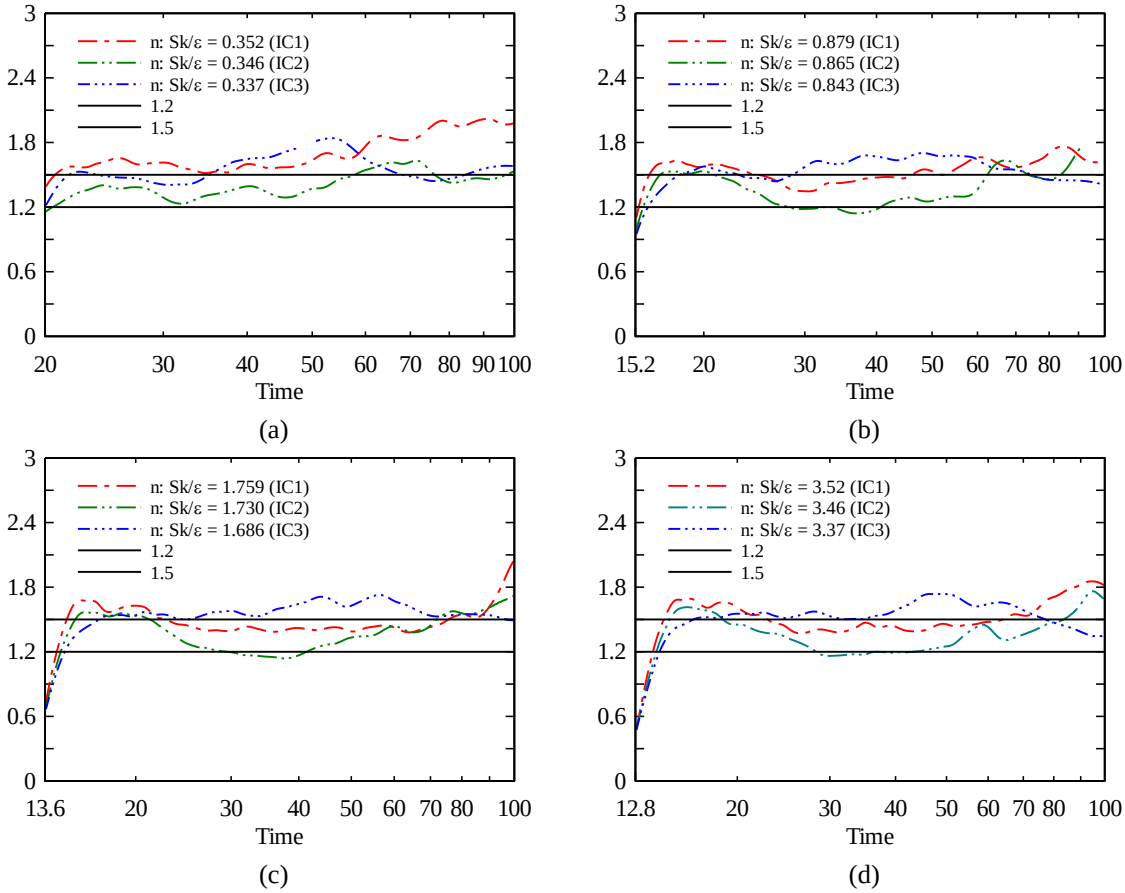

Figure 4.10 Decay exponent, n, resulting from initial conditions IC1, IC2 and IC3 subjected to plane strain. $Sk_0/\varepsilon_0 \approx$ (a) 0.346, (b) 0.865, (c) 1.730, (d) 3.46. Origin of x-axis represents the end of strain for each case.

4.4 Modeling

4.4.1 Anisotropy Based Models

Traditional return-to-isotropy models such as the linear Rotta [65], or the more general non-linear models (such as Sankar and Speziale [18]), attempt to characterize the return-to-isotropy using only the anisotropy tensor itself. A typical model for the slow part of the pressure-velocity gradient correlation takes the form:

$$\frac{db_{ij}}{dt} = (1 - C_1)\frac{b_{ij}}{T} + C_1^n \frac{\left(b_{ij}^2 - \frac{1}{3}b_{kk}^2\delta_{ij}\right)}{T} \tag{4.2}$$

Note that C_1 should be greater than 1 or this model does not cause return-to-isotropy.

In the case of plane strain the anisotropy tensor has two independent quantities because the off diagonal components are zero and the diagonal components sum to zero. It is therefore possible to determine the two constants C_1 and C_1^n from the two independent anisotropy components $b_{11}(t)$ and $b_{22}(t)$, and their evolution in time (see Durbin and Reif [63] for more details). The values for these constants are shown in figure 4.11 for the highest strain rate and three different initial conditions.

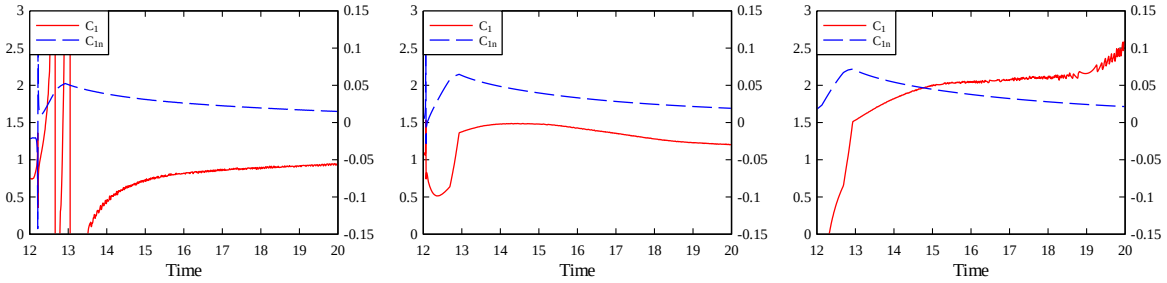

Figure 4.11 Linear return-to-isotropy constant C_1 (solid red curve, left axis) and the non-linear constant C_n (dashed blue curve, right axis) as a function of varying ICs (a) IC1 (Sk_0/ε_0 = 3.52), (b) IC2 (Sk_0/ε_0 = 3.46), (c) IC3 (Sk_0/ε_0 = 3.37).

The analysis only applies after the strain stops (12.8 seconds). Even for the same strain rate there is significant variation of these constants as a function of time and between different initial conditions. For the first initial condition IC1, figure 4.11(a), the constant C_1 is roughly a value of 1, which means the linear return part of the model is zero and the return is largely non-linear. The non-linear constant takes a value of roughly 0.03 for these cases but changes significantly with time. For IC3, figure 4.11(c), the value of C_1 is roughly a value of 2.

Figure 4.12 shows the return constants for the IC3 case after a variety of different strain rates. The linear constant tends to be a bit larger (1.5) for this IC. The value of the constants during the straining process (before the jump in the linear constant) are not relevant. Both figures 4.11 and 4.12 are suggesting that modeling the anisotropic decay process with this type of model is quite probably not feasible in practice.

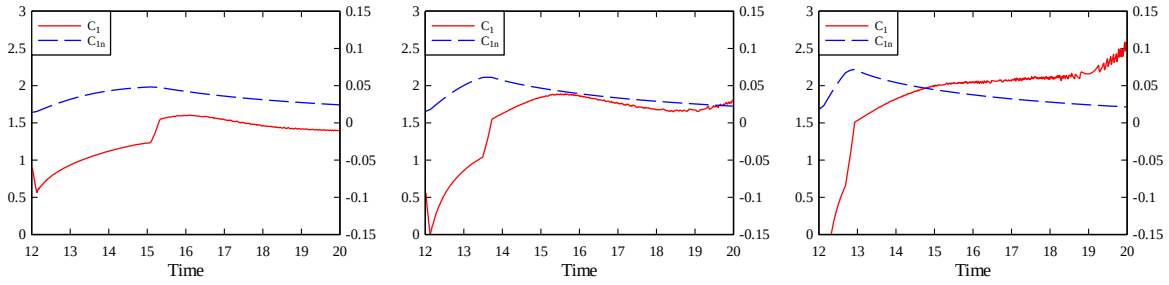

Figure 4.12 Linear return-to-isotropy constant C_1 (solid red curve, left axis) and the non-linear constant C_n (dashed blue curve, right axis) as a function of varying strain on IC3 (a) Sk_0/ε_0 = .843, (b) Sk_0/ε_0 = 1.69, (c) Sk_0/ε_0 = 3.37.

It is possible, that the constants in the models above are actually a function of the anisotropy invariants (*II* and *III*) or other dimensionless variables such as the Re. References [9] and [10] contain examples of models where such functions have been hypothesized. Note, that no matter how complex the functional dependence of the model constants, a return-to-isotropy model that only depends on information contained in the anisotropy tensor produces unique trajectories on the invariant map that never cross (one state can never produce two different evolution paths for these models). The crossings in figure 4.8 suggest that additional information must be used in the return-to-isotropy model. The Reynolds numbers in these test cases does not vary significantly between initial conditions, or the different strain rate tests, so it unlikely (in these simulations) to be the critical missing information. The next section considers the performance of a model which can account for eddy structure.

4.4.2 Oriented-Eddy Collision Model

The oriented eddy collision (OEC) model is discussed extensively in [1]. This model looks like a collection of Reynolds stress transport equations coupled with a set of transport equations for the inverse two-point correlation lengths. The information contained in the OEC model can be used to approximate the two-point correlation (not just its peak value which is the Reynolds stresses). In the OEC model the two-point correlation is approximated by

$$Q_{ij}(\boldsymbol{x},\boldsymbol{r}) = \sum \hat{R}_{ij}(\boldsymbol{x},t) f(|\boldsymbol{q}(\boldsymbol{x},t)\cdot\boldsymbol{r}|) \tag{4.3}$$

Where $\hat{R}_{ij}(\boldsymbol{x},t)$ and $\boldsymbol{q}(\boldsymbol{x},t)$ are determined by the model PDEs and the function f is usually chosen to be a decaying exponential. The OEC model uses a classic linear return-to-isotropy model for the velocity fluctuations, and also the simplest possible linear return-to-isotropy model for the inverse correlation lengths, $\boldsymbol{q}$. However, the time scale for the $\boldsymbol{q}-$ recovery is faster than that for the velocity-return.

The ability of the OEC model to predict the plane strain return is shown in figure 4.12. This figure shows the Reynolds stresses for IC1 subjected to 4 different strain rates. The OEC model is exact in the RDT limit, so the ability to c**a**pture the effect of straining which is normally quite difficult for turbulence models is not a problem for this model. The subsequent anisotropic decay (return-to-isotropy) is not exact for the OEC model. But the model uses the same information used to exactly predict the strain process, to also model the recovery process. The agreement over all 4 test cases (with the same model constants) is encouraging.

A more sensitive test of the OEC model is to plot the results on the anisotropy invariant map. This is shown in figure 4.13. The model produces the correct qualitative features. However, it tends to overshoot the recovery and move too far to the right on the invariant map. Note that this model can produce trajectory crossing like the DNS data demonstrates. Also note that this invariant plot uses cubes of the anisotropy for the x-axis as so small differences are exaggerated on this type of plot.

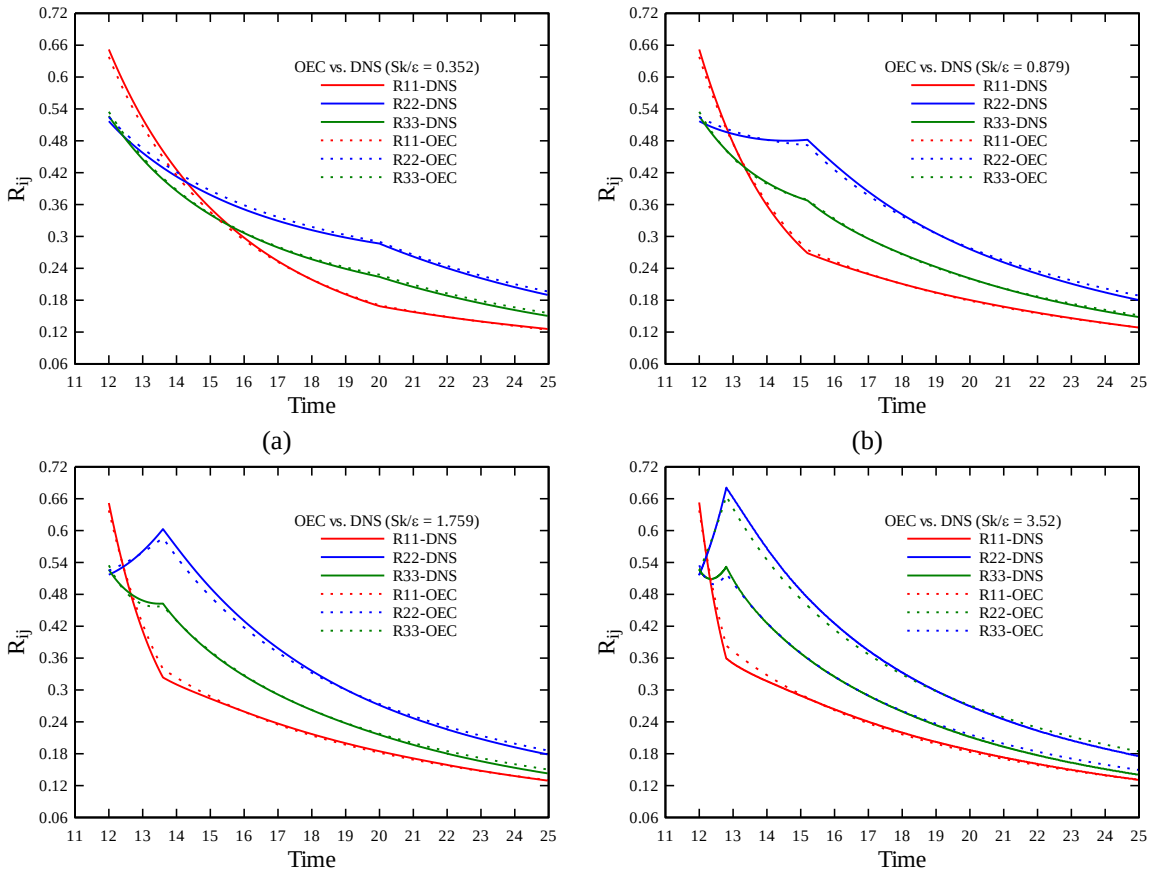

Figure 4.13 Reynolds stresses for IC1 with DNS data (solid lines) and the OEC model (C_R 0.5, C_L 0.67) predictions (dashed lines), for Sk_0/ε_0= (a) 0.352, (b) 0.879, (c) 1.759, (d) 3.52

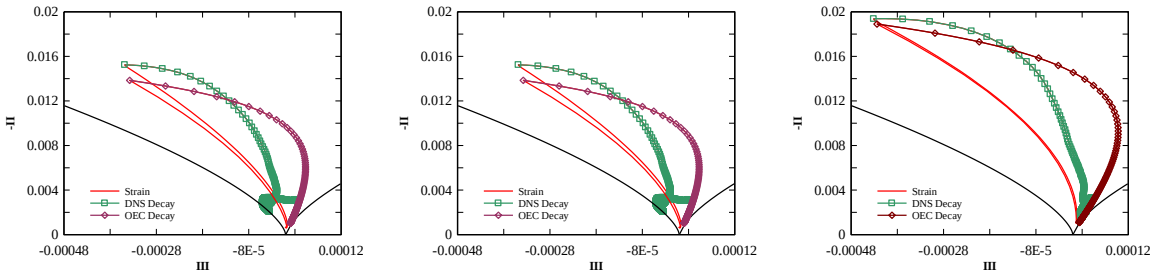

(a) (b) (c)

Figure 4.14 DNS and OEC model predictions for the three different initial conditions at the highest strain rate. (a) IC1, $Sk_0/\varepsilon_0 = 3.52$, (b) IC2, $Sk_0/\varepsilon_0 = 3.46$, (c) IC3, $Sk_0/\varepsilon_0 = 3.37$. The DNS is squares and the model is the diamonds.

4.5 Discussion

The simulations presented in this work have a 512^3 mesh resolution in order to try to capture the large scales well. Results suggest that the large-eddy length scale should be less than ¼ of the domain size to prevent the turbulence from becoming domain constrained. The large scales are known from theory to govern the behavior of isotropic decay. They also appear to strongly influence the behavior of anisotropic turbulence. In particular, at long times we do not see a return-to-isotropy, but a return of the small scales to anisotropy and fixed background level of the large scale anisotropy. Comte-Bellot and Corrsin [36] make the same observations in their experiments as do Kang *et al.* [89]. George [90] provides a possible theoretical argument for this behavior.

The initial conditions for the presented simulations were generated by moderate size cubes in a way that all large scales were formed by the turbulence process itself. The very largest scales of the turbulence (which govern the decay behavior) are much larger than the initial mixing cube size. There is very little human input to the simulation that influences the large scale turbulence. The very largest scales result from the Navier-Stokes equations and their interaction with a random arrangement of small cubes.

Because the large scales are much smaller than the domain size in these simulations, the turbulent Reynolds numbers are not large. Still, they are comparable to some experimental Reynolds numbers, and they appear to be high enough (at least for IC2) to produce the isotropic decay rate (n=6/5) predicted by Saffman for high Re turbulent decay both before and well after the straining process. It was found that after straining, the turbulent decay rate tends to be larger than the theoretical value that one would expect for isotropic decaying turbulence (during the recovery phase). At longer times after the strain, the decay rate returns to its classic theoretically expected value even though the turbulence is not yet fully isotropic (during the return phase).

An important observation of this paper is the confirmation that the return-to-isotropy occurs in two stages, a ***recovery*** stage immediately after the strain is removed in which some of the anisotropy components can still be increasing (and the decay rate differs from its isotropic value), and after some time the more classic ***return*** stage where the velocity fluctuation anisotropy tends to zero (and the classic isotropic decay rates are applicable). We hypothesize that the recovery stage is the turbulence structure (two-point correlation lengths) returning to isotropy at a faster rate than the velocity fluctuations return (which is the classic return stage). The presence of crossing trajectories on the invariant map is a critical observation because it demonstrates unequivocally that the evolution of anisotropic turbulence cannot be captured by the information in the anisotropy tensor alone.

Classic models for return-to-isotropy process have been stymied because they did not account for the presence of the recovery stage of anisotropic turbulent decay. It was

shown that even for the same flow conditions, that different initial conditions produced quite different values for the constants in the classic non-linear return-to-isotropy models.

Like the OEC model, the models of Kassinos, Reynolds and coworkers [27] [28] can also predict the two stages of anisotropic decay, recovery and return. However, the underlying models are related but not the same because of the difference in philosophy about what extra information is being included in the model (one-point correlations of derivatives, versus direct two-point information). Both modeling results of Kassinos, Reynolds and the current DNS work both indicate that the recovery stage of anisotropic decay requires knowledge of and some representation of the turbulent structure.

This work only examines one type of anisotropic turbulence (plane strain), but it is encouraging that the OEC model gives fairly reasonably predictions for all the different initial conditions and strain rates with a single set of constants. Simulation and modeling of other canonical turbulent flows are ongoing.

CHAPTER 5

AXI-SYMMETRIC CONTRACTION AND EXPANSION

5.1 Overview

The effect of axisymmetric contraction (AXC) and expansion (AXE) on isotropic turbulence and its subsequent decay are evaluated by way of direct numerical simulation (DNS). Small, moderate and large rates of contraction/and expansion are evaluated at moderate Reynolds number using two different sets of initial isotropic turbulence (initial conditions). The initial turbulence is generated via mechanical mixing so that the large scale turbulence develops naturally. Turbulence Reynolds number, length scales, decay rates, and anisotropy are investigated for the range of the simulations, with the goal of quantifying how anisotropic decay behaves during return-to-isotropy.

5.2 Introduction

Development of new or improved turbulence models requires a fundamental understanding of the turbulence itself. In particular the behavior of turbulence under controlled conditions such as the influence of a prescribed mean flow. Two such mean flow conditions are axisymmetric contraction (AXC) and expansion (AXE). In axisymmetric contraction two of the components of mean flow contract toward the center of the domain while the third component is allowed to expand to compensate and maintain the condition of incompressibility. Therefore, in this work, the mean flow AXC

is given by $u = 2Sx,\ v = -Sy,\ w = -Sz.$ Conversely AXE is given by $u = -2Sx,$ $v = Sy,\ w = Sz,$ where in both cases S is a constant. This type of flow can be found in applications involving contracting and expanding ducts as well as many other situations. Exposing isotropic turbulence to axisymmetric contraction or expansion is one of the canonical cases used to study the effects of mean flow deformation on isotropic turbulence. As pointed out by Pope [59], relatively low axisymmetric expansion (low S) can be investigated experimentally, while the case of rapid (RDT) axisymmetric expansion cannot be physically determined due to flow separation. Axisymmetric contraction is more forgiving in that it can be studied experimentally across a larger range of S. Uberoi [91] investigated experimentally, with a 4:1 contraction duct, the effects of axisymmetric contraction finding that the larger components of mean-square turbulent velocities $\langle v^2 \rangle$ and $\langle w^2 \rangle$ lose more energy due to dissipation than by the transfer to the smaller component $\langle u^2 \rangle$. However $\langle u^2 \rangle$ is receiving enough energy by transfer to compensate for its decay and in fact can be seen to increase. Mills and Corrsin [92] studied the effects of axisymmetric contraction on variable density turbulence as generated by a warm grid. While Comte-Bellot and Corrsin [93] Conducted experiments on axisymmetric contraction over a range of Reynolds numbers. Le Penven, Gence and Comte-Bellot [8] experiments using axisymmetric contraction and expansion indicated that starting from two different initial conditions, AXC and AXE, required two different C_r values for Rotta's [65] linear return model if one wanted the model to match the data. Lumley and Newman [94] and Choi and Lumley [11] point out the lack of information on the return-to-isotropy of homogeneous turbulence. Specifically by what mechanism and at what rate does return-to-isotropy take place. They investigate axisymmetric

contraction and expansion using grid generated turbulence and determine that return-to-isotropy does not follow Rotta's linear model. In addition Choi and Lumley parameterize the return rates of axisymmetric contraction and expansion relative to the overall decay of the turbulent kinetic energy:

$$\rho^* = \frac{k/(dk/dt)}{II/(dII/dt)} \tag{5.1}$$

Where k is the turbulent kinetic energy and II is the second invariant of the normalized anisotropy tensor where the second and third anisotropy tensor are given by

$$II = 3\eta^2 = -(1/2)b_{ij}b_{ji} \tag{5.2}$$

$$III = 2\xi^3 = (1/3)\, b_{ij}b_{jk}b_{ki} \tag{5.3}$$

finding that ρ^* takes on a range of values depending on the distribution of the anisotropy. The character of anisotropy can be described using these invariants as they provide a convenient way to visualize the return-to-isotropy process through the use of an anisotropy map where the anisotropy map displays the trajectory (the path from and to isotropy) as fluid is strained and subsequently allowed to return-to-isotropy. One such map developed by Lumley and commonly referred to as the Lumley triangle, plots -*II* and *III* invariants of the normalized anisotropy tensor. Figure 5.1 shows the invariant map for reviewing the trajectories and distribution of anisotropy. Turbulent eddies with two large and one small component (-*III*) in the anisotropy tensor can be thought of as having a

"pancake" shape while anisotropy with one large and two small components of anisotropy (+*III*) can be thought of as "cigar" shaped.

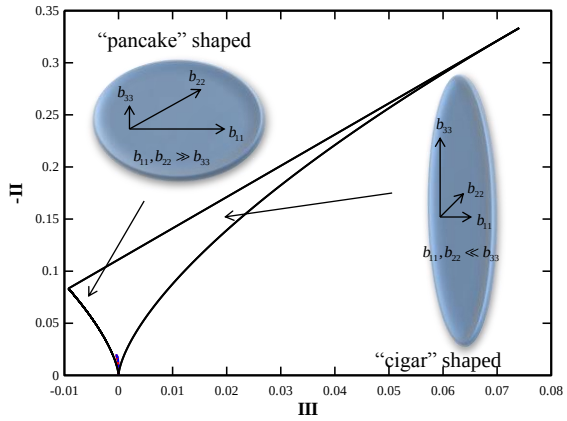

Figure 5.1 The invariant map for reviewing the trajectories and shape of anisotropy. Choi and Lumley found that [ρ^*(*III* < 0, i.e. "pancakes")] > [ρ^* (*III* > 0, i.e. "cigar")].

Lee and Reynolds [81] found that Reynolds stress anisotropy can be seen to increase in the initial stages following removal of strain. Sjogren and Johansson [95] conducted experimental investigation of axisymmetric contraction in wind tunnel finding that the slow pressure-strain has both a Reynolds number dependence as well as a dependence on the degree of anisotropy. Banerjee, Ertunc, Koksoy and Durst [96] evaluate a number of rapid pressure strain rate models and return-to-isotropy models using AXC/AXE data from Ertunc [97] and Lumley [98]. An important element of this research is pointed out by Cambon and Scott [99], that although two flows can have identical $\langle u_i u_j \rangle$ and thus anisotropy tensors [77] the underlying flows can be significantly different and can only be identified by their two point correlation structure $\langle u_i u_j(x+r) \rangle$. It is this point that the current paper hopes to elaborate on and reinforce the idea that two point correlations are necessary for the understanding of the turbulence and thus its modeling.

The discussion of the structure of the turbulence of the single point statistics $\langle u_i u_j \rangle$ should not be confused with the structure described by two point statistics $\langle u_i u_j (x + r) \rangle$ where the single point statistics are a special case of the two point statistics, namely at $r = 0$. Single point statistics give averages of the Reynolds stress tensor components but no indication or evidence in how the velocity fluctuations are related to their neighbors. Consequently many different flow patterns can average to the same value of R_{ij} and thus the same anisotropy. As a result the Reynolds stress or anisotropy tensors don't give enough of a description of the structure of the turbulence.

5.3 Results

5.3.1 Initial Conditions

Simulations were performed for cases of both axisymmetric contraction (AXC) and expansion (AXE), each undergoing three different strain rates (low, medium and high). In addition, in order to investigate the effects of initial conditions, two different initial conditions were used for each simulation case producing a suite of 12 simulations. The initial conditions (at the start of strain, $t_0 = 12s$) are listed in table 5.1. As a result of the slightly different initial values for the turbulence, the dimensionless strain rate, $S\,k_0/\varepsilon_0$, varies slightly between the low, medium, and high strain rate cases. Where S is the characteristic mean strain rate given by the maximum absolute strain rate in each case. The largest dimensionless strain rate cases will be shown to approximate the theory of RDT well during the straining period. The different initial conditions are generated by

having different random placements for the stirring cubes, and by shaking the domain in different random directions (though at the same amplitude).

		k_0	ε_0	Re_0	$Re_{\lambda 0}$	$T_0 = k_0/\varepsilon_0$	$L_0 = k_0^{3/2}/\varepsilon_0$	$S\,k_0/\varepsilon_0$	L_η	$L_\eta/\Delta x$
AXC	IC1	0.706	0.131	380.417	50.360	5.388	4.527	Low = 0.168 Med = 0.842 High = 3.367	0.053	0.561
	IC2	0.719	0.141	365.016	49.330	5.099	4.324	Low = 0.159 Med = 0.797 High = 3.187	0.052	0.550
AXE	IC1	0.770	0.138	430.827	53.593	5.595	4.909	Low = 0.175 Med = 0.874 High = 3.497	0.052	0.554
	IC2	0.838	0.160	440.103	54.167	5.252	4.808	Low = 0.164 Med = 0.821 High = 3.282	0.050	0.534

Table 5.1. Initial conditions for 12 test cases. All values are taken at time t = 12s (the onset of strain)

In addition to the dimensionless strain rate, table 5.1 also contains the initial kinetic energy k_0, dissipation ε_0, initial turbulent Reynolds number $Re_0 = {k_0}^2/\nu\varepsilon_0$, and the initial Taylor micro-scale Reynolds number $Re_{\lambda 0} = \sqrt{(20/3)Re_0}$. This work is similar in initial turbulent Reynolds number and resolution to the well resolved simulations of de Bruyn Kops and Riley [35]. The turbulent Reynolds numbers present in these simulations should be sufficient to capture the fundamental physics. The turbulent Reynolds number is also nearly the same as the turbulent Reynolds numbers in the classic wind tunnel experiments of Comte-Bellot and Corrsin [36].

The initial large-eddy turnover time $T_0 = k_0/\varepsilon_0$, is roughly 5 seconds. The duration of the strain is always less than or roughly equal to this time scale. The initial large-eddy length scale $L_0 = {k_0}^{3/2}/\varepsilon_0$ of roughly 4.8 is 1/10 of the simulation domain. The domain therefore provides considerable resolution of the large eddy scales. A domain size of at least 4 times the large eddy size was found by Perot [33] to be a necessary condition for proper decay in isotropic turbulence. Finally the table also shows

the initial Kolmogorov length scale, $L_\eta = \nu^{3/4}/\varepsilon^{1/4}$. A Kolmogorov length scale that is half the largest mesh spacing Δx or bigger is considered by most DNS practitioners to be more than sufficient for resolving small scales.

5.3.2 Time Development

The behavior of the turbulent Reynolds number and the large-eddy length scale are shown as a function of time in figure 5.2. This figure shows the behavior for two different initial conditions. High strain rate is shown for both AXC (figure 5.2a) and AXE (figure 5.2b), other strain-rate cases behave similarly. Note that the length-scales (increasing set of blue curves) grow more rapidly during the straining process (12.0s to 12.8s). The Reynolds number (decreasing set of greencurves) can also grow slightly during the straining because means expansion or contraction can add energy to the turbulence via the mean flow gradients. Solid lines are IC1 and dashed lines are IC2. The higher strain rate cases often show slightly more variation between the two initial conditions.

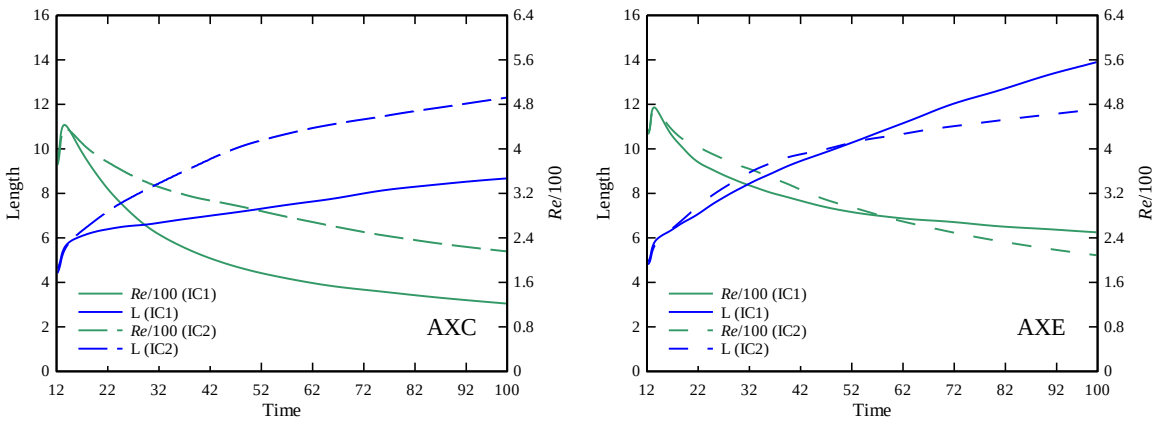

Figure 5.2. Large eddy length scale (blue, increasing curves: left y-axis) and turbulent Reynolds number/100 (green, decreasing curves: right y-axis). (a) AXC and (b) AXE at high strain rate. IC1 is solid lines, IC2 is dashed lines.

For all the cases in figure 5.2 the length scales continue to increase with time. This indicates that the turbulence has not become constrained by the domain size. In isotropic decaying simulations a length-scale of approximately ¼ the domain size (a length = 12 in these simulations) is found as the upper limit possible for the length scale before the domain begins to constrain the turbulence (and affect the decay results). As such, results in figure 5.2 are reaching a time where the periodic domain begins to influence results. This indicates that simulation times greater than 100 may become polluted by the finite domain size.

Reynolds stresses for AXC IC1 and AXE IC2, both subjected to high strain rates, are shown in figure 5.3 as they evolve in time. Again, these cases are indicative of the other strain rates and initial conditions. The Reynolds stresses decay with time overall, but for AXC there is an increase in the R_{22} and R_{33} stresses during the straining period and a more rapid decrease in R_{11}. Similarly, for AXE the opposite affect occurs. The off-diagonal components of the Reynolds stress tensor are small (statistically equal to zero) and so are not relevant to show in this figure. The blue (dotted) and green (dashed) lines would be identical to each other if the initial condition was perfectly axisymmetric. For statistical reasons, the initial conditions in this work are only ever close to axisymmetric.

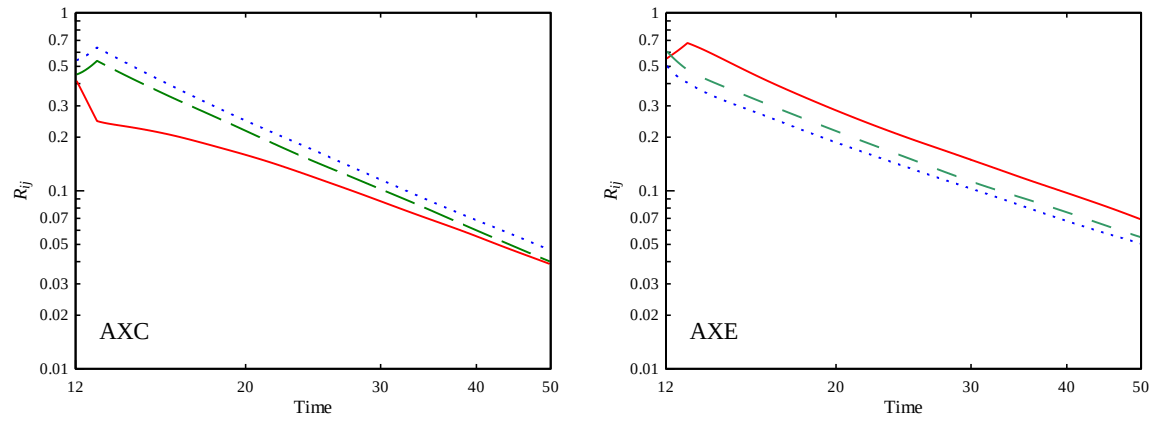

(a) (b)

Figure 5.2. Reynolds stresses for (a) AXC IC1: high strain rate. (b) AXE IC2: high strain rate. R_{11} solid red, R_{22} dashed green, and R_{33} dotted blue.

In this work, the dimensionless Reynolds stress anisotropy tensor is given by the expression:

$$b_{ij} = \frac{R_{ij}}{2k} - \frac{1}{3}\delta_{ij} \tag{5.4}$$

This quantity removes the effect of the strong decay that dominates figure 5.3, and focuses on the deviations of the Reynolds stresses from the isotropic case. Figure 5.4(a) shows the anisotropy tensor corresponding to AXC for initial conditions IC1 while figure 5.4(b) shows the anisotropy tensor corresponding to AXE for initial conditions IC2. Both figure 5.4(a) and 5.4(b) show b_{ij} values as a result of low medium and high strain rates. Other than statistical noise the off-diagonal components of the tensor are zero and not shown. Figure 5.4 confirms the theoretically expected behavior of turbulence subjected to AXC and AXE. During the AXC straining process the b_{22} and b_{33} components of the tensor increase while the b_{11} component decreases. After the straining process, all the anisotropy components tend to decay back towards zero. Again, for perfect axisymmetry

of the initial conditions then the dotted and dashed lines would lie on top of each other. It is clear that the behavior of the two sets of curves is very similar, with the major difference being a shift due to the slightly different initial conditions. As would be expected for AXE the b_{22} and b_{33} components now decrease and become negative, while the b_{11} component increases during the expansion process. In general, regardless of AXC or AXE the tensor components aligned in the direction of contraction increase while those aligned with expansion are suppressed. Figure 5.4(b) shows that at short times after the strain is removed from AXE the b_{11} component continues to increase, whereas for AXC the turbulence anisotropy abruptly decreases as soon as contraction ceases. This behavior of expansion is also seen in the case of plane strain Zusi & Perot [100].

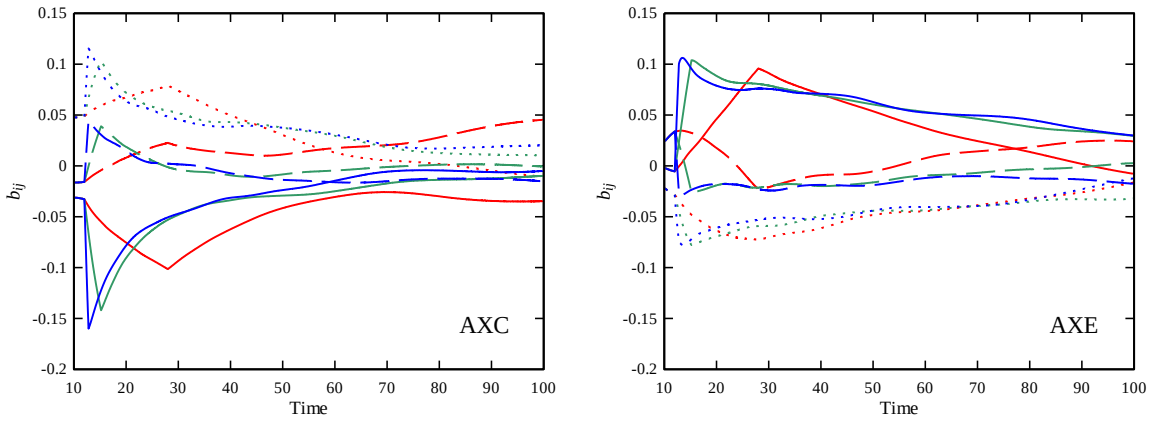

(a) (b)

Figure 5.3. Normalized anisotropy tensor (b_{11} solid lines, b_{22} dashed lines, b_{33} dotted lines) showing the effects of low, med. and high strain rates on (a) AXC IC1, (b) AXE IC2. The straining process occurs from 12.0 until 12.8, 15.2, and 28.0 respectively.

We will refer to this period after the strain is removed, but before all components begin to reduce their isotropy, as the ***recovery*** period. It is hypothesized in this work that in this ***recovery*** period the structure of the turbulence (the two-point correlation lengths) are returning to isotropy faster than the velocity fluctuations are returning. The structures

quickly ***recover*** their isotropic values, while the more classic mixing of velocity fluctuations and return-to-isotropy operates on a slower time scale. Note in figure 5.4(b), that recovery is more pronounced the higher the strain rate. This idea is used in the modeling section, 5.4.

For these simulations a b_{ij} with a magnitude < 0.05 is essentially statistical noise. At long times the various tensor components can be seen to wander within ± 0.05. At very long times, the anisotropy curves do not appear to asymptote to zero. They seem to asymptote to a fixed (non-zero) value. This could be a statistical effect caused by the very largest eddies (the only ones left after very long times) not having enough statistical sample in the finite simulation domain. Experiments show similar results, Le Penven [101], Gence [12] at long times.

5.3.3 Initial Conditions

Figure 5.5 shows the effect of having different initial conditions at the same strain rate. Figure 5.5(a) shows AXC and figure 5.5(b) shows AXE both subjected to the highest strain rate. In both figures solid lines are IC1 and dashed lines are IC2. The highest strain case shows the most variation between initial conditions. Figure 5.5(b) also clearly shows the recovery region immediately following the removal of strain at time 12.8s. This figure suggests that at high strain the recovery process described above is robust and is not a statistical artifact of IC1.

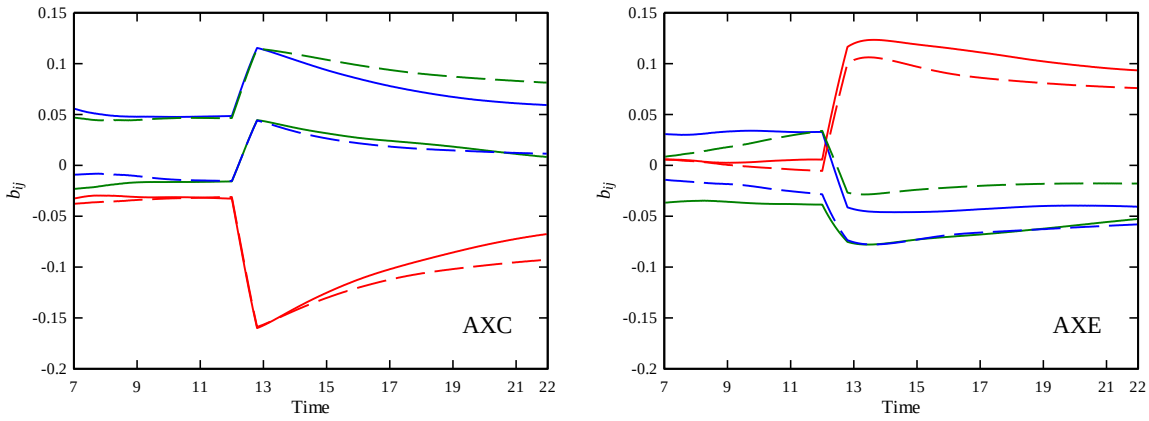

(a) (b)

Figure 5.4. Effects of initial conditions on (a) AXC and (b) AXE. (IC1 solid) (IC2 dashed).

5.3.4 Scaling

Figure 5.6 uses a scaling of the time axis to normalize the results for b_{ij} under the action of strain. This scaling uses a dimensionless timescale based on the strain rate, t* = S(t-12). Where 12 is the time in seconds at which straining begins. Under this scaling all the curves should begin and end the straining process at the same dimensionless time. The black lines on figure 5.6 are the theoretical results from the RDT theory for an infinite strain rate. The highest simulated strain rates (with dimensionless strain rate values of around 3) closely approximate the RDT theory. For AXC, the lower strain rates show a marked deviation from the RDT theory.

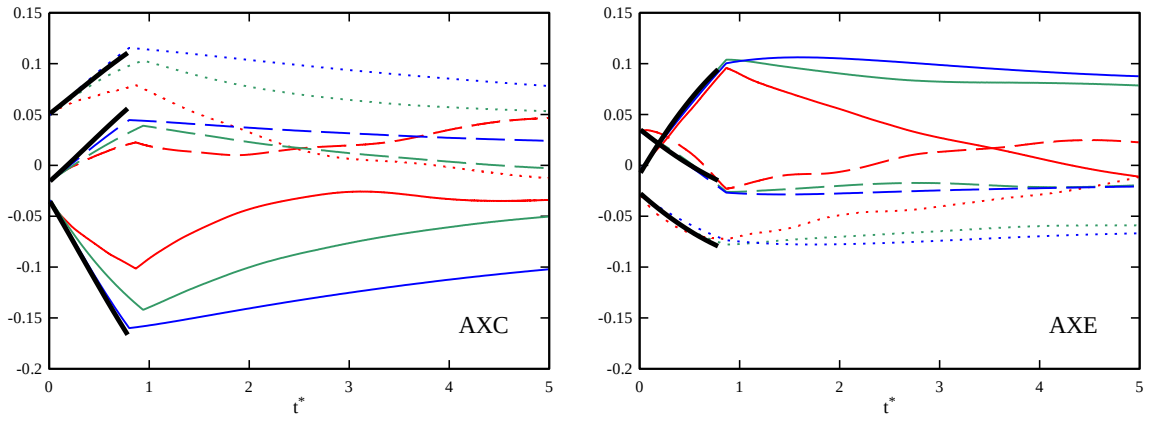

(a) (b)

Figure 5.5. Component of anisotropy tensor during strain and recovery subjected to different strain rates with x-axis scaled by S(t-12). b_{11} (solid), b_{22} (dashed), and b_{33} (dotted). (a) AXC IC1 (b) AXE IC2. Lower strain rates diverge from the RDT predictions (thick black lines) earlier in the straining process.

However, the AXE tends to agree with the RDT solution even at relatively low strain rates. The implication, here is that return-to-isotropy is weaker for turbulence generated by expansion. Experiments, (Gence et al) have also noted this phenomena. We hypothesize in this work that it is not differences in the Reynolds stress anisotropy that cause this effect, but differences in the turbulence structures (specifically two-point correlations) that the two different types of straining create.

A similar scaling of the time axis, for the situation after the strain is removed is more difficult. There is no obvious timescale in this situation. The large eddy timescale $T = k/\varepsilon$ varies linearly with time. Normalizing by it means dividing time by something proportional to time. Normalizing by the initial value at a particular time (say after strain stops) is arbitrary. A similar time normalization dilemma occurs for isotropic decaying turbulence. In figure 5.7 each curve is shifted in time until the peak value of the anisotropy (the value at the end of the strain) lies on the highest strain rate curve. After matching this 'start time' to the highest strain curve, the subsequent evolution of the anisotropy behaves very similarly (the curves lie on top of each other) for the highest

AXC strain rates. The lowest strain rate behaves slightly differently following the removal of strain. Note that time has not actually been scaled in this plot, just shifted. Also note that this observation of the flow after strain is removed, also confirms the interpretation that return-to-isotropy is a stronger process for turbulence generated by contraction than it is for turbulence generated by expansion.

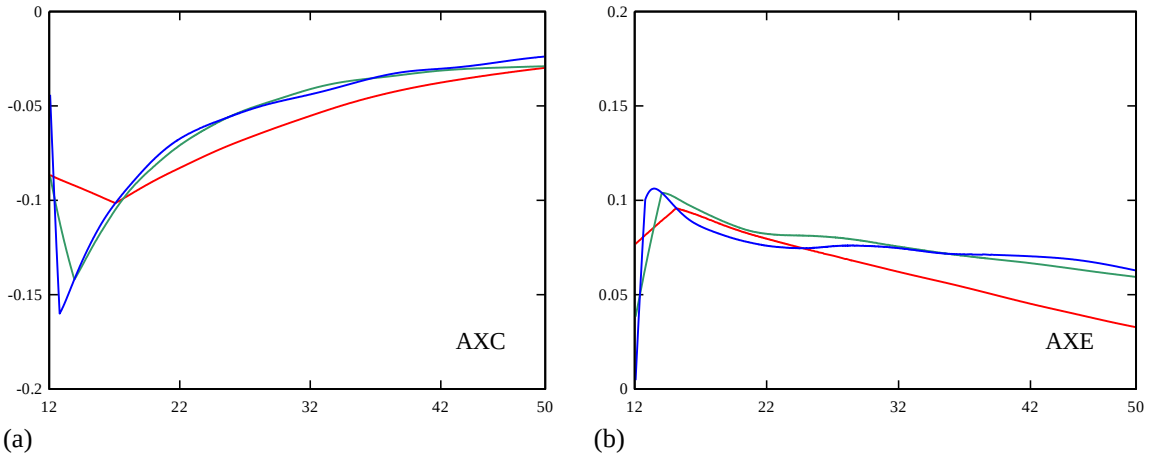

(a) (b)

Figure 5.6. b_{11} with each curve translated on the x-axis such that the point in time at which straining is stopped coincides with a point on the largest strain case allowing for a comparison of the return processes. (a) AXC IC1 (b) AXE IC2.

5.3.5 Invariant Map

The anisotropy invariant map [85] is a common way to look at the return-to-isotropy problem. The anisotropy tensor has zero trace, so the state of the turbulence anisotropy can be described by the other two invariants, $II = -(1/2)b_{ij}b_{ji}$ and $III = (1/3)b_{ij}b_{jk}b_{ki}$. Figure 5.8 shows the variation of the turbulence anisotropy invariants (for the highest strain rate cases) as it progresses through the straining process and then through the decay process for both (a) AXC and (b) AXE. Both sets of initial conditions are shown. In all four cases, the turbulence starts close to the origin (isotropy). The solid

red lines, no symbols, show the evolution as the turbulence is strained and moves away from isotropy. When the strain is removed (colored

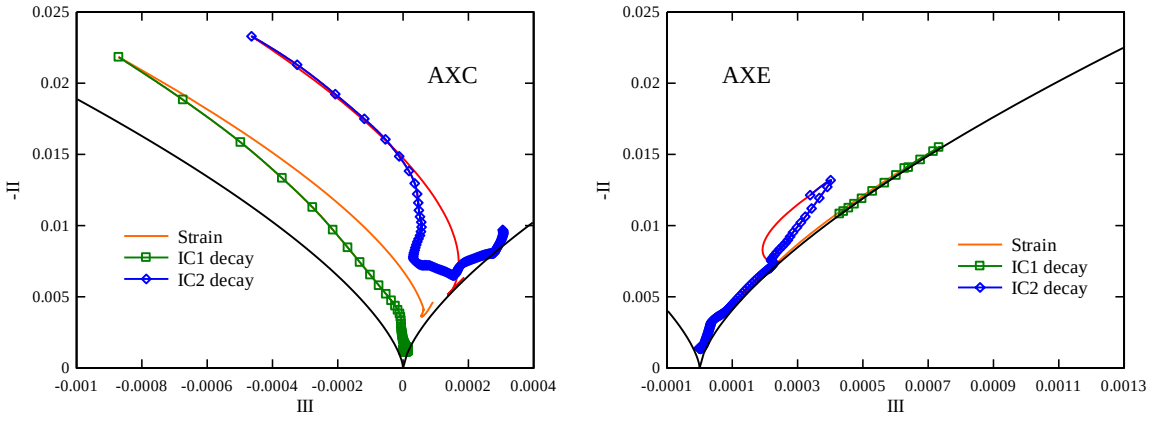

(a) (b)

Figure 5.7. Invariant plots of Reynolds-stress anisotropy subjected to high strain rates (a) AXC (b) AXE. The lowest black curves bound the realm of realizability. Solid red lines show the trajectory during the straining process and lines with symbols show the anisotropic decay trajectories.

symbols) the state generally moves back toward $-II = 0$, $III = 0$ (return-to-isotropy). An equal amount time exists between the symbols during each of the decay processes shown. The return-to-isotropy process slows as the turbulence becomes more isotropic. At very long times the trajectories tend to wander without a clear direction towards the origin. It is believed that this is the result of the fact that at long times the simulations are corrupted by the influence of the finite domain size. The two initial conditions produce somewhat different trajectories due to differences in their initial states, but the overall affect of the strain and subsequent decay are still clear in each case.

The rate of return-to-isotropy can be quantified by the expression

$$\rho^* = \frac{k/(dk/dt)}{II/(dII/dt)} \tag{5.5}$$

which compares the rate of decay of the kinetic energy to the rate of decay of the second invariant. Choi and Lumely [11] found experimentally values of ρ^* for AXC cases are approximately 2.5 times larger than for AXE cases. Figure 5.9 shows a similar effect for this data. With AXC (figure 5.9a) returning 2.5 times faster for short times, and up to 4 times faster at longer times than AXE (figure 5.9b).

Figure 5.10 shows the effect of the variation in strain rate on both AXC and AXE. Figure 5.10(a) and (c) show AXC IC1 and AXC IC2 respectively while figure 5.10(b) and (d) show AXE IC1 and AXE IC2 respectively. Each of the four plots shows the effects of the three different strain rates. For the AXC cases the tendency during the return process (lines with symbols) is for the turbulence to seek a trajectory that lies closer to the -*III* boundary of realizability (solid, black curve beneath and to the left of the strain/decay curves) than their preceding strain trajectories. This boundary is the limit of perfectly axisymmetric turbulence (with two large and one small Reynolds stress). It also appears that during the straining process the lower the strain rate the more the tendency to move toward the -*III* boundary. This motion towards axisymmetry is thought to be a result of the nonlinear return-to-isotropy process. Nothing in linear RDT theory would suggest this behavior.

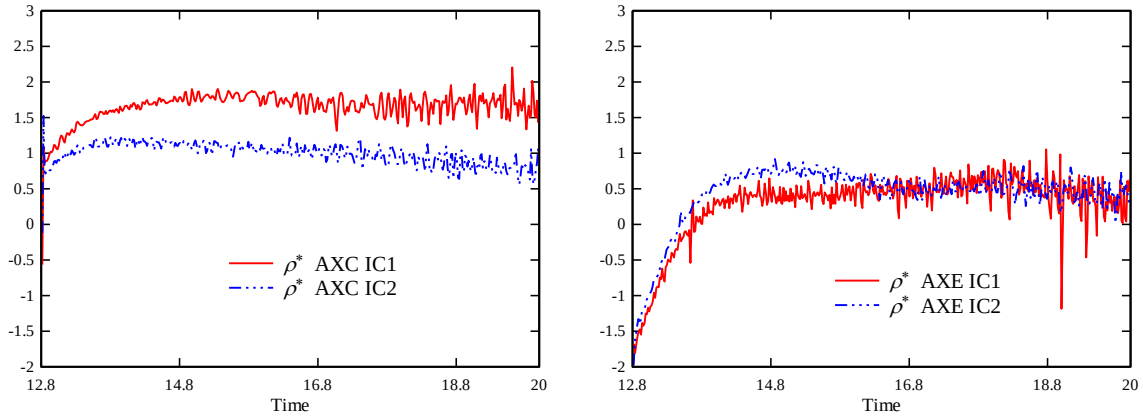

(a) (b)

Figure 5.8. Comparing relative return rates of AXC and AXE. ρ^*, Eq. (5.5), is a ratio of the time scale of decaying turbulent kinetic energy to that of return-to-isotropy.

The AXE cases exhibit significant differences from IC1 to IC2. For IC1 (figure 5.10a) the different strain rates produce very similar results moving up and back immediately adjacent to the *+III* boundary of realizability both during the strain and return processes. The *+III* boundary represents perfectly axisymmetric turbulence with one large and two small Reynolds stresses. IC2 (figure 5.10b) shows different behavior from one strain rate to the next. At the onset of strain the strain-rate trajectories immediately diverge only to align again prior to the termination of strain. It is thought that the strain is acting on some transient particular to that initial condition at early times in the straining process. The lowest strain rate shows significant divergence from higher strain rates both during the straining process as well as during return-to-isotropy. Upon removal of strain the lowest strain rate trajectory reverses direction and for a time decays back along its strain trajectory. The two highest strain rates return closer to the *+III* boundary than their respective strain trajectories. Upon removal of the highest strain rate the turbulence continues to become slightly more anisotropic (for a short time) before evolving toward the *+III* boundary and back towards isotropy. This is the 'recovery' stage noted earlier, which is also found to occur in turbulence subjected to plane strain Zusi & Perot [100].

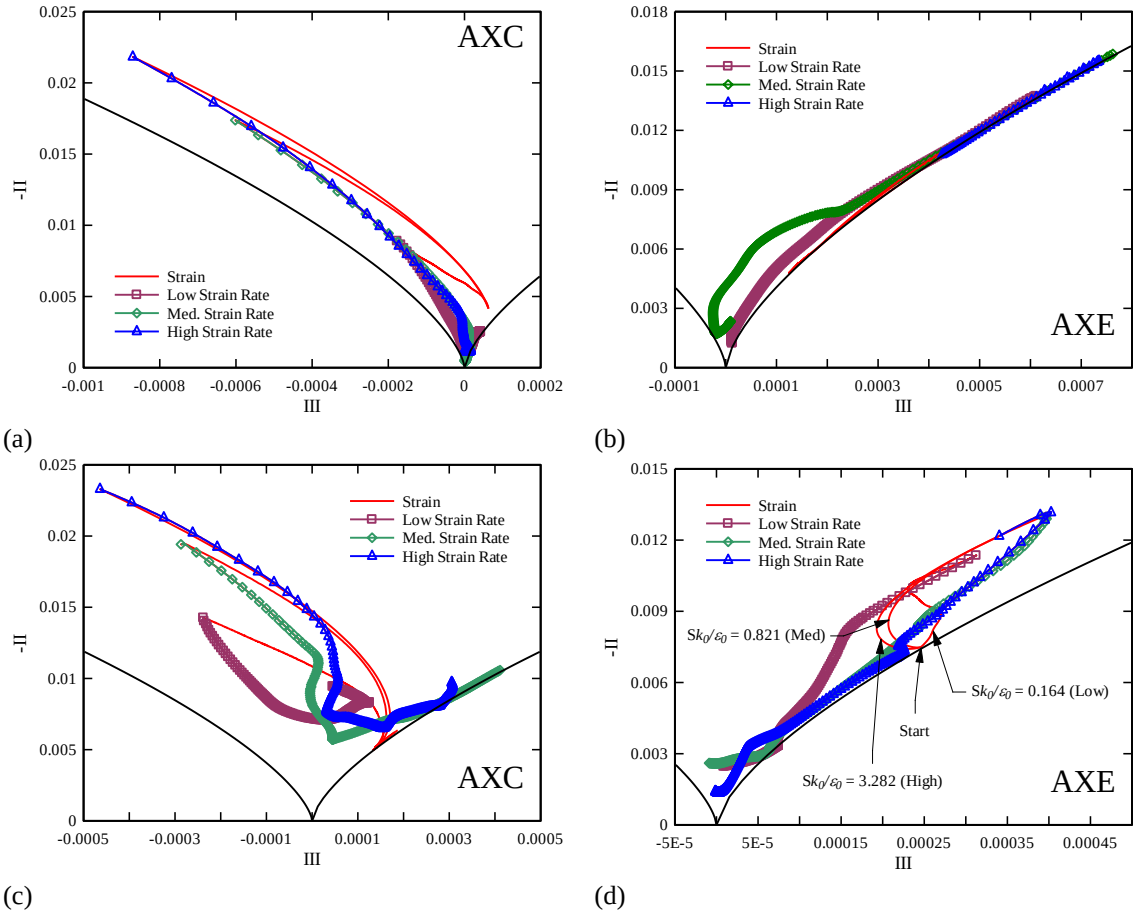

Figure 5.9. Invariant maps showing the straining process (red lines no symbols) and the return-to-isotropy process (symbols). AXC: (a) IC1 and (c) IC2. AXE: (b) IC1 and (d) IC2.

5.3.6 Decay Rate

Figure 5.11 shows the decay rate, n, as a function of time with two sets of initial conditions subjected to the high and low strain rates of both AXC and AXE. The decay rate is a sensitive measure of the energy cascade. It represents the power at which the kinetic energy decays, $k(t) = k_0(t - t_0)^{-n}$ and is calculated via the expression, $n = \left[\frac{d(K/\varepsilon)}{dt}\right]^{-1}$. The numerical calculation of this quantity requires small time increments for an accurate representation of the derivative [33]. Before the strain is applied at time 12 the turbulence usually approaches the theoretically expected Saffman [86] high

Reynolds number value of 6/5 (shown with a dashed black line on the figures). The low Reynolds number Saffman value of 3/2 is also shown on the figures.

The low strain rate cases of both AXC and AXE, figure 5.11(a) and (c) respectively, do not significantly change the decay rate. However, the high strain cases Figure 5.11(c), (d) show a significant reduction in the decay rate just after the strain is removed. This is due to the disruption to the energy cascade that strain (or any external forcing) produces. Disruption of the energy cascade leads to less energy dissipation, less loss of turbulent kinetic energy with time, and a smaller n. After the strain is removed the decay rate can be seen to increase significantly with time, in the cases of high strain rates, in order to recover to the theoretical values (in the theoretical limits between 1.2 to 1.5). The decay exponents of the low strain rate cases also increase but much less adjustment to the decay rate is needed for them to enter the region of 1.2 to 1.5 limits. In most cases of both AXC and AXE, after a long enough time, the decay rate appears to approach the low Reynolds number Saffman theoretical value of 1.5. In at least one case (AXC IC2) the decay exponent eventually moves towards the domain constrained value of 2 [87] at very long times (after about 100 seconds). Perot [33] looks at the effects of Reynolds number on decaying turbulence in more detail and shows that the decay rate transition from 1.2 to 1.5 is not solely related to the Reynolds number.

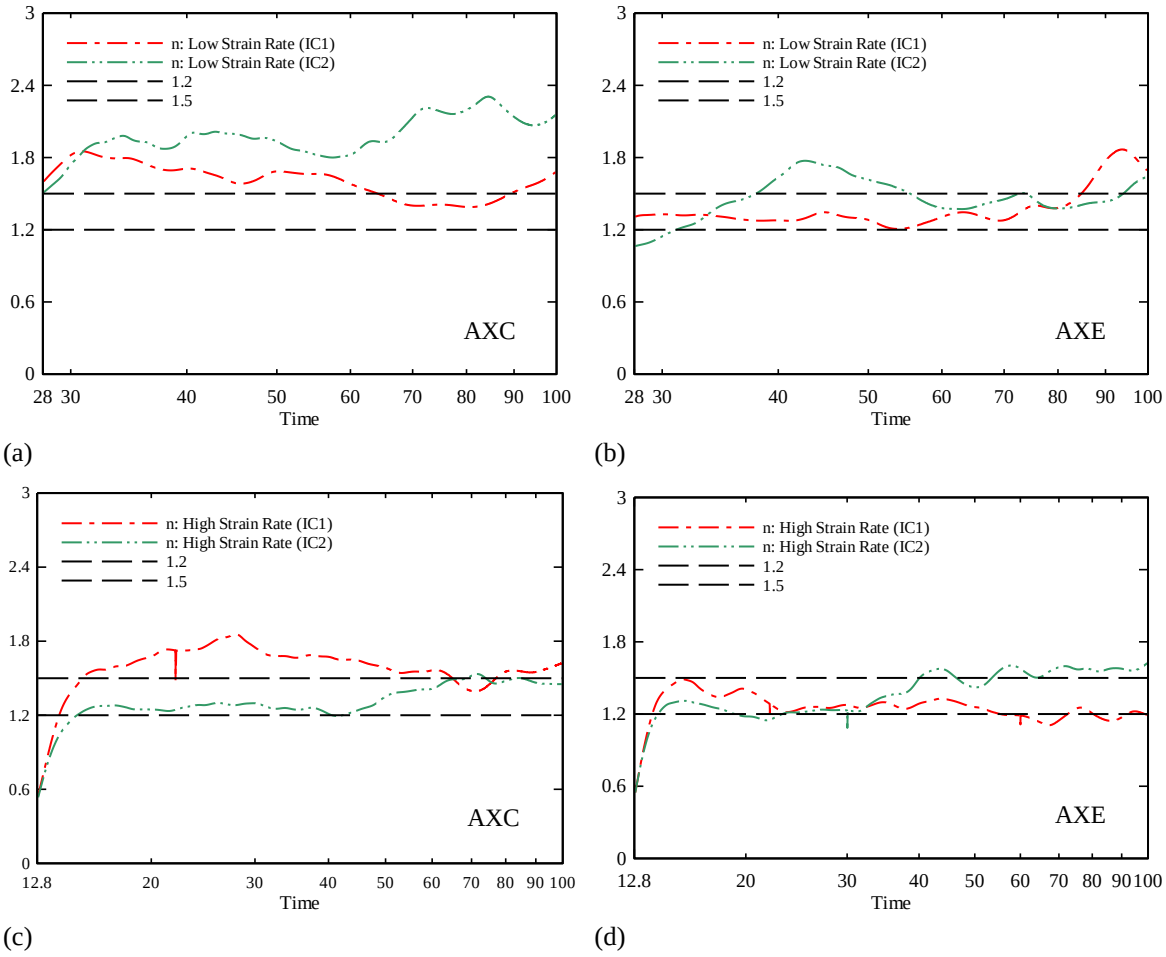

Figure 5.10. Decay exponent, n, for AXC (a), (c) and AXE (b), (d). Resulting from the exposure of initial conditions IC1, IC2 to low strain rates (a) and (b) and high strain rates (c) and (d).

5.4 MOdeling

5.4.1 Anisotropy Based Models

The linear model of Rotta [65], or the more general non-linear models (such as Sankar and Speziale [18]), attempt to represent the return-to-isotropy using only the anisotropy tensor itself. A typical model for return-to-isotropy takes the form,

$$\frac{db_{ij}}{dt} = (1 - C_1)\frac{b_{ij}}{T} + C_1^n \frac{\left(b_{ij}^2 - \frac{1}{3} b_{kk}^2 \delta_{ij}\right)}{T} \tag{5.6}$$

It can be seen that in order for this model to allow for return-to-isotropy the value of C_1 must be be greater than 1 (see Durbin and Reif [63] for more details). The values for the constants C_1 and C_1^n can be reverse calculated from the DNS data and are shown in figure 5.12 for both initial conditions of AXC and AXE.

Since these are constants for a return-to-isotropy model we are only interested in their values after the strain is removed, which in all cases in figure 5.12 is after 12.8 seconds. Even for the same strain rate there is significant variation of these constants as a function of time and between different initial conditions. These results indicate that such a model, with any fixed set of constants would have difficulty producing accurate result for this variety of turbulence conditions.

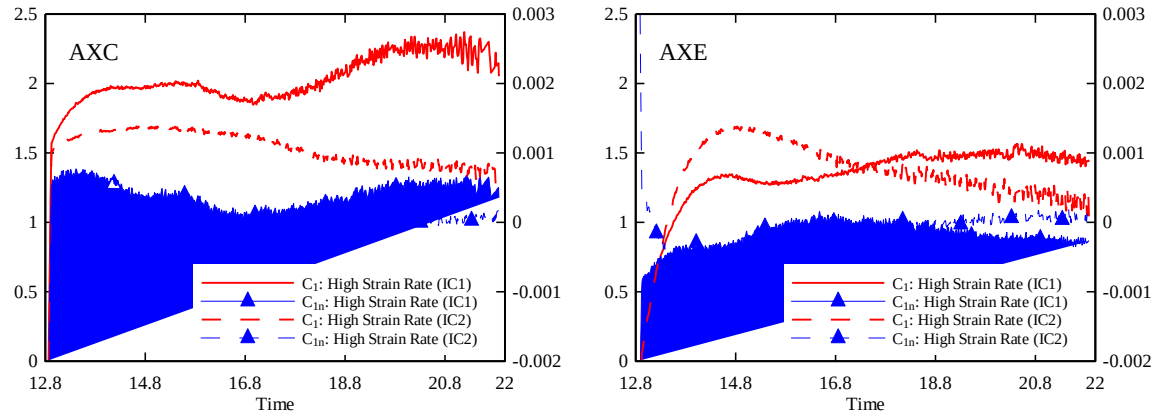

(a) (b)

Figure 5.11. Constants for the non-linear model Eq. (8). c_1 left y-axis, c_1^n right y-axis. High strain rate: (a) AXC IC1 (solid), IC2 (dashed), (b) AXE IC1 (solid), IC2 (dashed).

References [9] and [10] contain examples of models where such constants are functions of the anisotropy invariants (*II* and *III*) or other dimensionless variables such as the Re. However as discussed in Pope [59], no matter how complex the functional

dependence of the model constants, a return-to-isotropy model that only depends on information contained in the anisotropy tensor produces unique trajectories on the invariant map that never cross one another back to the origin (isotropy). For these types of models, any particular starting point on the invariant map cannot produce different evolutionary paths (trajectories) back to isotropy. Figure 13 shows return trajectories that have crossing paths during their return-to-isotropy and thus this DNS data suggests that additional information must be used in return-to-isotropy models. Section 4.2 discusses the performance of a model which accounts for additional information in the form of eddy structure by way of two-point correlations.

5.4.2 Oriented-Eddy Collision Model

The oriented eddy collision (OEC) model is discussed in Martell and Perot [1]. This model looks like a collection of Reynolds stress transport equations coupled with a set of transport equations for the inverse two-point correlation lengths. The information contained in the OEC model can be used to approximate the two-point velocity correlations (not just their peak values, which are the Reynolds stresses). In the OEC model the two-point correlation is approximated by

$$Q_{ij}(\boldsymbol{x},\boldsymbol{r}) = \sum \hat{R}_{ij}(\boldsymbol{x},t) f(|\boldsymbol{q}(\boldsymbol{x},t)| \cdot \boldsymbol{r}) \tag{5.7}$$

Where $\hat{R}_{ij}(\boldsymbol{x},t)$ and $\boldsymbol{q}(\boldsymbol{x},t)$ are determined by the model and the function f is usually chosen to be a decaying exponential. The OEC model uses a classic linear return-to-isotropy model for the velocity fluctuation and also the simplest possible linear return-to-

isotropy model for the inverse correlations lengths, $\boldsymbol{q}$. However, the time scale for the $\boldsymbol{q} - recovery$ is faster than that of the velocity-return.

The ability of the OEC model to predict both AXC and AXE is shown in figure 16. This figure shows the Reynolds stresses for both cases subjected to high strain rates. The OEC model is exact in the large strain RDT limit, so the ability to capture the effect of straining which is normally quite difficult for turbulence models is not a problem for this model. The subsequent anisotropic decay (return-to-isotropy) is not exact for the OEC model. But the model uses the same information necessary to exactly capture RDT to also model the recovery process. The agreement over both test cases (with the same model constants) is reasonable.

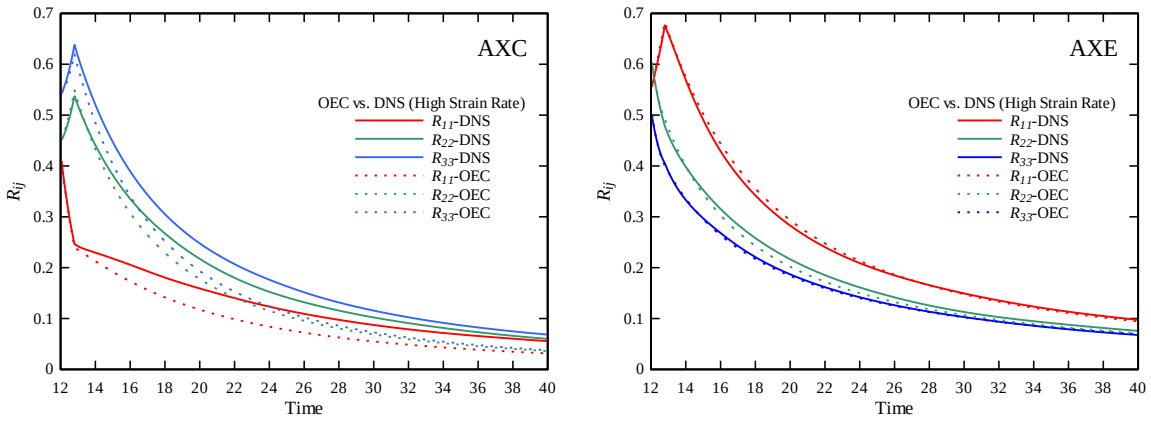

(a) (b)

Figure 5.12. Reynolds stresses for AXC IC1 (a) and AXE IC2 (b). DNS data (solid lines) and the OEC model (C_R = 0.5, C_L = 0.67) predictions (dashed lines).

A more sensitive test of the OEC model is to plot the results on the anisotropy invariant map as shown in figure 5.14. Here the OEC model can be seen to produce the correct qualitative features for cases of both AXC and AXE. The straining process is exponentially sensitive to initial conditions, and therefore the OEC results do not progress along exactly the same trajectories as the DNS simulations. These results were

produced by initializing the model with the R_{ij} initial conditions only. It is thought that incorporating not only the correct R_{ij} initial conditions but also the correct two point correlations length scale initial conditions will aid in the model's performance. The capability of incorporating information from the two-point correlation initial conditions is currently being incorporated into the model.

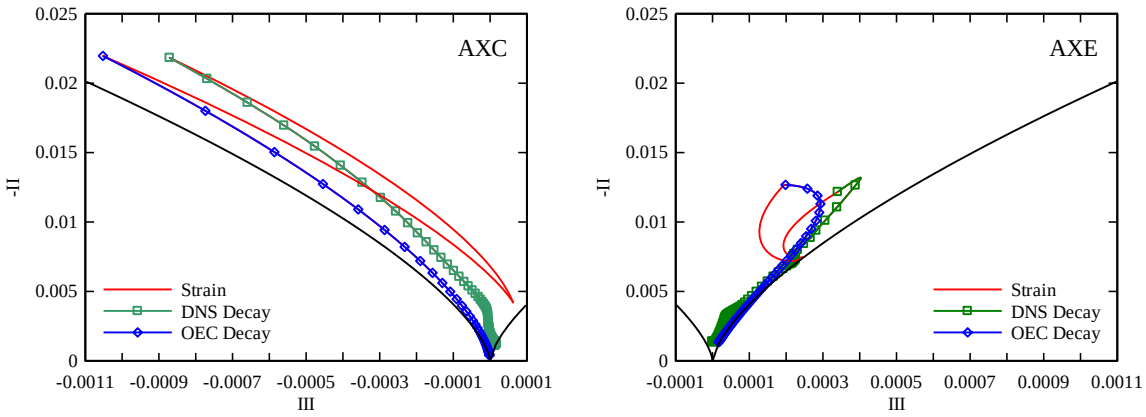

Figure 5.13. OEC vs. DNS: (a) AXC IC1, (b) AXE IC2 both subjected to high strain rate.

5.5 Discussion

The simulations presented in this work add to a growing set of canonical test cases of the affect of strain on isotropic turbulence and its post-strain return-to-isotropy. These simulations have a 512^3 mesh resolution in order to resolve and capture the large scales accurately. The large scales are known from theory to govern the behavior of isotropic decay. They also appear to strongly influence the behavior of anisotropic turbulence.

The initial conditions for the presented simulations were generated by mechanically stirring the fluid. This is done in the numerical simulation by moderate size

no-slip cubes. This is done so that all large scale turbulence is formed by the turbulence process itself and not set by the researchers. The very largest scales of the turbulence (which govern the decay behavior) are much larger than the initial mixing cube size. There is very little human input to the simulation that influences the large scale turbulence. The very largest scales result from the Navier-Stokes equations and their interaction with a random arrangement of small cubes.

In these simulation at long times we do not see a return-to-isotropy, but a return to the background level of statistical anisotropy that the simulations began with. Comte-Bellot and Corrsin [36] make a similar observations in their experiments, as do Kang [89]. George [90] provides a possible theoretical argument for this behavior.

Because the large scales are much smaller than the domain size in these simulations, the turbulent Reynolds numbers are not large. Still, they are comparable to some experimental Reynolds numbers, and they appear to be high enough (at least for IC2) to produce the isotropic decay rate (n=6/5) predicted by Saffman [86] for high Re turbulent decay both before and well after the straining process. It was found that the straining process, in both AXC and AXE, reduces the decay exponent (i.e. decay rate) in the highest strain rate cases and at least limits the increase of the decay rate in low strain rate cases. It was found that after straining, the decay rate increases to levels in the range of 6/5 to 3/2 Saffman's [86] predictions of high and low Reynolds number values. For cases of low strain rate both AXC and AXE can be seen to be increasing above the 3/2 level perhaps indicating a domain constrained condition (n=2.0) (see Stalp *et al*. [87] and Touil *et al*. [88]).

An important observation of this paper is the confirmation that return-to-isotropy occurs in two stages, a ***recovery*** stage immediately after the strain is removed, in which some of the anisotropy components can still be increasing (and the decay rate differs from its isotropic value), and the ***return*** stage where the velocity fluctuation anisotropy tends to zero (and the classic isotropic decay rates are applicable). We hypothesize that the recovery stage is the turbulence structure (two-point correlation lengths) returning to isotropy at a faster rate than the velocity fluctuations return (which is the classic return stage). The observation in the DNS data of trajectory crossing support the idea that the evolution of anisotropic turbulence cannot be captured by the information in the anisotropy tensor alone.

Traditional return-to-isotropy models are handicapped because they do not account for the presence of the recovery stage of anisotropic turbulent decay. It has been shown that even for the same mean flow conditions (i.e. AXC or AXE), different initial conditions produced quite different values of constants in the classic non-linear return-to-isotropy models. Like the OEC model, the models of Kassinos and coworkers [28], [29] can also predict the two stages of anisotropic decay, recovery and return. The underlying models are related but not the same because of the difference in philosophy about what extra information is being included in the model (one-point correlations of derivatives, versus two-point length scales). Both the modeling results of Kassinos and the current DNS work indicate that the recovery stage of anisotropic decay requires knowledge and representation of the turbulent structure.

This work only examines two types of anisotropic turbulence (AXC and AXE), but it is encouraging that the OEC model gives fairly reasonably predictions for all the

different initial conditions and strain rates with a single set of constants. Simulation and modeling of other canonical turbulent flows are ongoing.

CHAPTER 6

ROTATION

6.1 Overview

The remainder of the research covered by this work will examine the effects of rotation on return-to-isotropy and the turbulence decay rate. The affect of rotation on Reynolds stresses, as well as anisotropy components, is presented along with the traditionally measured Reynolds number and turbulence length scales. The effect of rotation on the structure of the turbulence in the form of longitudinal two point correlations, as well as qualitative velocity contours, is presented. The degree to which rotation inhibits the decay of turbulent kinetic energy will be evaluated both during rotation as well as after rotation has ended.

6.2 Introduction

The effect of rotation on isotropic turbulence and the affected turbulence's behavior subsequent to the removal of rotation is an important baseline flow condition to understand in order to advance turbulence models. In this study rotation is imposed by spinning the flow around the z-axis (Ω_z). The characterization of rotating turbulence is often done by way of the non-dimensional number $Ro = \varepsilon_0(\Omega k_0)^{-1}$ known as the turbulent Rossby number. The magnitude of this number defines the relation of the mean flow rotation rate Ω (with units of 1/time) to that of to the turbulent time scale k_0/ε_0 (with units of time). Note the turbulent Rossby number is inversely proportional to the

mean flow rotation rate Ω. Exposing isotropic turbulence to rotation is one of the canonical cases used to study the effects of mean flow variation on isotropic turbulence.

The effects of rotation on the decay of isotropic turbulence have been studied extensively as rotation is present in many turbulent flows, such as the Earth's atmosphere and oceans as well as in industrial applications such as rotorcraft, wind turbines, turbo machinery, rotating channels etc. [102]. Other authors have pursued investigations into the effects of rotation on isotropic turbulence both experimentally and through simulation. However no prior simulations have used numerical simulation with initial conditions generated by mechanical mixing as has been done herein. In addition, this work focuses on turbulence behavior *after* the rotation is stopped.

As is pointed out in early works by Wigeland & Nagib [103], Bardina, Ferzinger & Rogallo [104] and Speziale, Mansour & Rogallo [105], the effects of rotation on turbulence reveals some interesting results. Rotation has little effect on the isotropic state of the turbulence while the energy decay is suppressed. The cause of this suppression is related to the disruption of the energy cascade, but it is not particularly well understood. Understanding this decay suppression is of great importance to the proper modeling of rotating turbulence.

Speziale, Raj & Gatski [106] evaluate models by Pope [107], Hanjalic & Launder [108], Bardina [104] and Raj [109] and their ability to predict the dissipation rate under the influence of rotation. They point out that eddy viscosity based models depend only on mean velocity gradients and are blind to the presence of rotation. They find deficiencies in the models they review ranging from a limited effectiveness (low rates of rotation only) to unrealizable results leading to negative values of dissipation rate.

Isotropic turbulence subjected to rotation is unique among the cases studied in this work in that the geometry of the overall domain is not cubic at any time during the mixing or decay process. Neither the overall domain nor the mesh geometry change shape during the entire simulation but the domain is designed such that it is twice the size along the axis of rotation. This means the domain is given by $L_x = L_y = (1/2)L_z$. The mesh is also scaled appropriately so that the cell aspect ratio remains unity, thus the mesh sizes are 512_x x 512_y x 1024_z. Figure 6.1 shows the overall shape of the domain which is maintained throughout the simulation with the z-axis being the axis of rotation.

It is commonly hypothesized that under the influence of rotation turbulent velocity correlations oriented parallel to the axis of rotation are stronger (at a certain radius) than those oriented normal to rotation axis, Thiele [110]. This is why extra room is provided in the domain along the direction of rotation. Perot [33] showed that as large-eddy length scales grow to 1/4 the size of the periodic domain they can begin to affect the turbulent statistics. In order to minimize the effects of the domain's periodicity on the turbulence statistics the domains was designed such that the domain's length aligned with the axis of rotation is twice the length of the other dimensions.

The non-dimensional rate of rotation is defined by $\Omega k_0/\varepsilon_0$. With the rotation rate, $\Omega = 2\pi \frac{\text{rotations}}{\text{second}}$, varied in order to compare the affect of various rotation rates during both during and after rotation. Although the rotation rate is varied, the total number of rotations of the fluid remains the same across all simulations such that $\Omega T = 3.0$ where T is to total rotation time. The Rossby number, $Ro = \varepsilon_0/k_0\Omega$ (or the inverse of the non-dimensional rotation rate), is often used to characterize the mean flow rotation. The Rossby number is unintuitive because it goes to infinity when there is no rotation. We

will use $\Omega k_0/\varepsilon_0$ to also remain consistent with the previous straining cases where the non-dimensional strain rate is characterized using $S\,k_0/\varepsilon_0$.

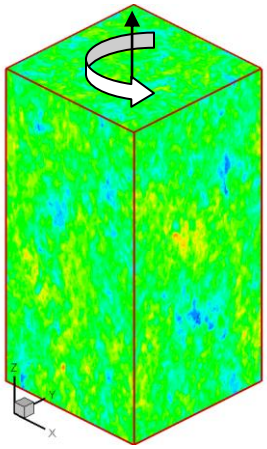

Figure 6.1 Domain used in rotation simulations with $\boldsymbol{L_x = L_y = (1/2)L_z}$.

6.3 Results

6.3.1 Initial Conditions

A number of cases have been run to investigate the decay of anisotropic turbulence generated by rotation. Table 6.1 shows the five different rotation rates (RR) used to examine the effects on a set of three initial conditions.

	k_0	ε_0	Re_0	$Re_{\lambda 0}$	T_0	L_0	$\Omega\, k_0/\varepsilon_0$	Ro_0	L_η	$L_\eta/\Delta x$
IC1	0.885	0.137	573.445	61.830	6.477	6.094	Low = 2.035	0.491	0.052	0.555
							MedLow = 4.070	0.246		
							Med = 10.174	0.098		
							MedHigh = 20.348	0.049		
							High = 40.695	0.025		
IC2	0.597	0.100	354.857	48.639	5.948	4.594	Low = 1.869	0.535	0.056	0.599
							MedLow = 3.738	0.268		
							Med = 9.344	0.107		
							MedHigh = 18.688	0.054		
							High = 37.375	0.027		
IC3	0.942	0.165	536.773	59.820	5.700	5.531	Low = 1.791	0.558	0.050	0.529
							MedLow = 3.581	0.279		
							Med = 8.954	0.112		
							MedHigh = 17.907	0.056		
							High = 35.815	0.028		

Table 6.1 Initial conditions, time = 17.0 seconds**.**

Table 6.1 data is defined as follows with turbulent kinetic energy k_0, dissipation ε_0 and turbulent Reynolds number $Re_0 = {k_0}^2/\nu\varepsilon_0$. It also shows the Taylor micro-scale Reynolds number $Re_{\lambda 0} = \sqrt{(20/3)Re_0}$, large-eddy turnover time $T_0 = k_0/\varepsilon_0$, large-eddy length scale $L_0 = {k_0}^{3/2}/\varepsilon_0$, the Rossby number $Ro = \varepsilon_0/k_0\Omega$, and the Kolmogorov length scale, $L_\eta = \nu^{3/4}/\varepsilon^{1/4}$. A grid spacing ΔX that is twice the Kolmogorov length scale or smaller, is considered by most DNS practitioners to be more than sufficient for resolving small scales. The subscript zero defines the data as taken from the time of the start of rotation which is considered the time of initial conditions.

As with the other cases in this work initial conditions were generated using the shaking technique as described in section 3.2. A set of three initial conditions were generated in order to compare the effects of initial conditions. Each of the initial conditions was rotated at five different rotation rates for a total of 15 separate

simulations. Rotation simulations were carried out using the original Stag3D code (FORTRAN) ported to GPU architecture (C++/CUDA). A rotational computational domain twice the size of the other canonical cases in this study would mean twice the computational resources required to complete the simulations. However, the GPU based code; running at approximately 25x the speed of the FORTRAN code meant an overall speedup of approximately 12x. Given the increase in computation speed it was decided to extend the turbulence generation time (the most computational demanding portions of the simulation) in order to ensure thorough stirring of the fluid and generation of isotropic turbulence. As such the evolution of the simulation as described in figure 3.1 evolves as follows for rotation simulations. Stage 1 (shake): $0.0 \rightarrow 10.0s$, Stage 2 (settle): $10.0s \rightarrow 12.0s$, (remove cubes): $12.0s$, (settle) $12.0 \rightarrow 17.0s$, Stage 3 (rotate): $17.0 \rightarrow 17.0 + (3.0\pi/\Omega)$, Stage 4 (decay): $17.0 + (3.0\pi/\Omega) \rightarrow 100.0$. Given the slight variation in k_0, ε_0 across the initial conditions there is some slight variation in the non-dimensional rate of rotation $\Omega k_0/\varepsilon_0$ for each initial condition.

6.4 time development

Figures 6.2a,b,c,d,e show the affects of rotation rate on Reynolds number and the large-eddy length scale across the set of three ICs (with rotation occurring within the red shaded region). As seen with the other canonical cases, namely plane strain, axi-symmetric contraction (AXC) and axi-symmetric expansion (AXE), the affect during rotation is to cause both Re and L to increase. Figure 6.2 shows that during the period of rotation the growth rate of Re and L are proportional to rotation rate. Figure 6.2 also

shows that in the lower rotation rate cases both Re and L decrease following the end of rotation while in the higher rotation rate cases both Re and L continue to grow throughout the simulation, $t \rightarrow 100.0s$. All cases reveal a $recovery$ period where rotation has stopped but length scale continues to grow for a period of time. This is clearly evident in the low rotation rate case from time $t = 47.0$ (the end of rotation) to roughly $t = 57.0$ where L begins to decrease. Recalling from the cases of AXC/AXE, it is hypothesized in this work that during this *recovery* period the structure of the turbulence (the two-point correlation lengths) are returning to isotropy faster than the velocity fluctuations are returning. The effects on turbulence statistics of the intermediate rotation rates across all three ICs show similar results.

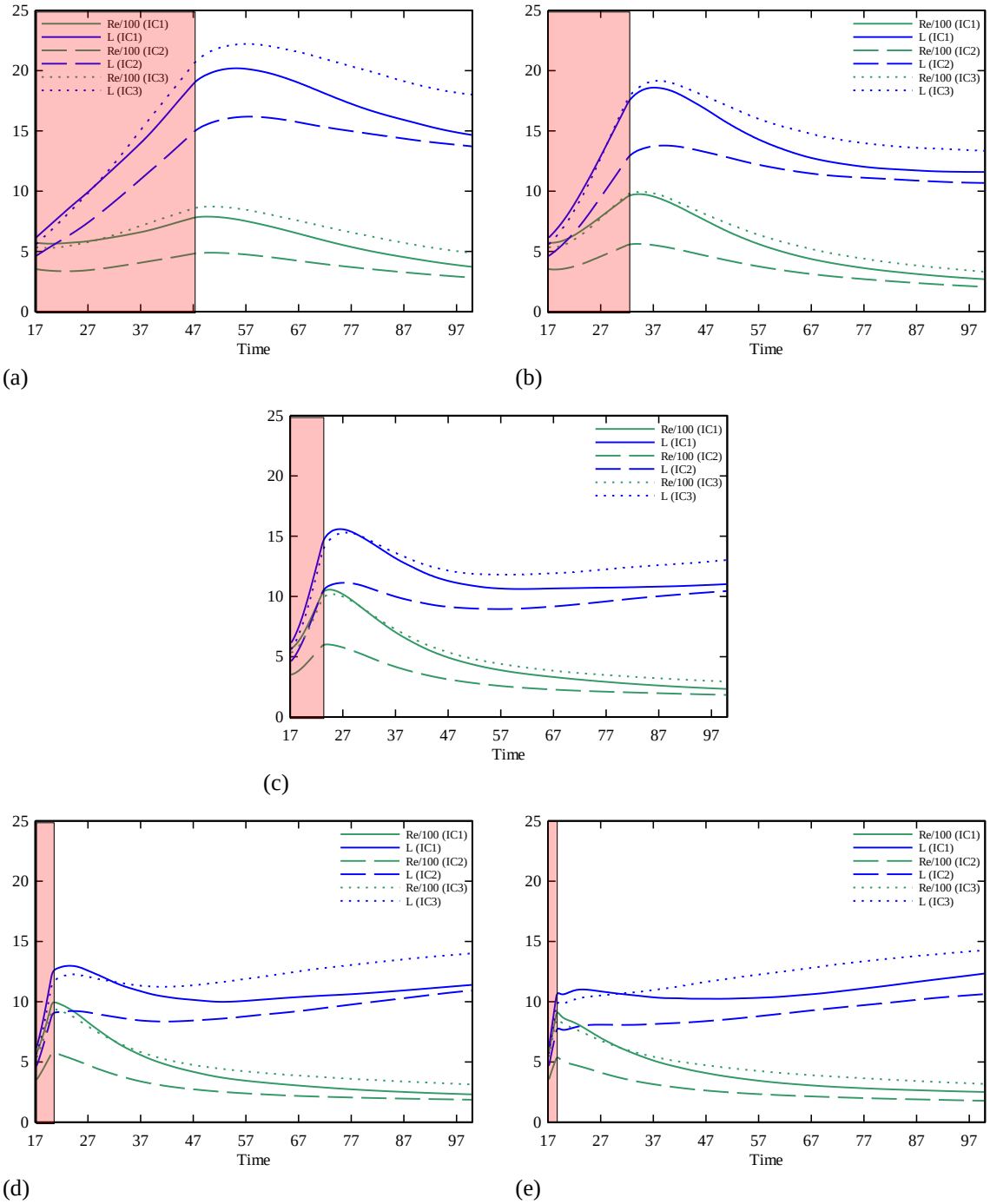

Figure 6.2 The effect of rotation rate Reynolds number and large eddy length scale across three different initial conditions. Rotation rates of low, MedLow, Med, MedHigh and High are shown in a, b, c, d, and e respectively. Rotation occurs within the red shaded region.

Figure 6.3 shows the effects of rotation rate on Reynolds stress and anisotropy tensor components. It can be seen that while rotation reorients the tensor components it

does little in the way of altering the magnitude of these values. It is hypothesized in this work that rotation has very little effect on the Reynolds stress anisotropy. The values in the second row of figure are within statistical noise at all times. The effect of rotation is thought to manifest itself almost entirely in the two-point correlations (or what we call the turbulent structure).

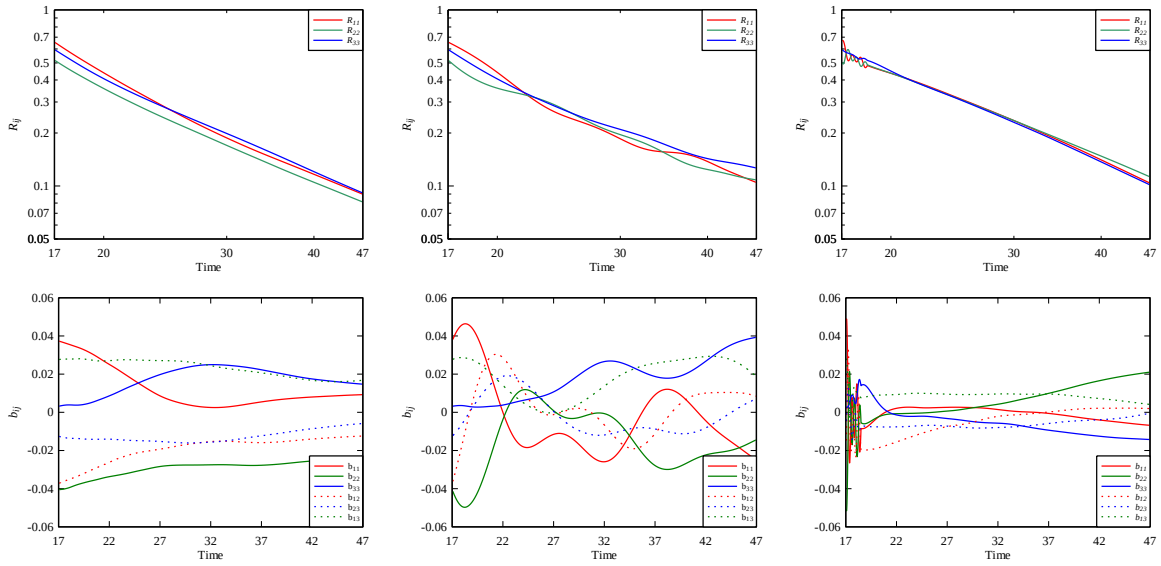

(a) (b) (c)

Figure 6.3 The effect of rotation on Reynolds stress and normalized anisotropy tensor components of IC1. (a) No rotation, (b) Low rotation rate, (c) High rotation rate.

6.5 Turbulence structure and decay rate

Previous authors such as Speziale [106], Teitelbaum [102], Yang [111] and references within, discuss the effects of rotation on the dissipation rate of turbulence. Rotation disrupts the energy cascade limiting the turbulence's ability to dissipate energy. The mechanism by which this takes place is not well understood. Tsuei & Perot [112] describe rotation altering the orientation of the turbulent eddies which influences the

conventional turbulent structure. Cambon [113], Theiele [110], Teitelbaum [102] discuss structural changes within the turbulence resulting from rotation with observations by Theile [110] that strong velocity correlations, $u_i'(x)u_i'(x+r_i)$, along the axis of rotation result in the quasi two-dimenionalization of the flow. Further stating that energy fluxes weaken in the presence of rotation, in particular along the axis of rotation, and that the classical picture of energy transfer by way of eddy breakup is stronger in eddies perpendicular to the axis of rotation where coherent structures remains relatively intact.

Figure 6.4 shows the longitudinal autocorrelations from IC1, both normalized and non-normalized. Shown in columns from left to right are $f(r_1), f(r_2), f(r_3)$ with $f(r_3)$ being aligned with the axis of rotation. Rotation can be seen to increase the lateral extent of these correlations in each component direction. As suggested by Theile [110], under the effects of rotation correlations along the axis of rotation increase more than those align perpendicular to the axis of rotation. Figure 6.4c clearly shows a larger increase in the longitudinal autocorrelation function along the axis of rotation than the autocorrelations along the other orientations aligned perpendicular to rotation, Figures 6.4a and 6.5b.

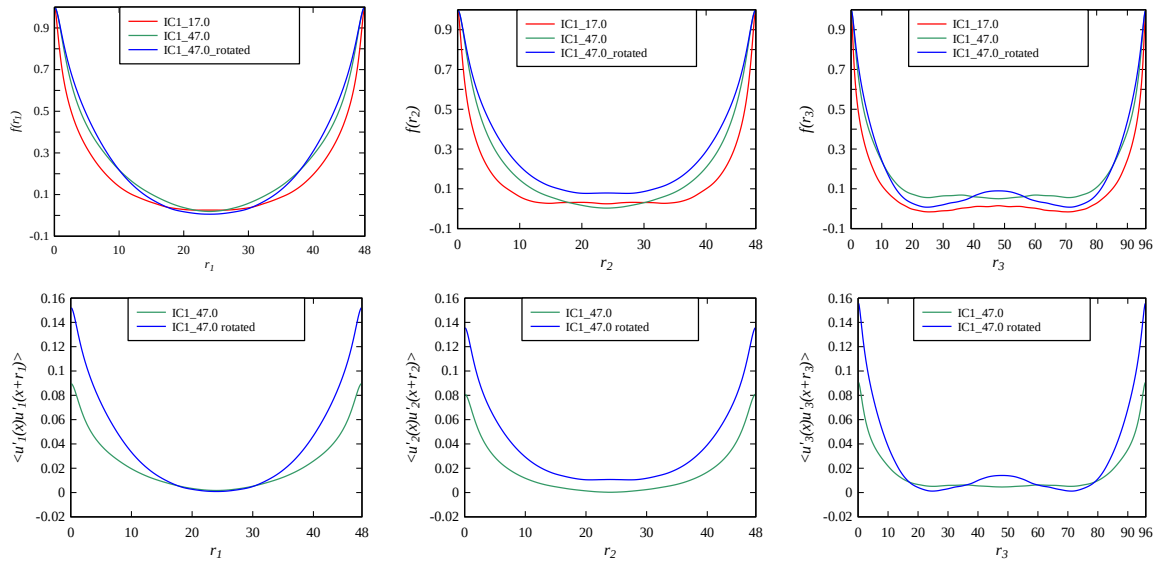

(a) (b) (c)

Figure 6.4 Longitudinal velocity autocorrelation functions, $\boldsymbol{f(r_i) = \langle u_i'(x)u_i'(x+r_i)\rangle / \langle u_i'(x)u_i'(x)\rangle}$, from IC1 case with low rotation rate. Top row compares IC1 values at 17.0 seconds with the rotated and non-rotated cases at time 47.0 seconds. Bottom row are not normalized by $\boldsymbol{\langle u_i'(x)u_i'(x)\rangle}$: (a) top $\boldsymbol{f(r_1)}$, bottom $\boldsymbol{f(r_1)\langle u_1'(x)u_1'(x)\rangle}$, (b) top $\boldsymbol{f(r_2)}$, bottom $\boldsymbol{f(r_2)\langle u_2'(x)u_2'(x)\rangle}$, (c) top $\boldsymbol{f(r_3)}$, bottom $\boldsymbol{f(r_3)\langle u_3'(x)u_3'(x)\rangle}$. Note: $\boldsymbol{r_3}$ is aligned with axis of rotation.

Figure 6.5 shows contour plots of the w-velocity component (the component aligned with the axis of rotation). Figure 6.5a shows contours at the time just before rotation, $t = 17.0$. Figure 6.5b shows the same contours without rotation at time $t = 47.0$. Figure 6.5c shows these contours at the end of rotation for the low rotation rate case at time $t = 47.0$. This rotated case shows turbulent structures elongated with an orientation along the axis of rotation. This is consistent with the increasing correlations shown in Figure 6.4. Thiele [110] has shown similar results with contour structures traversing virtually the entire domain in the direction of rotation. While such contours indicate an orientation of the turbulent structure in the rotation direction they also show that the domain is too small in those simulations for accurate statistics. Perot [33] shows that for isotropic turbulence any length scale that extends beyond one quarter of the

domain length is an indication that the flow is becoming domain constrained and periodicity is affecting the turbulent statistics.

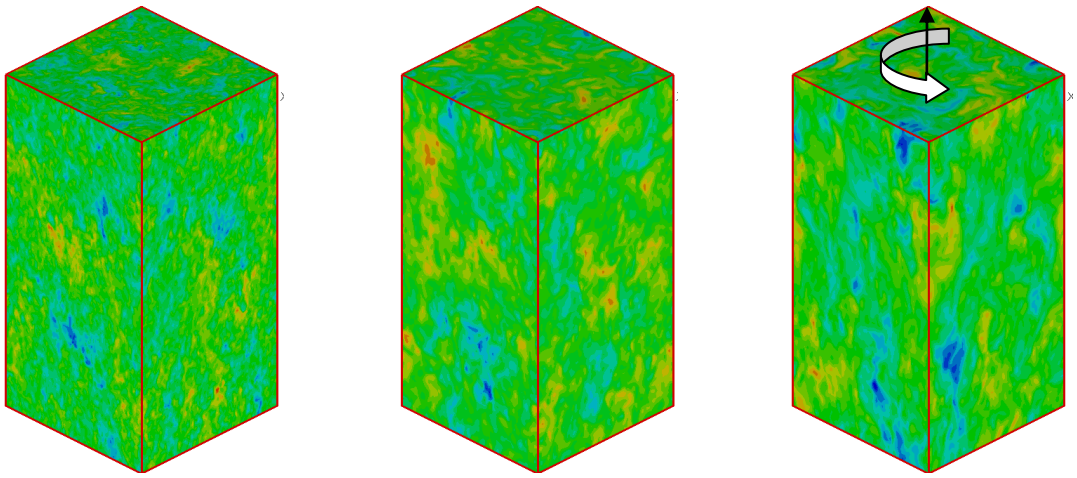

(a) (b) (c)

Figure 6.5 Contours of w-velocity. w-velocity is the component aligned with the axis of rotation. (a) IC1 at $\boldsymbol{t = 17.0}$, not yet rotated. (b) $\boldsymbol{t = 47.0}$ non-rotated. (c) $\boldsymbol{t = 47.0}$ rotated.

Figure 6.6a shows the power law decay exponent as a function of all the rotation rates on IC1, where each rotational case has been scaled so that the effects of rotation are shown from $\Omega T = 0 \rightarrow 3.0$. All exponent values can be seen to be approaching an asymptotic limit after 3 rotations. It can be seen in figure 6.6a that the decay exponent drops more quickly and to a greater degree with higher rotation rates (i.e. decay rate is inversely proportional to rotation rate). Attempts at very high rotation rates can only be calculated with very small time steps and these simulations are beyond the resources of this work. Figure 6.6b shows the same decay exponents as those in figure 6.6a but without a scaling of the x-axis. After rotation is stopped the turbulence decays exponentially, and not as a power law. The power-law exponent, n, therefore makes no sense (and goes to infinity) after rotations stops.

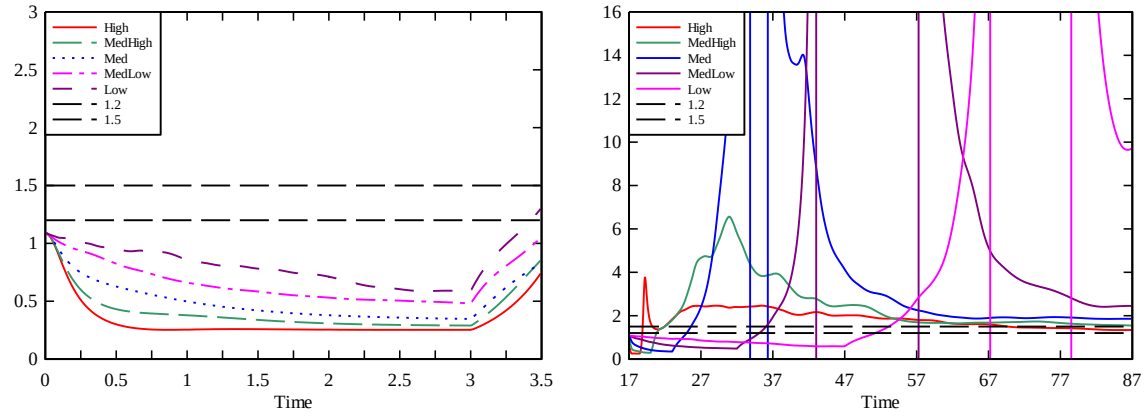

Figure 6.6 Decay exponents as a function of time. Decay exponent is seen to be inversely proportional to rotation rate. (a) x-axis scaled to align end of rotation period. (b) Decay exponent during and subsequent to rotation.

Figure 6.6b shows that the higher rotation rates, and shorter duration cases, recover a power-law decay exponent more quickly than those cases with slower rotation rate and a longer duration.

As has been stated it is well known that the turbulent kinetic energy decay rate decreases due to rotation. However questions remain as to the relationship between rotation rate and decay rate. Squires, Chasnov, Mansour & Cambon [114] performed LES in an attempt to characterize the relationship between rotation rate and the decay exponent. Their findings indicate a reduction of the decay exponent by approximately $1/2$ from the non-rotating case at very strong rotation rates. Our results differ, and suggest that the lower limit for the decay rate is zero for very high rotation rates. This suggests that rotation can completely disrupt the energy cascade if it is rapid enough.

Figure 6.7 shows the present study's decay exponent during rotation as a function of non-dimensional rotation rate for all three ICs. Results shown in Figure 6.7 suggest a power law relationship between rotation rate and the decay-rate exponent with a slope (exponent) of approximately -1/4.

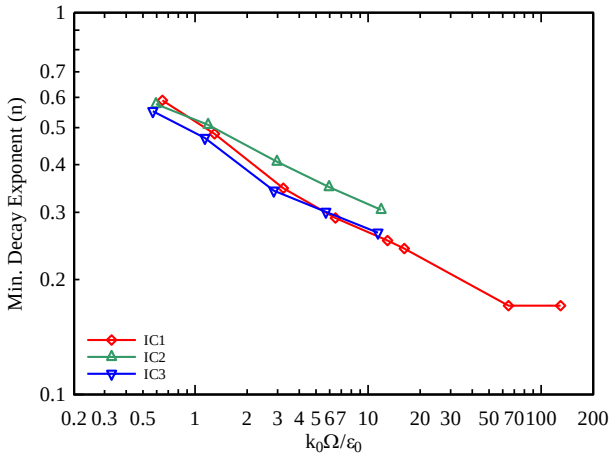

Figure 6.7 Minimum decay rate as a function of non-dimensional rotation rate

6.6 Modeling

Historically and up to this point in this work the behavior of decaying kinetic energy has been assumed to follow a power-law with respect to time, $k(t) = k_0(t - t_0)^{-n}$. This power law assumption has been a focal point in the research of decaying turbulence for many years and by many authors. Saffman established theoretical power law exponent values (n) of 1.2 and 1.5 for high and low Reynolds numbers respectively (for a k^2 low wave number spectrum). Many authors over the years have produced experimental and numerical results that aim to validate or invalidate these theoretical values. Rotation reduces the decay rate and therefore the power law decay exponent is seen to drop during rotation. The drop and dependence of the power law decay exponent on rotation rates has been address herein and by previous researchers.

Previous research by Squires [114] suggests that rotation reduces the power law decay exponent by ½ in the limit of large rotation rates. The current research indicates

that the power law decay exponent exhibits a power law dependence on rotation rate, see Figure 6.7, of approximately -1/4 which leads to a decay exponent of zero at large rotation rates. In all simulated cases we obtain decay exponents for rotation that are less than 3/5 (half the un-rotating decay exponent of 6/5).

While much research exists surrounding the power-law decay exponent and its value in the presence of rotation, little if any work as been published with regarding to the power law exponent following the removal of rotation. It has been well established that rotation restricts dissipation and disrupts the energy cascade. Evaluating the decay of TKE following the remove of rotation would seem to be the next logical step yet to this author's knowledge, no work has been published that addresses the behavior of the decay rate subsequent to the removal of rotation.

Figure 6.7b indicates that modeling the decay of TKE as a power law function is not be valid for some period of time subsequent to the removal of rotation. The erratic behavior of the power law exponent subsequent to the removal of rotation indicates a decay rate of TKE that is exponential, $k(t) = k_0 e^{-c\frac{\varepsilon}{k}(t-t_0)}$ and not a power law

TKE decaying exponentially with time would be evidenced by the ratio of $k(t)$ to its derivative dk/dt remaining constant in time (i.e. $k(t)/\varepsilon(t) = const.$) where $\varepsilon(t) = -dk/dt$. Figure 6.8a shows plots of the behavior of $k(t)/\varepsilon(t)$ for all 5 rotation rates on IC1. It can be clearly seen in the lower rotation rate cases that following the end of rotation, plots of $k(t)/\varepsilon(t)$ maintain a constant value. This leveling off of the curves is less evident in the higher rotation rate (lower rotation duration) cases. This would indicate that the duration of the rotation is more important than the rotation rate in setting up an exponential decay following the end of rotation. Figures 6.8b,c,d,e,f show the

$k(t)/\varepsilon(t)$ plotted along with the power law decay exponent. Comparing the two on each one of the individual plots allows one to see the distinct period of erratic behavior of a power law decay exponent, n, when it is attempting to capture exponential decay. Figures 6.8b,c,d show the period of exponential decay following the end of rotation and the recovery of power law decay after a period of time. Here the power law decay exponent n returns to levels commensurate with Saffman's predictions of n = 1.2-1.5 while the plot of $k(t)/\varepsilon(t)$ moves off a constant value. Figures 6.8e,f show only slight indications that TKE is decaying exponentially. In these cases it is hypothesized that the lack of time under the influence of rotation has not allow for the build up and quasi two-dimensionalization of the turbulence, as described by Theile [110], which is thought to lead to the eventual exponential decay as the turbulence returns to its natural three-dimensional state. Similar results are seen in IC2 and IC3 and have been omitted for brevity.

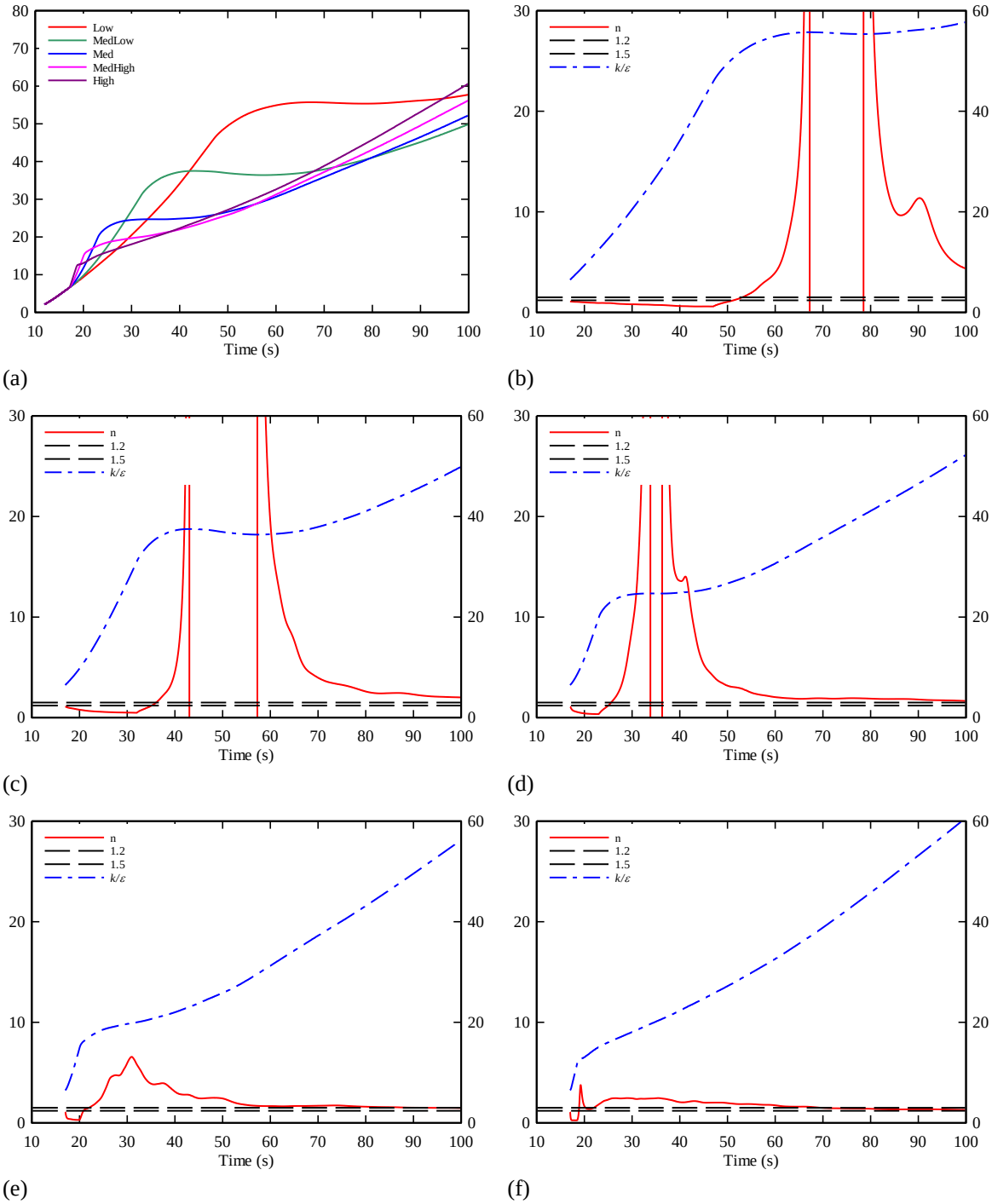

Figure 6.8 Evidence of exponential decaying turbulence through a constant value of $\boldsymbol{k(t)/\varepsilon(t)}$. (a) a comparison of all rotation rates. (b)(c)(d)(e)(f) $\boldsymbol{k(t)/\varepsilon(t)}$ and the erratic behavior of the traditional power law decay exponent attempting to capture exponential decay.

CHAPTER 7

DISCUSSION AND CONCLUSIONS

Direct numerical simulations were carried out on a periodic domain using a staggered Cartesian mesh and 3-step and 2nd-order Runge-Kutta for time advancement. Mesh sizes for plain strain as well as axi-symmetric contraction and axi-symmetric expansion were 512 x 512 x 512 while rotation cases utilized a 512 x 512 x 1024 mesh with 1024 being aligned with the axis of rotation to accommodate increasing longitudinal correlations. A unique stirring method mixes the fluid mechanically allowing for the generation of turbulence and the development of turbulence scales and the energy spectra in a more natural way.

Plain strain, AXC, AXE and rotation all exhibit a $recovery$ phase where turbulent structure in the form of two point turbulent velocity correlations are returning to isotropy faster than the classically defined measure of anisotropy, Reynolds stresses. Traditional and well used return-to-isotropy models such as the linear model of Rotta [65] and more general non-linear models such as that of Sankar & Speziale [18], model return-to-isotropy using only single point statistic in the form of conventional Reynolds stress anisotropy, $R_{11} \neq R_{22} \neq R_{33}$. Results in Chapter 5 reveal, through the DNS data generated herein, that an attempt to back into constants for the Rotta or Sankar & Speziale models fails to produce usable constants, a sign that something more than single point statistics are required for an effective return-to-isotropy model. To this end it is proposed that inclusion of structural information in the form of two point correlations

will allow turbulence to be modeled inclusive of a $recovery$ period where two point statistics are returning to isotropy faster than the traditional Reynolds stresses.

Chapter 5 shows results obtained using the OEC model of Martell & Perot [1] in comparison to plain strain DNS results. These OEC results compare favorably to DNS data in the form of Reynolds stresses plots and invariant maps, Figure 5.13 and 5.14 respectively. DNS data when viewed by way of invariant maps, sometimes referred to as Lumley triangles, show invariant trajectories during return-to-isotropy that have the ability to cross one another given different initial starting points. This is counter to the results provided by traditional linear and non-linear return models where all paths back to isotropy are parallel. Further proof that more information than Reynolds stresses is required for proper modeling.

The effect of rotation on isotropic decaying turbulence has been a popular topic of research both experimentally and numerically. This is most likely owed to the fact that so many applications of scientific and engineering interest are affected by rotating turbulence. As is always the case, and often remarked upon by the engineering and scientific community, a better understanding of the behavior of turbulence statistics can lead to a multitude of engineering design improvements. The effect of rotation is certainly no exception and may very well be of primary importance. There is a great deal of research that has been conducted on turbulence under the direct influence of (during) rotation. Results by previous authors such as those by Squires et. al. contradicts the result of the present study. Squires et. al. suggest the power law decay exponent is reduced during rotation, they also suggest a level which is independent of rotation rate. They go on to propose that the decay exponent under the influence of rotation is dependent only

on the form of the prescribed energy spectra at the onset of rotation. The current study utilizes a relatively new and unique stirring method to generate the turbulence so that the scales of turbulence develop more naturally and thus the energy spectra takes a form that is not directly prescribed by the researcher. From these, arguably more natural energy spectra, it is found that the power law decay exponent behaves as a power law itself, a power law as a function of rotation rate. This power law dependence, with $n=-\frac{1}{4}$, is shown to exist across the set of three initial conditions.

Finally, results within this study which reveal an exponential decay rate for turbulent kinetic energy, subsequent to the removal of rotation, are unknown to have been previously published or otherwise documented. It is hypothesized that during the period of rotation, the turbulence becomes quasi two-dimensional as discussed by Squires et. al. Upon the removal of rotation and during the $recovery$ period, while the three-dimensionality is being recovered, the turbulence dissipates energy rapidly, at an exponential rate, until which time the turbulence is once again three-dimensional and undergoing the well research and documented power law decay.

Several simulation and modeling goals have been met and are summarized as follows:

- The whole of return-to-isotropy is a two part process including a $recovery$ and a return process. The $recovery$process, in which two point correlation anisotropy is returning to isotropy, occurs faster than the traditionally discussed and modeled return-to-isotropy of Reynolds stresses. Two point statistics models, such as

OEC, show promise in better capturing the entirety of the return-to-isotropy process by including this two point correlation information.

- Under the influence of rotation the decay of turbulent kinetic energy exhibits a power law dependency as a function of rotation rate. During rotation the power law decay exponent reaches an asymptotic limit (minimum). This limit is a function of rotation rate. It is important to be clear that this behavior occurs while rotation is taking place and not subsequent to its removal.
- Under the influence of rotation longitudinal two point correlations aligned with the axis of rotation grow stronger while Reynolds stresses change only slightly.
- The method of mechanically stirred turbulence is an effective methodology in the study of isotropic and anisotropic decaying turbulence.
- Further evidence is provided, by the crossing of return-to-isotropy trajectories on invariant maps, that simple linear and non linear return-to-isotropy models are in sufficient to capture the behavior of return-to-isotropy.
- Upon removal of rotation, the behavior of the decay of turbulent kinetic energy is shown to decay exponentially for a period of time before resuming the well documented and theorized power law behavior.

B I B L I O G R A P H Y

[1] M. B. Martell and J. B. Perot, "The Oriented-Eddy Collision Model," *Flow Turbulence and Combustion,* vol. 89, no. 3, pp. 335-359, 2012.

[2] P. A. Davidson, Turbulence an Introduction for Scientist and Engineers, New York, NY: Oxford, 2004.

[3] P. A. Durbin, "Near-wall turbulence closure modeling without damping functions," *Theoret. Comput. Fluid Dynamics,* vol. 3, pp. 1-13, 1991.

[4] J. Kim, P. Moin and R. Moser, "Turbulence statistics in fully developed channel flow at low Reynolds number," *Journal of Fluid Mechanics,* vol. 177, pp. 133-166, 1987.

[5] C. G. Speziale, R. M. So and B. A. Younis, "On the prediction of turbulent secondary flows," ICASE Report 92-57, 1992.

[6] P. R. Spalart and S. R. Allmaras, "A One-Equation Turbulence Model for Aerodynamic Flows," *Recherche Aerospatiale,* vol. 1, pp. 5-21, 1994.

[7] P. R. Spalart, "Strategies for turbulence modeling and simulations.," *Rodi and Laurence, eds. Elsevier,* 1999.

[8] L. Le Penven, J. N. Gence and G. Comte-Bellot, "On the Approach to Isotropy of Homogeneous Turbulence: Effect of the Partition of Kinetic Energy Among the Velocity Components," in *Frontiers in Fluid Mechanics*, New York, NY: Springer, 1985, pp. 1-21.

[9] J. L. Lumley and G. R. Newman, "The return to isotropy of homogeeous turbulence," *Journal of Fluid Mechanics,* vol. 82, pp. 161-178, 1977.

[10] K. S. Choi and J. L. Lumley, "Turbulence and Chaotic Phenomena in Fluids," in *Proceedings of the IUTAM Symposium*, Kyoto, Japan, 1984.

[11] K. Choi and J. L. Lumley, "The return to isotropy of homogeneous turbulence," *Journal of Fluid Mech,* vol. 436, pp. 59-84, 2001.

[12] J. N. Gence and J. Mathieu, "The return to isotropy of an homogeneous turbulence having been submitted to two successive plane strains," *Journal of Fluid Mechanics,* vol. 101, p. 555, 1980.

[13] V. G. Harris, J. A. H. Graham and S. Corrsin, "Further experiments in nearly homogeneous turbulent shear flow," *Journal of Fluid Mechanics,* vol. 81, p. 657–687, 1977.

[14] R. S. Rogallo, "Numerical experiments in homogeneous turbulence," 1981.

[15] K. Yamamoto, "Numerical simulation of the return to isotropy of homogeneous turbulence," National Aerospace Laboratory, Japan, 1985.

[16] M. Yamamoto and C. Arakawa, "Study on the Pressure-Strain Term in Reynolds Stress models," in *Proceedings of the Eighth Symposium on Turbulent Shear Flows*, Technical University of Munich, Munich, Germany, 1991.

[17] T. Sjögren and A. V. Johansson, "Development and calibration of algebraic nonlinear models for terms in the Reynolds stress transport equation," *Physics of Fluids,* vol. 12, p. 1554, 2000.

[18] S. Sarkar and C. G. Speziale, "A Simple nonlinear model for the return to isotropy in turbulence," *Physics of Fluids,* vol. A, no. 2, p. 84, 1990.

[19] D. C. Haworth and S. B. Pope, "A generalized Langevin model for turbulent flows," *Physics of Fluids,* vol. 29, no. 2, 1986.

[20] D. Besnard, F. H. Harlow, R. Rauenzahn and C. Zemach, "Spectral transport model for turbulence," LA-11821-MS, 1990.

[21] D. C. Besnard, F. H. Harlow, R. M. Rauenzahn and C. Zemach, "Spectral Transport Model for Turbulence," *Theoretical and Computational Fluid Dynamics,* vol. 8, pp. 1-35, 1996.

[22] W. C. Reynolds and S. C. Kassinos, "One-point modeling of rapidly deformed homogeneous turbulence," *Proceedings of the Royal Society of London A,* vol. Osborne Reynolds Centenary Volume, pp. 87-104, 1995.

[23] P. R. Van Slooten and S. B. Pope, "PDF modeling for inhomogeneous turbulence with exact representation of rapid distortions," *Physics of Fluids,* vol. 9, no. 4, p. 1085, 1997.

[24] J. B. Perot and C. Chartrand, "Modeling Return to Isotropy Using Kinetic Equations," *Physics of Fluids,* vol. 17, p. 3, 2005.

[25] T. Kurian and J. H. M. Fransson, "Grid-generated turbulence revisited," *Fluid Dynamics Research,* vol. 41, no. 2, p. Article number 021403, 2009.

[26] S. C. Kassinos and W. C. Reynolds, "A structure-based model for the rapid distortion of homogeneous turbulence," Stanford University, Stanford, CA, 1994.

[27] S. C. Kassinos, W. C. Reynolds and M. M. Rogers, "One-point turbulence structure tensors," *Journal of Fluid Mechanics,* vol. 428, pp. 213-248, 2001.

[28] S. C. Kassinos, C. A. Langer, S. L. Haire and W. C. Reynolds, "Structure-based turbulence modeling for wall-bounded flows," *International Journal of Heat and Fluid Flow,* vol. 21, pp. 599-605, 2000.

[29] S. C. Kassinos and E. Akylas, "Advances in Particle Representation Modeling of Homogeneous Turbulence. From the Linear PRM Version to the Interacting Viscoelastic IPRM," *New Approaches in Modeling Multiphase Flows and Dispersion in Turbulence, Fractal Methods and Synthetic Turbulence,* vol. ERCOFTAC Series 18, no. DOI 10.1007/978-94-007-2506-5_6, pp. 81-101, 2012.

[30] N. K. R. Kevlahan and J. C. R. Hunt, "Nonlinear interactions in turbulence with strong irrotational straining," *Journal of Fluid Mechanics,* vol. 337, p. 333, 1997.

[31] G. K. Batchelor and I. Proudman, "The effect of rapid distortion of a fluid in turbulent motion," *Quarterly Journal of Mechanics and Applied Mathematics,* vol. 7, no. 1, p. 83, 1954.

[32] M. Hallbäck, J. Groth and A. V. Johansson, "An algebraic model for nonisotropic turbulent dissipation rate in Reynolds stress closures," *Physics of Fluids,* vol. 2, no. 10, p. 1859, 1990.

[33] J. B. Perot, "Determination of the decay exponent in mechanically stirred isotropic turbulence," *AIP Advances 1,* vol. 022104, 2011.

[34] P. G. Saffman, "The large-scale structure of homogeneous turbulence," *Journal of Fluid Mechanics,* vol. 27, p. 581, 1967 .

[35] S. M. de Bruyn Kops and J. J. Riley, "Direct numerical simulation of laboratory experiments in isotropic turbulence," *Physics of Fluids,* vol. 10, p. 2125, 1998.

[36] G. Comte-Bellot and S. Corrsin, "Simple Eularian time correlations of full and narrow-band velocity signals in grid generated isotropic turbulence," *Journal of Fluid Mechanics,* vol. 48, p. 273, 1971.

[37] P. Moin and J. J. Kim, "Tackling turbulence with supercomputers," *Scientific American,* January 1997.

[38] J. B. Perot and P. Moin, "Shear-Free Turbulent Boundary Layers, Part I: Physical insights into near wall turbulence," *Journal of Fluid Mechanics,* vol. 295, p. 199, 1995.

[39] J. B. Perot and P. Moin, "Shear-Free Turbulent Boundary Layers, Part II: New concepts for Reynolds stress transport equation modelling of inhomogeneous flows," *Journal of Fluid Mechanics,* vol. 295, pp. 229-245, 1995.

[40] O. Reynolds, "An Experimental Investigation of the Circumstances Which Determine Whether the Motion of Water in Parallel Channels Shall be Direct or Sinuous and of the Law of Resistance in Parallel Channels," *Philos. Trans. R. Soc.,* vol. 174, no. 935, p. 82, 1883.

[41] N. Rott, "Note on the History of the Reynolds Number," *Annual Revue of Fluid Mechanics 22: I-II (1990).,* vol. 22, no. I-II, 1990.

[42] A. Sommerfeld, "Ein Beitrag zur hydrodynamische Erklärung der turbulenten Flüssigkeitsbewegungen," in *Proceedings of the 4th International Congress of Mathematicians III*, Rome, Italy, 1908.

[43] O. Reynolds, "On the Dynamical Theory of Incompressible Viscous Fluids and the Determination of the Criterion," *Philos. Trans. R. Soc.,* vol. 186, p. 186, 1895.

[44] J. P. Richter, The Notebooks of Leonardo da Vinci, New York, NY: Dover, 1970.

[45] J. L. Lumley, "Some Comments on Turbulence," *Physics of Fluids A,* vol. 4, no. 2, pp. 203-211, 1992.

[46] D. Jackson and B. Launder, "Osborne Reynolds and the Publication of His Papers on Turbulent Flow," *Annual Review of Fluid Mechanics,* vol. 39, p. 19–35., 2007.

[47] J. Jimenez, "The Contributions of A. N. Kolmogorov to the Theory of Turbulence," *http://arbor.revistas.csic.es/index.php/arbor/article/viewFile/550/551*, pp. 589-606, 2004.

[48] R. Ecke, "The Turbulence Problem," *Los Alamos Science,* vol. 29, 2005.

[49] J. L. Lumley and A. M. Yaglom, "A Century of Turbulence," *Flow, Turbulence and Combustion,* vol. 66, pp. 241-286, 2001.

[50] P. A. Davidson, Y. Kaneda, K. Moffatt and K. R. Sreenivasan, A Voyage Through Turbulence, Vols. [12] Davidson, P. A., Kaneda, Y., Moffatt, K. and Sreenivasan, K. R., A Voyage Through Turbulence. Cambride University Press, Cambridge, UK (2011)., Cambridge, UK: Cambride University Press, 2011, pp. [12] Davidson, P. A., Kaneda, Y., Moffatt, K. and Sreenivasan, K. R., A Voyage Through Turbulence. Cambride University Press, Cambridge, UK (2011)..

[51] F. Tonti and E. Zarantonello, "Algebraic Formulation of Elastodynamics: the Cell Method," *Computer Modeling in Engineering & Science (CMES),* vol. 64, no. 1,

pp. 37-70, 2010.

[52] D. C. Wilcox, Basic Fluid Mechanics 4th ed., DCW Industries, 2010.

[53] J. B. Perot, "Conservation Properties of Unstructured Staggered Mesh Schemes," *Journal of Computational Physics,* vol. 159, no. 1, p. 58, 2000.

[54] F. H. Harlow and J. E. Welch, "Numerical Calculation of Time-Dependent Viscous Incompressible Flow of Fluid with Free Surface," *Physics of Fluids,* vol. 8, no. 12, p. 2182, 1965.

[55] F. H. Harlow, "Fluid dynamics in Group T-3 Los Alamos National Laboratory," *Journal of Computational Physics* , vol. 195, p. 414–433, 2004.

[56] X. Zhang, D. Schmidt and J. B. Perot, "Accuracy and Conservation Properties of a Three-Dimensional Unstructured Staggered Mesh Scheme for Fluid Dynamics," *Journal of Computational Physics,* vol. 175, pp. 764-791, 2002.

[57] D. Besnard, F. H. Harlow, N. L. Johnson, R. M. Rauenzahn and J. Wolfe, "Instabilities & Turbulence," *Los Alamos Science, Number 15, Special Issue, Stanislaw Ulam,* vol. 15, pp. 1909-1984, 1987.

[58] M. M. Hand, D. A. Simms, L. J. Fingersh, D. W. Jager, J. R. Cotrell, S. Schreck and S. M. Larwood, "Unsteady Aerodynamics Experiment Phase VI: Wind Tunnel Test Configurations and Available Data Campaigns," 2001.

[59] S. B. Pope, Turbulent Flows, New York, NY: Cambridge University Press, 2000.

[60] D. Wilcox, Turbulence Modeling for CFD, La Canada, CA, USA: DCW Industries, 1993.

[61] J. D. Anderson, A History of Aerodynamics: And Its Impact on Flying Machine, New York, NY, USA: Cambridge University Press, 2000.

[62] P. A. Libby, Introduction to Turbulence, Washington, D.C., USA: Taylor & Francis, 1996.

[63] P. A. P. R. B. A. Durbin, Statistical Theory and Modeling for Turbulent Flows, 2nd ed., The Atrium, Souther Gate, Chichester, West Sussex, United Kingdom: John Wiley & Sons, Ltd, 2001.

[64] F. Mentor, "Two-equation eddy-viscosity turbulence models for engineering applications," *AIAA J.,* vol. 32, pp. 1598-1605, 1994.

[65] J. C. Rotta, "Statistische Theorie Nichthomogener Turbulenz," *Mitteilung Z. Physik,* vol. 129, p. 547, 1951.

[66] J. B. Perot, "PhD Thesis".

[67] P. G. Saffman and D. I. Pullin, "Calculation of velocity structure functions for vortex models of isotropic turbulence," *Physics of Fluids,* vol. 8, p. 3072–3084, 1996.

[68] P. L. Bhatnagar, E. P. Gross and M. Krook, "A Model for Collision Processes in Gases. I. Small Amplitude Processes in Charged and Neutral One-Component Systems," *Physical Review,* vol. 94, no. 3, p. 511–525., 1954.

[69] H. Chen, S. A. Orszag, I. Staroselsky and S. Succi, "Expanded analogy between Boltzmann kinetic theory of fluids and turbulence," *Journal of Fluid Mechechanics,* vol. 519, pp. 301-314, 2004.

[70] S. B. Pope, "A Lagrangian two-time probability density function equation for inhomogeneous turbulent flows," *Physics of Fluids,* vol. 26, pp. 3448-3450, 1983.

[71] J. B. Perot, "An Analysis of the Fractional Step Method," *Journal of Computational Physics,* vol. 1, p. 108, 1993.

[72] W. Chang, F. Giraldo and J. B. Perot, "Analysis of an Exact Fractional Step Method," *Journal of Computational Physics,* vol. 179, pp. 1-17, 2002.

[73] H. Le, P. Moin and J. Kim, "Direct numerical simulation of turbulent flow over a backward step," *Journal of Fluid Mechanics,* vol. 330, p. 349, 1997.

[74] M. Martell, J. B. Perot and J. Rothstein, "Direct Numerical Simulation of Turbulent Flow over Drag-Reducing Ultrahydrophobic Surfaces," *Journal of Fluid Mechanics,* vol. 620, p. 31, 2009.

[75] J. B. Perot and V. Subramanian, "Discrete Calculus Methods for Diffusion," *Journal of Computational Physics,* vol. 224, no. 1, p. 59, 2007.

[76] A. Wray, "Decaying Isotropic Turbulence," 1998.

[77] A. A. Townsend, "The uniform distortion of homogeneous turbulence," *Quarterly Journal of Mechanics and Applied Mathematics,* vol. 7, p. 104, 1954.

[78] T. H. J. and A. J. Reynolds, "The distortion of turbulence by irrotational plane strain," *Journal of Fluid Mechanics,* vol. 32, p. 657, 1968.

[79] A. J. Reynolds and H. J. Tucker, "The distortion of turbulence by general uniform irrotational strain," *Journal of Fluid Mechanics,* vol. 68, no. 4, 1975.

[80] D. Kwak, W. C. Reynolds and J. H. Ferziger, "Three-Dimensional Time Dependent Computation of Turbulent Flow," 1975.

[81] M. J. Lee and W. C. Reynolds, "Numerical experiments on the structure of homogeneous turbulence," 1985.

[82] M. M. Rogers and P. Moin, "The structure of vorticity fields in homogeneous turbulent flows," *Journal of Fluid Mechanics,* vol. 68, p. 537, 1975.

[83] C. Barre, F. Mashayek and D. B. Taulbee, "Statistics in particle-laden plane strain turbulence by direct numerical simulation," *International Journal of Multiphase Flow,* vol. 27, no. 2, p. 347, 2001.

[84] K.-S. Choi, "A Study of the Return to Isotropy of Homogeneous Turbulence," 1983.

[85] J. L. Lumley, "Computational modeling of turbulent flows," *Adv. Appl. Mech,* vol. 18, p. 123–176, 1978.

[86] P. G. Saffman, "Note on decay of homogeneous turbulence," *Phys. Fluids 10,* p. 1349, 1967.

[87] S. R. Stalp, "Decay of grid turbulence in a finite channel," *Physical review Letters 82,* pp. 4831-4834, 1999.

[88] H. Touil, J. P. Bertoglio and L. Shao, "The decay of turbulence in a bounded domain," *Journal of Turbulence,* vol. 3, p. 49, 2002.

[89] H. S. Kang, S. Chester and C. Meneveau, "Decaying turbulence in an active-grid-generated flow and comparisons with large-eddy simulation," *Journal of Fluid Mechanics,* vol. 480, pp. 129-160, 2003.

[90] W. K. George, "Is there an asymptotic effect of initial and upstream conditions on turbulence?," in *Freeman Lecture, ASME Fluids Engineering Meeting*, Jacksonville, FL, USA, 2008.

[91] M. S. Uberoi, "Equipartition of energy and local isotropy in turbulent flow," *Journal of Applied Physics*, vol. 28, p. 1165 .

[92] R. R. Mills and S. Corrsin, "Effect of contraction in turbulence and temperature fluctuations generated by a warm grid".

[93] G. Comte-Bellot and S. Corrsin, "The use of a contraction to improve the isotropy of grid-generated turbulence," *J. Fluid Mech.*, vol. 25, p. 657, 1966.

[94] J. L. N. G. R. Lumley, "The return to isotropy of homogeeous turbulence," *Journal of Fluid Mechanics*, vol. 82, pp. 161-178, 1977.

[95] T. Sjogren and A. V. Johansson, "Measurement and modeling of homogeneous asisymmetric turbulence," *Journal of Fluid Mechanics*, vol. 374, pp. 59-90, 1998.

[96] S. Banerjee, O. Ertunc, C. Koksoy and F. Durst, "Pressure strain rate modeling of homogeneous axisymmetric turbulence," *Journal of Turbulence*, 2009.

[97] O. Ertunc and F. Durst, "On the high contraction ration anomaly of axisymmetric contraction of greid-generated turbulence," *Physics of Fluids*, vol. 25103, p. 115, 2008.

[98] J. L. Lumley, "Pressure-strain correlation," *Physics of Fluids*, vol. 18, p. 750, 1975.

[99] C. Cambon and J. F. Scott, "Linear and nonlinear models of anisotropic turbulence," *Annual Review of Fluid Mechanics*, vol. 31, pp. 1-53, 1999.

[100] C. J. Zusi and J. B. Perot, "Simulation and Modeling of Turbulence Subjected to a Period of Uniform Plane Strain," *Phys. Fluids*, vol. 25, no. 110819, 2013.

[101] L. Le Penven, J. N. Gence and G. Comte-Bellot, "On the Approach to Isotropy of Homogeneous Turbulence: Effect of the Partition of Kinetic Energy Among the Velocity Components," in *Frontiers in Fluid Mechanics*, New York, NY: Springer, 1985, pp. 1-21.

[102] T. Teitelbaum and P. D. Mininni, "The decay of turbulence in rotating flows," *Physics of Fluids*, vol. 23, no. 065101, pp. 1-15, 2011.

[103] R. A. Wigeland and H. M. Nagib, "Grid-generated turbulence with and without rotation about the streamwise direction," Illinois Inst. of Tech., Chicago, Illinois, 1978.

[104] J. Barinda, J. H. Ferzinger and R. S. Rogallo, "Effect of rotation on isotropic turbulence: computation and modeling," *J. Fluid Mech.*, vol. 154, pp. 321-336.

[105] C. G. Speziale, N. N. Mansour and R. S. Rogallo, "The Decay of Isotropic Turbulence in a Rapidly Rotating Reference Frame," in *Center for Turbulence Research Proceedings of the Summer Program 1987*, 1987.

[106] C. G. Speziale, R. Raj and T. Gatski, "MODELING THE DISSIPATION RATE IN ROTATING TURBULENT FLOWS," NASA ICASE Report N. 90-88, Hampton, Virginia, 1990.

[107] S. B. Pope, "An Explanation of the Turbulent Round Jet/Plane Jet Anomaly," *AIAA J.*, vol. 16, pp. 279-281, 1978.

[108] K. Hanjalic and B. E. Launder, "Sensitizing the Dissipation Equation to Irrotational Strains," *ASME J. Fluids Eng.,* vol. 102, pp. 34-40, 1980.

[109] R. Raj, "Form of the Turbulence Dissipation Equation as Applied to Curved and Rotating Turbulent Flows," *Phys. Fluids,* vol. 18, pp. 1241-1244, 1975.

[110] M. Thiele and W. C. Muller, "Structure and decay of rotating homogeneous turbulence," *J. Fluid Mech,* vol. 637, pp. 425-442, 2009.

[111] X. Yang and A. Domaradzki, "Large eddy simulations of decaying rotating turbulence," *Physics of Fluids,* vol. 16, no. 11, pp. 4088-4104, 2004.

[112] H.-H. Tsuei and J. B. Perot, "Advanced Turbulence Model for Transitional and Rotational flows in Turbomachinery," *AIAA,* vol. 0134, pp. 1-14, 2000.

[113] C. Cambon and B. Grea, "The role of directionality on the structure and dynamics of strongly anisotropic turbulent flows," *Journal of Turbulence,* vol. 14, no. 1, pp. 50-71, 2013.

[114] K. D. Squires, J. R. Chasnov, N. N. Mansour and C. Cambon, "The Asymptotic State of Rotating Turbulence At High Reynolds Numbers," in *74th Fluid Dynamics Symposium on "Application of Direct and Large Eddy Simulations to Transition and Turbulence"*, Chania, Crete, Greece, 1994.

[115] C. Chartrand, "Development of the Eddy Collision Model," Amherst, MA, 2005.

[116] R. Mba, "Extension of the Eddy Collision Model to Complex Turbulent Flows," Amhert, MA, 2008.